POLITECNICO DI TORINO

MASTER's Degree in ENVIRONMENTAL AND LAND ENGINEERING

MASTER's Degree Thesis

Attenuation Correction Methodology for Multi-Frequency Weather Radars

Supervisors

Prof. Alessandro BATTAGLIA

Dr. Renzo BECHINI

Dr. Valentina CAMPANA

Candidate

Chiara LEVA

MARCH 2026

Abstract

This work investigates signal attenuation in weather radars and its practical implications for Quantitative Precipitation Estimation (QPE), a key step for hydrological modeling and risk management. Radar attenuation, caused by absorption and scattering of the electromagnetic waves by hydrometeors along the propagation path, leads to reflectivity underestimation and consequently to biased QPEs. The magnitude of this effect depends on radar frequency as well as on microphysical properties of precipitation, including drop size distribution (DSD), particle orientation, and temperature.

Dual-polarization radars transmit and receive electromagnetic waves at different polarizations, typically horizontal and vertical, providing additional variables that enable attenuation correction. In particular, the differential phase shift (Φ_{dp}), which arises from the difference in propagation velocity between horizontally and vertically polarized waves, is proportional to the path-integrated attenuation and therefore represents a robust variable for quantifying and correcting the signal degradation. Despite this capability, operational attenuation correction procedures commonly rely on fixed attenuation coefficients selected solely according to radar frequency, neglecting the variability of individual precipitation events and the microphysical properties of hydrometeors.

The aim of this Thesis is to develop and validate an event-based methodology for optimizing attenuation coefficients in dual-polarization radars operating at different frequencies. The quantitative analysis is conducted using data from the Arpa Piemonte radar network, which includes three systems: Bric della Croce, Monte Settepani, and Druento. The first two are C-band systems, operating at 5.6 GHz, while the third is an X-band system operating at 9.4 GHz. By exploiting collocated radar observations and applying a regression-based optimization approach, event-specific attenuation coefficients are derived and compared with the fixed operational values.

The proposed methodology highlights the limitations of fixed-coefficient approaches by revealing significant discrepancies with the fixed values commonly adopted. These differences directly propagate into QPE estimates, leading to non-negligible variations in retrieved cumulative precipitation. This work

therefore demonstrates the importance of frequency- and event-dependent QPE optimization for accurate precipitation monitoring.

ACKNOWLEDGMENTS

To Mum and Dad,

for your endless support.

This degree may bear my name, but this achievement belongs to you too.

Table of Contents

List of Figures

List of Tables

Chapter 1

The weather radar: fundamentals and limitations

The acronym Radar (RAdio Detection And Ranging) traces its origins to World War II, when it was first demonstrated that radio waves could detect physical targets, such as aircraft for military applications and weather for meteorological purposes.

Since its inception, radar technology has undergone substantial development, progressively extending its range of applications to numerous scientific and industrial fields, including military defense, geophysics, astronomy, manufacturing processes, automobile navigation systems and meteorology [1].

In the decades following World War II, particularly during the 1960s and 1970s, the first weather radar networks were established. These early systems were limited to reflectivity measurements, providing only partial information regarding the position and intensity of precipitation. A major advancement in meteorological radar applications was achieved in 1973, when a Doppler system was employed to describe the life cycle of a tornado in Oklahoma, including measurements of radial velocity. From that moment Doppler radars became popular in operational meteorology and Doppler radar networks were progressively deployed worldwide, allowing forecast to get precise measurements of storm dynamics and intensity. For this reason, between 1980 and 2000, they became an integral component of national weather services [1].

Subsequently, a further technological innovation emerged: the dual polarization

Figure 1.1: Schematic picture of raindrops with increasing size, which illustrates their tendency to take on an increasingly pronounced oblate shape as their size increases [1].

weather radar, also known as polarimetric radar. This system allow radio waves to be emitted with a double polarization, specifically horizontal and vertical, enabling precipitation to be investigated in terms of its shape and composition. This capability is particularly relevant because hydrometeors are not perfectly spherical, instead, they tend to adopt an oblate shape, with the degree of flattening increasing as their size grows. Consequently, their horizontal axis becomes progressively larger than the vertical axis, as illustrated in Figure 1.1.

This marked a turning point that profoundly transformed weather radars, adding multiple parameters for observation capability and allowing more precise measurements and classification of precipitation [1].

One of the most common application when using weather radar is the Quantitative Precipitation Estimation (QPE). Unlike rain gauges, these systems are capable of monitoring precipitation on a large scale using a single measuring instrument, ensuring high spatial resolution. In addition, they repeat scans at regular intervals ensuring high temporal resolution. QPE techniques typically rely on radar reflectivity measurements, which are converted into rainfall rate estimates through empirical or physically-based relationships. The hydrometeors diameter ranges between 0.01 and 8 mm and, in order for the precipitation to be visible from the radar without producing too much attenuation, their size should be smaller but not too much smaller than the radar wavelength, λ. For this reason, the operating frequencies of weather radars span from 2.8 GHz ($\lambda \sim 10$ cm) to 9.4 GHz ($\lambda \sim 2$ cm). In Table 1.1 the typical weather radar frequencies, with their corresponding bands and wavelengths, are summarized.

An accurate QPE is fundamental for a wide range of applications, including hydrological modelling, flood forecasting and real-time hazard monitoring. Given that climate change is having a profound impact on hydrology, in addition to other applications, radars observations play an important role in risk

	Frequency (GHz)	Wavelength (cm)
S Band	2.8	10.7
C Band	5.6	5.4
X Band	9.4	3.2

Table 1.1: Operating weather radar frequencies, with their respective radar bands and wavelengths.

prevention and civil protection. However, radar-based QPE may be biased by geometric and physical factors, such as the height of the observation volume above the ground, the variability of the drop size distribution (DSD) in rain, the signal attenuation occurring between the radar and the precipitation target, and the presence of frozen or mixed-phase particles [1].

Low accuracy in QPE can have significant environmental consequences, potentially leading to false alarms or missed detections in flood warnings. In cases of both overestimation and underestimation, this may particularly affect the operations of the Civil Protection Agency. Indeed, each region issues a daily weather report that includes precipitation data-liquid, solid, and snow-alongside other meteorological variables. Based on the alert level indicated in the report, the Civil Protection Agency implements appropriate intervention protocols corresponding to the severity of the situation.

The advent of polarimetric radars marked a key advancement in this regard: the additional variables enabled an improvement of the accuracy by estimating attenuation and deploying it for signal correction.

1.1 The signal attenuation problem

What makes the weather radar fundamental in QPE is the spatial and temporal resolution: this cannot be replaced by any rain-gauge network. However, the lack of accuracy due to remote sensing-based estimates must be taken into account. In fact, the signal is attenuated in the atmosphere, which is a problem that affects the QPE and other radar estimates.

It is widely known that rainfall can interfere with the transmission of signals operating at radio wave frequencies. Signal attenuation results from the absorption and scattering of incident electromagnetic wave energy by hydrometeors

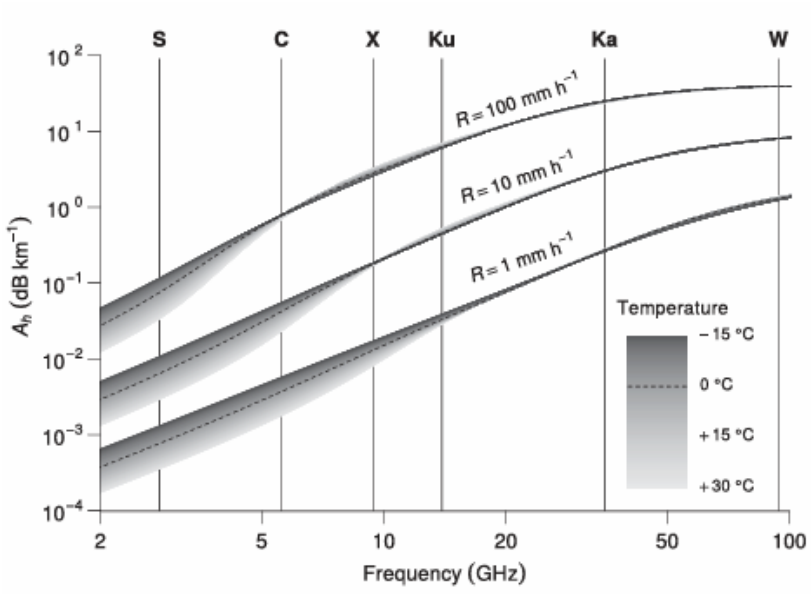

Figure 1.2: Attenuation trend as a function of the radar frequency, temperature and rainfall rate [1].

along the propagation path, leading to a progressive reduction in signal power. As the radar beam traverses precipitating media, this loss of energy causes an underestimation of the measured reflectivity. The resulting bias propagates into Quantitative Precipitation Estimation (QPE), producing underestimated rainfall amounts. The magnitude of this effect increases with the severity of attenuation. This motivates the need for attenuation correction: the signal must be corrected first in order to provide reliable and accurate estimates.
Attenuation is affected by the radar frequency, the drop size distribution (DSD), the particles' orientation and the temperature. An overview of these factors is provided in this introductory chapter, while a detailed analysis is presented in the subsequent ones.

The relationship between attenuation and radar frequency is illustrated in Figure 1.2. Attenuation is enhanced at bigger frequencies f, because they are linked to shorter signal wavelengths λ ($\lambda \propto f^{-1}$), which approach the size of raindrops. When the wavelength is similar to the particle's dimension, its ability to scatter and absorb the signal increases significantly. Furthermore, an increase in attenuation is observed with increasing rainfall rate and decreasing temperature.

1.2 Attenuation correction and radar evolution: the added value of dual polarization

Dual polarization radars, in addition to reflectivity and Doppler velocity measurements, transmit pulses and receive radiation at different polarization, specifically horizontal and vertical. This enables the measurement of additional polarimetric variables, which are fundamental for attenuation correction. Over the past years, polarimetric radars have significantly improved correction techniques and are now essential for accurate forecasting.

Some examples of polarimetric radar quantities are the differential reflectivity, the depolarization ratio, the copolar correlation coefficient and the differential phase shift (Φ_{dp}). The last one mentioned is crucial for attenuation correction and it represents the key added value of polarimetric radars. It measures the differential phase shift between the phase of the copolar signal at horizontal polarization Φ_{HH} and that at vertical polarization Φ_{VV}. Owing to the typically oblate shape of raindrops, the horizontally polarized electromagnetic wave experiences a different propagation velocity compared to the vertically polarized wave. In particular, the horizontal component propagates more slowly, resulting in the accumulation of a phase difference between the two polarization states along the propagation direction.

As consequence, polarimetric radars improve attenuation estimation and correction because Φ_{dp} is proportional to the attenuation of the entire path between the radar and the targets, reflecting its characteristics.

Indeed, Figure 1.3 highlights a proportionality between the attenuation A_h and the specific differential phase shift K_{dp} depending on the DSD, i.e. the drop size distribution, which describes the number of hydrometeors per unit volume as a function of their diameter. Because of the linear relationship between the two variables we introduce a linear coefficient of proportionality between the two quantities, denoted as α. Each radar frequency is associated with a distinct range of variability for the attenuation coefficient α. Specifically, for C-band systems, α typically ranges between 0.06 dB/deg and 0.12 dB/deg, whereas for X-band systems it assumes higher values, generally between 0.26 dB/deg

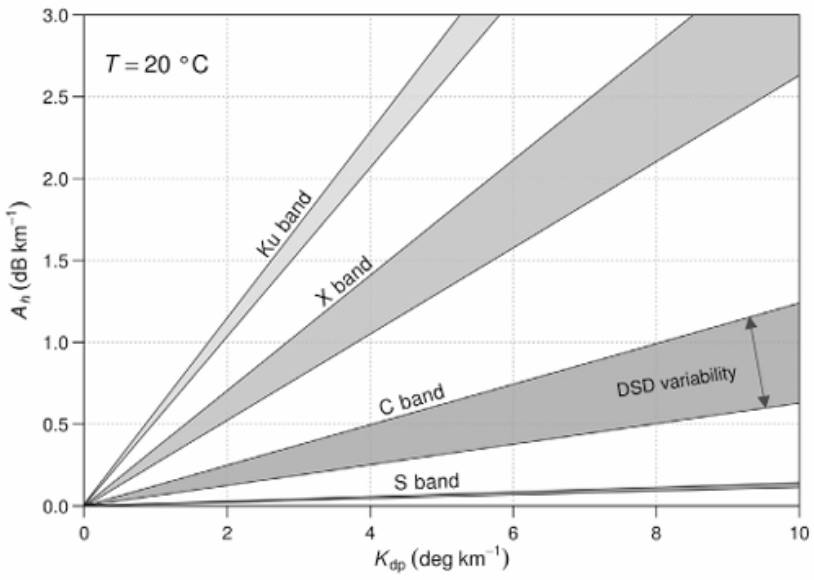

Figure 1.3: Relation between horizontal specific attenuation A_h and K_{dp} at different radar wavelengths and 20°C ([1]).

and 0.35 dB/deg.

These considerations suggest that α should be optimized for each singular event. Indeed, the fixed coefficient α variability depends on several factors, including the signal frequency, the DSD, the particles' orientation and the temperature. Accordingly, each precipitation event must be examined on a case-by-case basis, taking these elements into account, with α specifically optimized, while the associated data should be aggregated over appropriate temporal intervals to ensure reliable estimates.

Nevertheless, operational attenuation correction procedures continue to rely on a fixed coefficient determined solely by the radar's operating frequency. The outcomes of the attenuation correction using the Φ_{dp}- and fixed α- based method for two generic radars are shown in Figure 1.4a and 1.4b. Two radar reflectivities from collocated observation volumes are compared in the density plots, showing the distribution and density of the data values. Since the two radars observe the same precipitation, they should measure the same reflectivity values. Therefore, data points are expected to lie along a straight line with an intercept of 0 and a slope equal to 1. However, the attenuation cause data to deviate from the bisector line and the calibration bias lead to a shift of the data relative to the straight line, as shown in 1.4a. Correcting reflectivities

with a fixed coefficient α and with Φ_{dp} reduces the dispersion and improves the fit, as shown in 1.4b.

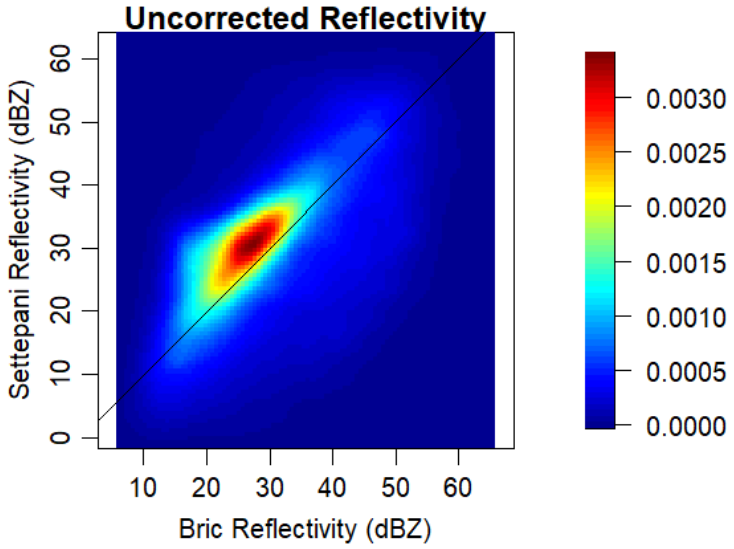

(a) Uncorrected reflectivity values, shown through density plot.

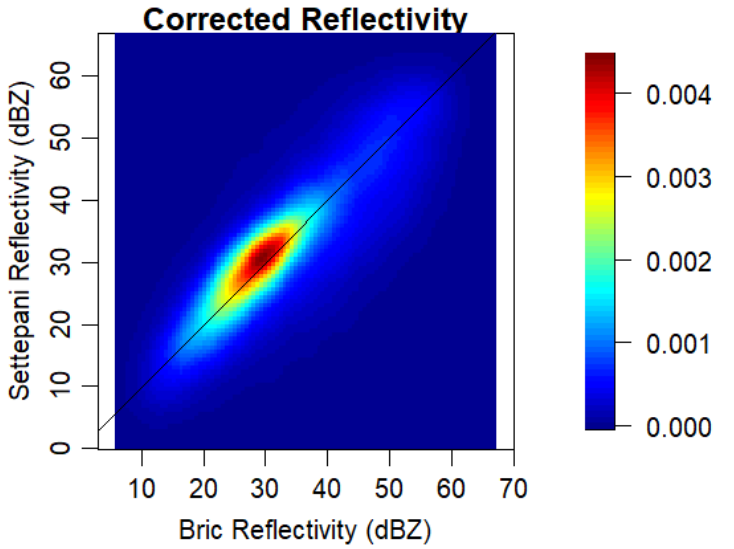

(b) Φ - Method corrected reflectivity values, shown through density plot.

Figure 1.4: Comparison through density plots between uncorrected and Φ - Method corrected reflectivity values.

Dual polarization radar marked a significant improvement in attenuation correction, however calibration bias and dispersion of data are still observed. By examining the density plot for corrected reflectivity values, it is showed that the two radars measure slightly different reflectivities: it is observed a non null intercept, which indicates a radar's calibration bias, and a residual data's dispersion, due to an incomplete attenuation correction.

1.2.1 Thesis goal

The main aim of this Master's Thesis is to optimize the empirical fixed attenuation coefficients currently employed by Arpa Piemonte and to develop a theoretical framework for their refinement using the Arpa radar dataset. Specifically, the study seeks to propose and validate a methodology for deriving event-specific attenuation coefficients in dual-polarization weather radars operating at both C-band and X-band frequencies. By utilizing collocated radar observations and applying a regression-based optimization approach, the methodology allows for the estimation of coefficients tailored to individual precipitation events, which are then compared with the fixed values used in operational practice.

Key questions addressed in this research include: which data filtering strategies should be applied to minimize dispersion and calibration biases while maximizing the performance of the linear regression? What is the optimal temporal interval for data aggregation? And what is the physical interpretation of obtaining optimized coefficients that are higher or lower than the standard values currently adopted by Arpa?

Chapter 2

Scattering and radar measurements

For a radar to operate, it needs a transmitter for the generation of the electromagnetic wave and a receiver for the quantification of the backscattered echoes. When transmitting, the wave propagates radially from the antenna, then the signal encounters the precipitation and it is backscattered to the receiver. The transition from transmitted wave to received power is critical: only a small amount of the original power can be registered by the radar antenna, due to scattering and attenuation processes. Finally, the radar-received power is converted in meaningful parameters for radar users [2].
The echoes registered by weather radars strongly depend on single particles scattering properties, such as the radar cross section, the extinction cross section and the dielectric properties ($|K|^2$, n and ϵ_r). Furthermore, these determine the macroscopic backscattering volume properties, which define the radar measurements. In the following sections each of them will be detailed.

2.1 Single particles scattering properties

When the incident wave interacts with the hydrometeors, it is partially absorbed and partially scattered and diffused in all directions, including towards the radar receiver (Figure 2.1). These phenomena are termed extinction processes and are responsible for the partial loss of the received energy. Therefore, the

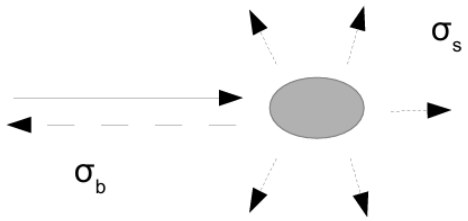

Figure 2.1: Scattering process through schematic representation.

measurements must be analysed and corrected for attenuation.

The scattering volume is filled with an extreme large number of scatterers, each characterized by its scattering cross-section.

Firstly, it is essential to define the backscattering cross-section, also referred to as the *radar cross-section*, which can be expressed as σ_b. This is measured in m^2 and describes how effectively a material reflects or backscatters incident waves: a large drop with a high value of σ_b reflects a significant proportion of the incident wave, resulting in a high power return to the radar.

The all-direction diffusion, on the other hand, is described by the *total scattering radar cross-section*, or σ_s. In contrast, another portion of the incident wave is absorbed by the particle and consequently it will not be registered by the receiving antenna: this is called the *absorption radar cross-section*, or σ_a.

The last two properties identify the extinction cross section, or σ_e, which measures the total amount of lost incident power and it is defined as the portion of energy that does not reach the receiving antenna. For each particle it can be written as follows:

$$\sigma_e = \sigma_a + \sigma_s, \tag{2.1}$$

where σ_a is the loss of radar wave power due to the absorption cross-section and σ_s is the loss due to total scattering cross-section [1].

In order to characterize the scattering cross-sections for arbitrary scatterers, the far-field amplitude vector for each scatterer, $s(\hat{s}, \hat{i})$, must be known for all targets, namely for all combinations of scattering and incident directions, $\hat{s}$ and $\hat{i}$, respectively. Regarding the general bistatic radar cross-section, it can be defined as follows:

$$\sigma_{bi}(\hat{s}, \hat{i}) = 4\pi \left| s(\hat{s}, \hat{i}) \right|^2, \tag{2.2}$$

The total scattered power is usually deployed for the total scattering cross-section calculation, in fact it is true that:

$$\sigma_s = \int_{4\pi} |s(\hat{s}(\Omega), \hat{i})|^2 \, d\Omega, \tag{2.3}$$

where the incident angle is fixed and the scattering angle is varied as a function of the solid angle Ω over the entire sphere.
Ultimately, the extinction cross-section for the scatter is identified as:

$$\sigma_e = -4\pi k_0 \, Im(s(\hat{i}, \hat{i})\Big). \tag{2.4}$$

This corresponds to the power lost by the incident wave due to absorption and scattering, when the incident and scattering directions coincide [1]. These Equations generally do not provide simple closed-form solutions, except in the simplest cases of spheroidal scatterers, available in the Rayleigh scattering regime.

2.1.1 Mie theory and Rayleigh approximation

The scattering processes can be classified into three scattering regimes, as illustrated in Figure 2.2: Rayleigh, Mie and optical. Furthermore, this figure shows how the backscattering, scattering and absorption cross sections vary with the diameter of a water sphere, determining its scattering regime.

The Rayleigh region is characterised by particles with a diameter far below the radar wavelength ($D << \lambda$): here the radar cross-section σ_b is proportional only to the diameter to the sixth power, allowing analytical simplifications of several expressions. Furthermore, particles in this region are assumed to be spherical.
At visible wavelengths, air molecules are much smaller than the wavelength λ and at radar wavelengths (Table 1.1) most atmospheric targets behave as Rayleigh scatterers [2].
Assuming the Rayleigh approximation for hydrometeors, the scattering ampli-

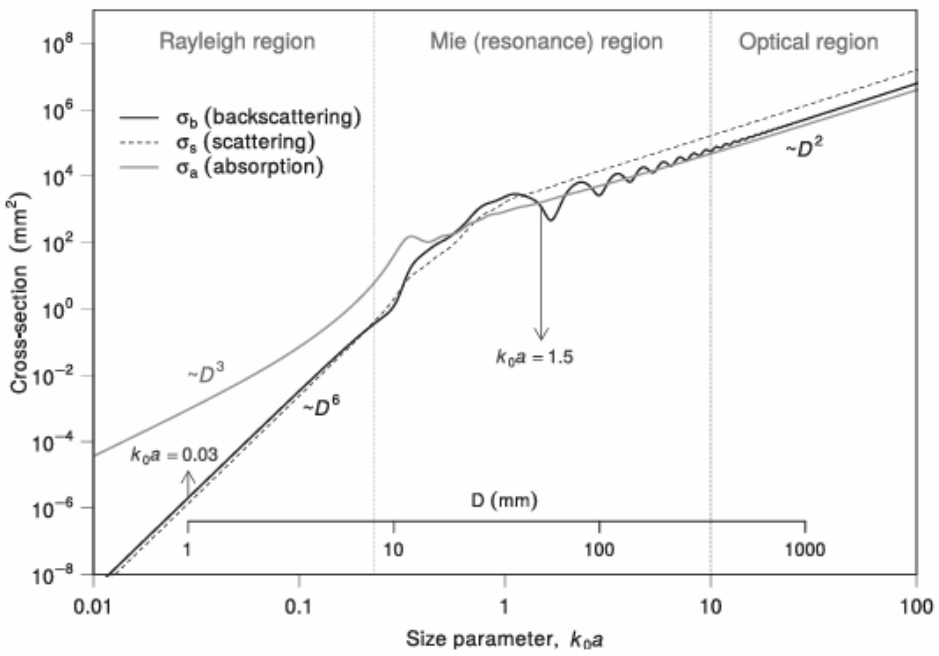

Figure 2.2: Scattering cross-section of spherical water particles at S-band as function of the size parameter, with the comparison between the Rayleigh region, the Mie (resonance) region and the optical region ([1]).

tude of a dielectric sphere is given by:

$$s = s(-\hat{i}, \hat{i}) = \frac{\pi^2}{2\lambda^2} \frac{\varepsilon_r - 1}{\varepsilon_r + 2} D^3, \tag{2.5}$$

and the radar cross-section becomes ([1]):

$$\sigma_b = 4\pi |s|^2 = \frac{\pi^5}{\lambda^4} |K|^2 D^6, \tag{2.6}$$

where ε_r and $|K|^2$ stand for the relative permittivity and the dielectric constant, whose definitions and properties will be discussed in detail below.

Also, since scattering is proportional to D^6 ($\sigma_b \propto D^6$), in the Rayleigh regime larger echoes are produced by larger objects in a disproportionate manner compared to small particles. Therefore, the received power is dominated by the larger drops in the illuminated volume scan [2].

On the other hand, if the diameter is comparable to the radar wavelength λ, we fall into the Mie region or resonance region. In this case the value of the radar cross-section fluctuates due to constructive and destructive interference. The occurrence of this phenomenon depends on the exact value of wavelength

of electromagnetic radiation and the size of the particle.

When the particle size is much larger than the wavelength ($D >> \lambda$), the corresponding region is the optical region instead, so named because most scattering of this type occurs at visible wavelengths. Under these conditions the scattering efficiency factor, defined as $\xi_s(n(\lambda), D, \lambda) \equiv \frac{\sigma_s}{\pi D^2}$, loses its direct dependence on wavelength and diameter, depending only on the refractive index (i.e. the scattering cross section is proportional to D^2, $\sigma_s \propto D^2$) [2].

The microphysical properties of precipitation, such as the dielectric constant together with scattering phenomena, explain why the signal gets more attenuated by the liquid phase than by solid ice or the mixed-phase particles.

Target	Dielectric constant $\lvert K\rvert^2$
Liquid water (cloud, drizzle, rain)	0.93
Solid ice	0.176
Air-ice mixture (snow)	$0.205\,(\rho_s/\rho_i)^2$

Table 2.1: Hydrometeors' dielectric constants.

In order to introduce the backscattering volume properties and the attenuation problem, it is necessary to introduce the dielectric properties of a single particle. The first one is the complex dielectric constant $|K|^2$, which can be defined as follows:

$$|K|^2 = \left|\frac{n(\lambda)^2 - 1}{n(\lambda)^2 + 2}\right|^2, \tag{2.7}$$

where $n(\lambda)$ is the refractive index of the hydrometeor [2].

$|K|^2$ affects scattering: a higher value of this parameter leads to a higher backscattered power to the radar. Furthermore, in the Rayleigh regime, the extinction process (i.e. the attenuation) is mostly attributed to the drop's energy absorption. Since this is driven by $\mathrm{Im}(K)$, higher values of the parameter determine a stronger absorption and a stronger signal attenuation.

For both water and ice $|K|^2$ and $Im(K)$, vary with temperature and frequency, but overall they are greater for water than ice (2.1). This results in a stronger response of water, which exhibits high scattering and absorption capabilities, than that of ice: liquid drop's reflectivity is higher than solid particles, as well as the absorption of energy by itself and the consequent signal attenuation.

Depending on the dielectric characteristics a different attenuation correction

may be applied. Water has the highest attenuation, so a stronger correction has to be implemented, whereas ice has a lower one and thus requires a smaller correction. The snow particle consists of ice with air inclusions and sometimes it contains water. For this reason, it has a variable dielectric constant depending on its water content: dry snow is highly porous due to the absence of water, so its dielectric constant is lower than that of pure ice, while wet snow has a significant water content, leading to intermediate values between water and dry snow. As a result, the radar signals' attenuation in snow is subject to variation: in dry snow, it is negligible, but in wet snow, it is more significant. In the melting layer the particles are subjected to an intermediate situation in which attenuation varies depending on their mixed-phase composition: a higher water content results in greater signal attenuation due to its higher extinction properties, while a lower value determines a lower extinction value. [2].
Finally, besides the refractive index n and the dielectric constant $|K|^2$, the relative permittivity ϵ is required to fully characterize the particle's scattering properties. The relationship between the refractive index and the relative permittivity is:

$$n = \sqrt{\epsilon_r}, \tag{2.8}$$

where the expression for the complex refractive index n, highlighting its real and imaginary part, is:

$$n = n^{'} - jn^{''}. \tag{2.9}$$

Similarly, the relative permittivity ϵ_r may be described as:

$$\epsilon_r = \epsilon_r^{'} - j\epsilon_r^{''}, \tag{2.10}$$

where $\epsilon_r^{'}$ is the real part of the complex relative permittivity and $\epsilon_r^{''}$ is the imaginary part of it. The imaginary component of the complex relative permittivity is highlighted because it is responsible for absorption processes similarly to $Im(K)$, thus for signal attenuation.

2.2 Backscattering volume

The backscattering power is converted by radars in reflectivity measurements, in fact the reflectivity radar was the first radar ever developed. The reflectivity is a fundamental parameter for precipitation estimation: it is linked to the precipitation intensity and the cloud composition. The measure achieved by the radar is the reflectivity factor (Z), which can be expressed as:

$$Z = \frac{\sum_n D_n^6}{V}, \tag{2.11}$$

where D is the diameter of the raindrop, V is the backscattering volume in which the drops are contained and $\sum_n D_n^6$ is the total contribution to reflectivity of all particles within the given volume, according to their diameter [1].
The Equation 2.11 is valid considering Rayleigh approximation: particles are assumed spherical and with a smaller size than the radar's wavelength. Furthermore, it is obvious that, with Z being proportional to D_n^6, larger particles will scatter disproportionately more than smaller ones, and the received power will be dominated by these bigger targets [2].
The common units for the reflectivity factor are mm^6/m^3, but the equation can be rewritten and referred to a logarithmic scale with units of dBZ:

$$Z(dBZ) = 10 \log_{10}(Z). \tag{2.12}$$

This is the typical unit of measure for precipitation classification.
The observation of clouds through low-frequency weather radars may produce values below -50 dBZ and values around -20 dBZ for lightest drizzle. 10 dBZ is associated with very light precipitation, while heavy rain is generally below 55-60 dBZ and hail is about 60-70 dBZ. Values above 70 or 75 dBZ could be non-meteorological objects, such as buildings or terrain features, and they are called *clutters* [2].
The calculation of the received power, directly proportional to the precipitation intensity, is accomplished by the weather radar equation. A convenient version

for radars with circular parabolic antennas is

$$P_r = \frac{1.22^2 0.55^2 10^{-18} \pi^7 c}{1024 \log_e(2)} \frac{P_t \tau D_a^2}{\lambda^4} \frac{T(0,r)^2}{r^2} |K|^2 Z, \tag{2.13}$$

where P_t is the power of the transmit pulse and τ its duration, D_a is the diameter of the antenna, T is the transmittance of the atmosphere along the path between the radar at range 0 and the sampling volume at range r, and $|K|^2$ is the dielectric constant of scatterers.

The Equation 2.13 is valid when all hydrometeors have the same dielectric constant, they are spherical, they behave as Rayleigh scatterers and they are randomly distributed with a mean density that does not vary within the sampling volume. The first term is about constants, the second depends on radar parameters, the third depends on the path properties and the fourth depends on target properties [2].

The Equation 2.13 can be deployed to retrieve the reflectivity factor Z, when the dielectric constant $|K|^2$ of the particles is known.

As illustrated in Table 2.1, the dielectric constant of the liquid phase is higher than the solid matter, so the power received from rain will be stronger than from a solid ice target. Despite its lower dielectric constant, hail is sometimes associated with high reflectivity: this can be attributed to its larger size compared to rain. At an equal size, rain will result in higher reflectivity because of water's increased dielectric constant. However, hail is usually characterized by larger dimension than rain, so higher values in dBZ will be detected for ice. The situation gets more complex with snow, which is ice with air inclusions and it may be dry or wet, depending on its water content, influencing the dielectric constant and, subsequently, the reflectivity factor.

Because of uncertainties about the scatterers' phase and dimension (thus whether or not they are Rayleigh targets), a new quantity is defined: the equivalent reflectivity factor such that:

$$P_r = \frac{1.22^2 0.55^2 10^{-18} \pi^7 c}{1024\, log_e(2)} \frac{P_t \tau D_a^2}{\lambda^4} \frac{T(0,r)^2}{r^2} ||K_w||^2 Z_e, \tag{2.14}$$

with $|K_w|^2$ being the dielectric constant of liquid water and Z_e the equivalent

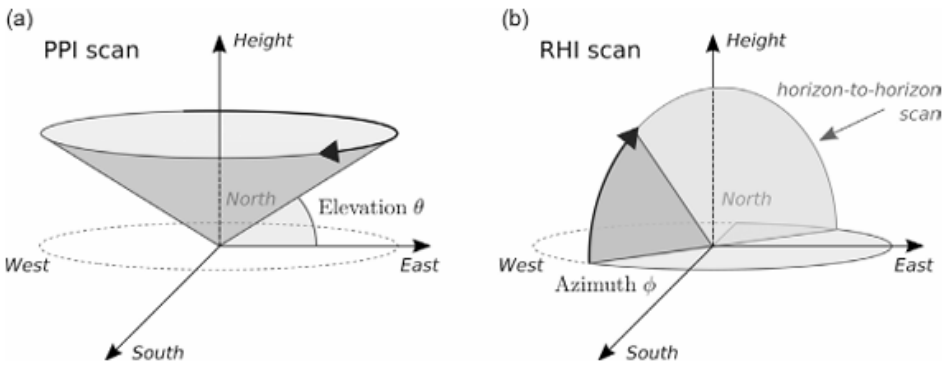

Figure 2.3: Schematic representation of weather radar scan geometries ([1]).

reflectivity factor [2].

Because $|K|^2$ depends on the phase of the scatterers, it is inconvenient to have to adjust it for every target. Thus Z_e is defined as the reflectivity factor that would give the same returned power if the scatterers were liquid water. The equation for Z_e can be written as follows:

$$Z_e = \frac{|K|^2}{|K_w|^2} Z, \tag{2.15}$$

This resolves the uncertainty regarding the particles' phase [2].

2.2.1 Visualization of radar reflectivity

Weather phenomena evolve rapidly in the troposphere, the lower layer of atmosphere investigated by weather radars, so the scanning strategies must ensure an effective trade-off between data accuracy, and spatial and temporal resolution.

Generally, a scanning strategy consists of two types of scans where the radar is located at the centre of the sphere and it can steer its beam in both azimuth and elevation, as shown in Figure 2.3. The first one is the PPI (Plan Position Indicator) and the second one is the RHI (Range Height Indicator) scan. The PPI scan consists of scanning in azimuth at a fixed elevation, while the RHI scans in elevation at a fixed azimuth. Both radar observation geometries are described by three spherical coordinates: range (r), azimuth (ϕ) and elevation (θ).

Reflectivity and Doppler radars provide measurements of the reflectivity factor

and the Doppler velocity [2].

These collected data must be displayed to be interpreted. Weather radar scans collect three-dimensional data, but they are usually rendered on 2-D displays: these are known as radar products. The simplest product is the PPI scan: the reflectivity of all azimuth angles at a given elevation can be rendered through a colour ramp, indicating the precipitation intensity. One of the disadvantages of a PPI display is that there is a systematic change in the observation height with range: close to the ground echoes are originated from near the surface heights, while far from the radar echoes are originated from scatterers located at increasing higher altitudes. To compensate this problem, a CAPPI is usually adopted: it is made by selecting information from all elevation angles, with the aim of generating a display of the weather at a specific level above the sea level [2].

2.3 Attenuation problem and effects

Attenuation is affected by multiple parameters: the radar frequency, the drop size distribution (DSD), the particles' orientation and the temperature. The first concept has already been addressed in the introductory chapter; therefore, the remaining three will be discussed below.

The drop size distribution describes the number of hydrometeors per unit volume as a function of their diameter and, for this reason, it is a key macrophysical property of precipitation, since both scattering and absorption depend strongly on drop diameter. A higher DSD in the large-drop range suggest a predominance of big drops in the precipitation, that cause a higher extinction and, as a result, a higher total attenuation. In contrast, a DSD dominated by small drops produces a weaker attenuation. The extinction for a backscattering volume can be quantified by the extinction coefficient K_{ext}, which measure the signal loss along the radar beam path in dB/km. It is defined as:

$$K_{\text{ext}} = \int_0^\infty N(D)\,\sigma_{\text{ext}}(D)\,\mathrm{d}D, \tag{2.16}$$

where $N(D)$ is the particle size distribution, so the number of particles per unit volume and per unit diameter, and σ_{ext} is the extinction cross section for a particle with a diameter D, expressed in m^2.
As demonstrated in Figure 2.4, for a fixed Rain Water Content (RWC) equal to 1 g/m^3, a frequency of 5.6 GHz (characteristic of a C-band weather radar) and three distributions (one exponential and two gamma) the extinction coefficient K_{ext} increases as the mean mass-weighted diameter D_m increases. D_m is defined as:

$$D_{\mathrm{m}} = \frac{\int_0^\infty D^4 N(D) dD}{\int_0^\infty D^3 N(D) dD}, \tag{2.17}$$

representing the mean drops diameter, weighed according to the their mass.
The particle size distribution $N(D)$, which appears in both Equations 2.16 and 2.17, can be described as a function of three parameters: N_0, μ and Λ. In fact, it is valid that:

$$N(D) = N_0 \, D^{\mu} \, e^{-\Lambda D}, \tag{2.18}$$

where N_0 is the concentration (intercept) parameter, μ is the shape parameter and Λ is the size (slope) parameter. This expression provides a simple way of representing a wide range of rainfall conditions. For example, setting $\mu = 0$ the 2.18 becomes an exponential distribution, while setting $\mu > 0$ different gamma distributions may be defined.

In Fig. 2.4 the extinction coefficient for unit mass is shown as a function of D_m for three DSDs: the exponential distribution ($\mu = 0$) and two gamma distributions ($\mu = 3$ and $\mu = 6$). When the DSD is characterized by larger drops, thus larger D_m, the extinction coefficient gets higher, as well as the attenuation. Secondly, the extinction coefficient varies according to the distribution type, thus according to μ. The exponential distribution includes a big quantity of small drops and, at the same time, a tail of very large drops, while the gamma distributions with $\mu > 0$ for the same RWC value consider a smallest number of big drops . As the shape parameter μ increases, the distribution becomes narrower around the mean D_m: so the $\mu = 6$ distribution predicts fewer big drops rather than the $\mu = 3$ one. The larger drops are responsible for the highest values of K_{ext}: for this reason, the exponential distribution is

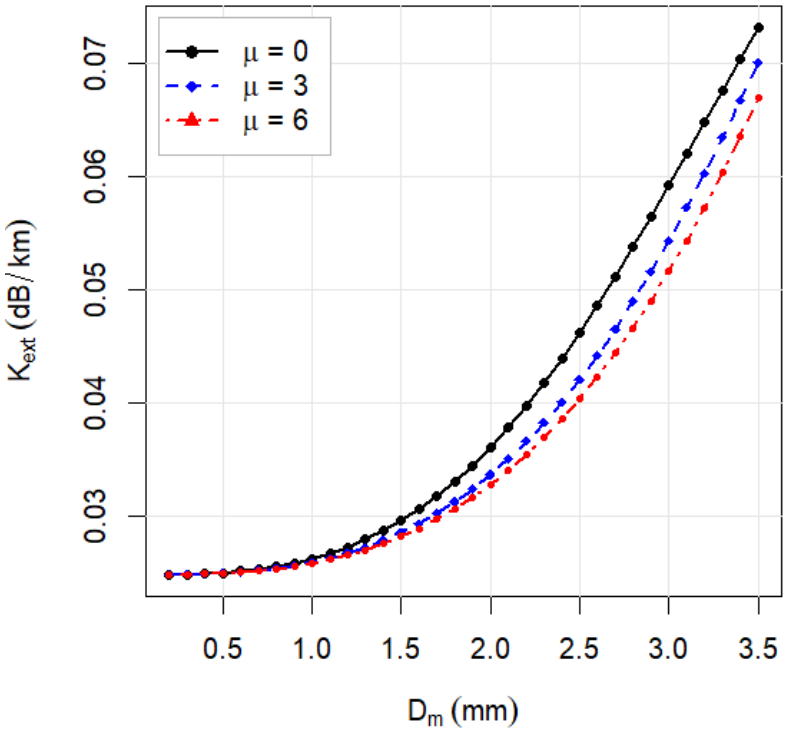

Figure 2.4: Extinction coefficient trend with increasing mean mass-weighted diameter for a C band radar, at a fixed rain water content of 1 g/m^3 and for different drop size distributions (DSD), i.e. the exponential distribution ($\mu = 0$) and two gamma distributions ($\mu = 3$ and $\mu = 6$).

characterized by larger extinction coefficients, rather than the gamma ones.
The second parameter affecting attenuation is the particles orientation and shape. In dual polarization weather radars the horizontally polarized electric field interacts with larger horizontal dimension of the drops, so it is affected by greater attenuation, while the vertically polarized electric field interacts with smaller vertical dimensions, so the attenuation effects are smaller. Indeed, the extinction cross section is different for the horizontal and vertical polarization.
Finally, atmospheric temperature also influences radar signal attenuation. As reported in Table 2.2, at low frequencies an increase in temperature leads to a reduction in the imaginary part of the relative permittivity, ϵ_r, resulting in decreased attenuation. Conversely, at a fixed temperature, higher radar frequencies are associated with an increase in the imaginary component, and consequently, greater signal attenuation.
Moreover, as discussed in Section 2.1.1, absorption processes are closely related to the imaginary part of the dielectric factor, K. Specifically, $Im(K)$ governs the absorption, which in the Rayleigh scattering regime represents the main contributor to signal attenuation. Consistent with the behavior of $Im(\epsilon_r)$, $Im(K)$ decreases as temperature increases, resulting in a corresponding reduction in signal attenuation. [1].

Frequency (GHz)	ε_r			$\lvert K_w \rvert^2$			$Im(K)$		
	0°C	10°C	20°C	0°C	10°C	20°C	0°C	10°C	20°C
2.8	81 - j23	80 - j16	78 - j12	0.934	0.931	0.928	-0.0093	-0.0069	-0.0055
5.6	64 - j37	71 - j29	73 - j22	0.932	0.930	0.928	-0.0194	-0.0141	-0.0108
9.4	45 - j41	55 - j37	62 - j32	0.929	0.929	0.927	-0.0316	-0.0240	-0.0188
13.9	30 - j37	41 - j39	50 - j37	0.923	0.925	0.925	-0.0464	-0.0347	-0.0272
36	11 - j19	14 - j24	19 - j28	0.869	0.894	0.906	-0.1075	-0.0865	-0.0686
95	7 - j8	7 - j11	8 - j13	0.699	0.763	0.811	-0.1655	-0.1634	-0.1450

Table 2.2: ε_r, $|K_w|^2$ and $Im(K)$ values at different radar frequencies and temperatures [1].

2.4 Dual polarization weather radar

Dual polarization radars enabled a significant advancement in weather forecasts and in weather radar system designs.
The difference between radars lie in how echoes are captured, stored, processed and visualized. Polarimetric radars, in particular, introduced new measure-

ments capabilities and visualizations techniques by exploiting the horizontal and vertical components of the electric field.

The wave's polarization depends on the orientation of its electric field. Typically, in dual polarization weather radar, both horizontal and vertical components are observed allowing a good visualization of the precipitation and providing information about hydrometeors in both the horizontal and the vertical dimensions. It is important to mention that, regardless of the polarization type, the wave when transmitting propagates radially outward from the antenna as a spherical wave. So, as the range increases, the curvature of the wave front decreases until it becomes flat: at this point, we can locally approximate the wave as a plane wave [1].

When the electromagnetic wave propagates in the three-dimensional space the first dimension is the propagation's direction, while the second and the third determine the polarization plane, which is perpendicular to the direction of propagation. The vertical and horizontal polarization usually adopted for weather radars is known as linear polarization. The two orientations are determined by the antenna, but it is important to keep in mind that the terms *horizontal* and *vertical* keep an intuitive meaning only when pointing at the 0° elevation angle [1].

The electric field, horizontal and vertical, can be described by a sinusoid, varying through time for a fixed position. However, with a propagating wave it takes additional time to travel a range r (because $\tau = r/c$), so the plane's wave electric field will be at the same time function of both time and range. Therefore, it can be demonstrated that:

$$E = E_0\, cos(\omega(t-\tau)) = E_0\, cos(\omega t - \frac{\omega}{c} r) = E_0\, cos(\omega t - k_0 r), \qquad (2.19)$$

where k_0 is the free-space wave number ($k_0 = \omega/c$) [1].

2.4.1 Polarimetric weather radar measurements

The first additional measure observed with polarimetric radars is the **differential reflectivity**, Z_{dr}. It is calculated as the difference between reflectivities at

horizontal and vertical polarizations and, just as the radar reflectivity factor, it is expressed in logarithmic scale (dB):

$$Z_{dr}(dB) = 10\log_{10}(Z_{dr}) = Z_h(dBZ) - Z_v(dBZ). \tag{2.20}$$

The differential reflectivity provides information about the shape, composition and density of the hydrometeors. It varies depending on composition because of the materials' different relative permittivity, for example: oblate raindrops will have a larger Z_{dr} than hail with the same shape, because of the water's greater permittivity. Examining the dependency with shape, it is observed that high Z_{dr} values are indicative of large drops, while small values indicate small drops. This is justified by the tendency of large droplets to flatten, orienting their major axis horizontally: as consequence, the difference between the horizontal and vertical reflectivity increases. On the contrary, small drops appear quite spherical with comparable vertical and horizontal dimensions. This aspect leads to its combined use with Z for a more accurate rainfall estimation, since Z_{dr} helps to reduce uncertainty about drop size distributions [2].

The second additional observation provided by polarimetric radars is the **differential phase shift** Φ_{dp}, which is a key parameter for attenuation correction. This quantifies the phase difference between the received signals at horizontal and vertical polarization and can be highly informative about the particles' classification and precipitation intensity along the signal path.

The equation for the differential phase shift Ψ_{dp} between the horizontal and vertical polarization at a certain range is:

$$\Psi_{dp} = \Phi_{HH} - \Phi_{VV} = \sigma_{co} + \Phi_{dp} + \Psi_o. \tag{2.21}$$

In Equation 2.21 σ_{co} is the backscattering phase delay, Φ_{dp} is the two-way differential propagation phase and Ψ_o is the phase difference between the two transmit waves at range zero, that is the software and hardware shift typical of each radar design. While the last parameter is range-independent and can be easily eliminated, σ_{co} is range dependent and can introduce strong fluctuations

to Ψ_{dp}. Since Φ_{dp} is expected to be a monotonically increasing function with range, it is generally obtained via a spline interpolation from observed Ψ_{dp} values. Hereafter the notation Φ_{dp} will indicate the differential phase shift retrieved from the observed Ψ_{dp} with spline filtering [2].

Φ_{dp} increases monotonically with range with stronger increase corresponding to regions with larger water contents: its rate of increase is proportional to a combination of factors, which are the number, size and orientation of particles [2].

A greater increase of the two-way differential propagation phase suggests a precipitation characterized at a certain range by large and numerous drops, with major dimension preferentially orientated in the horizontal plane. A very small Φ_{dp} indicates a precipitation with small hydrometeors, such as drizzle, few particles and a bad orientation or more randomly oriented. Along the path there could be a bigger increase at first and then a very small one: this could happen if the number, size and elongation vary with range.

The parameter K_{dp} can be estimated from the differential phase shift Φ_{dp} and it is often used for attenuation correction as well. The specific differential phase shift, K_{dp}, is the rate of change in the phase difference between the two polarizations as the wave propagates and it is usually expressed in $^\circ/km$ through the equation:

$$\Phi_{dp}(r) = \phi_{sys} + 2\int_0^r K_{dp}(r)\, dr, \tag{2.22}$$

where ϕ_{sys} is the system differential phase. At attenuating wavelengths, this quantity can be used to compensate the attenuation of the signal, analogously to Φ_{dp} [2].

Along the path the signal may decrease due to atmospheric gases, but the most relevant effects are introduced by precipitation. The path integrated attenuation depends on the radar wavelength, the composition of the precipitation particles (dimensions, shapes, orientations and phases), and their distribution along the radar beam between the antenna and the target resolution volume. Consequently, the total attenuation cannot be simply accounted for by a constant term in the radar equation, rather a range-dependent estimate and integration

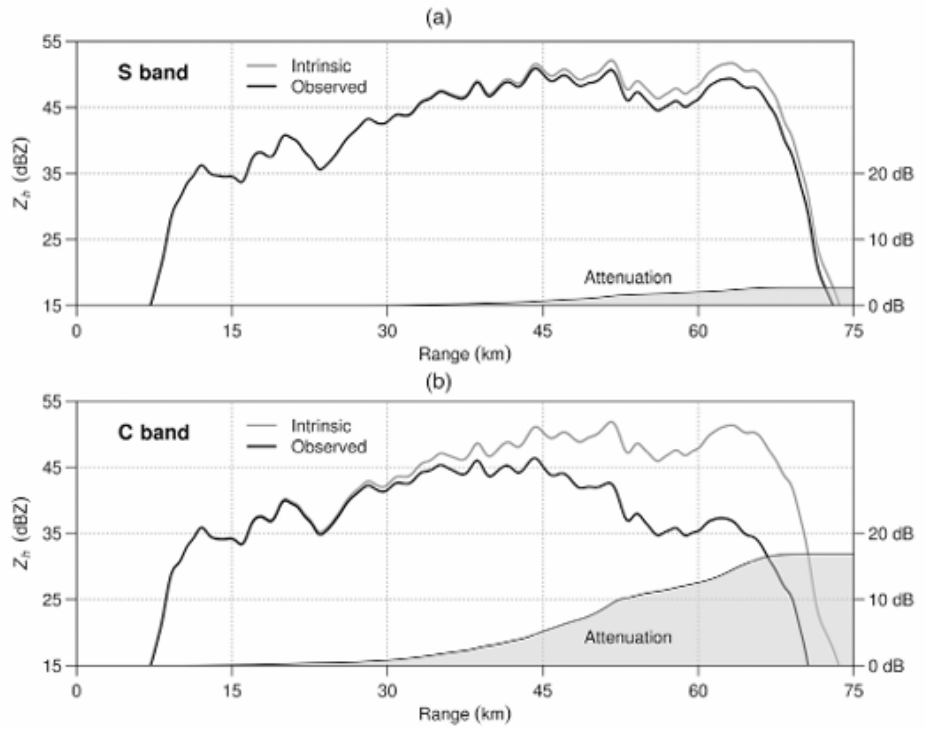

Figure 2.5: Range profiles of simulated reflectivity at S-band and C-band, with the related attenuation estimate ([1]).

along the beam's path must be evaluated. This range-dependent attenuation can be effectively estimated using polarimetric radar parameters, in particular the differential propagation phase Φ_{dp} and its range derivative K_{dp}.

The last introduced measurement is the **copolar correlation coefficient** ρ_{hv} that provides information about the particle's homogeneity within the scan volume: it measures how similar the horizontal and vertical scattering cross-sections of the objects are. A higher ρ_{hv} value is observed in rain, as a result of the consistency of the raindrops' shape and fall behaviour, while lower values are typically observed in the melting layer, where liquid, solid and mixed-phase particles coexist [1].

Attenuation effects are noticeable in all quantitative applications, and can often lead to an underestimation of precipitation due to signal loss. For illustration, the results deriving from S-band and C-band dual polarization radars observations of reflectivity and differential phase shift are presented below. To evaluate the impact of attenuation, measurements are taken along a radial path at a fixed azimuth to simulate radar reflectivity profiles at both S-band and C-band along the propagation path.

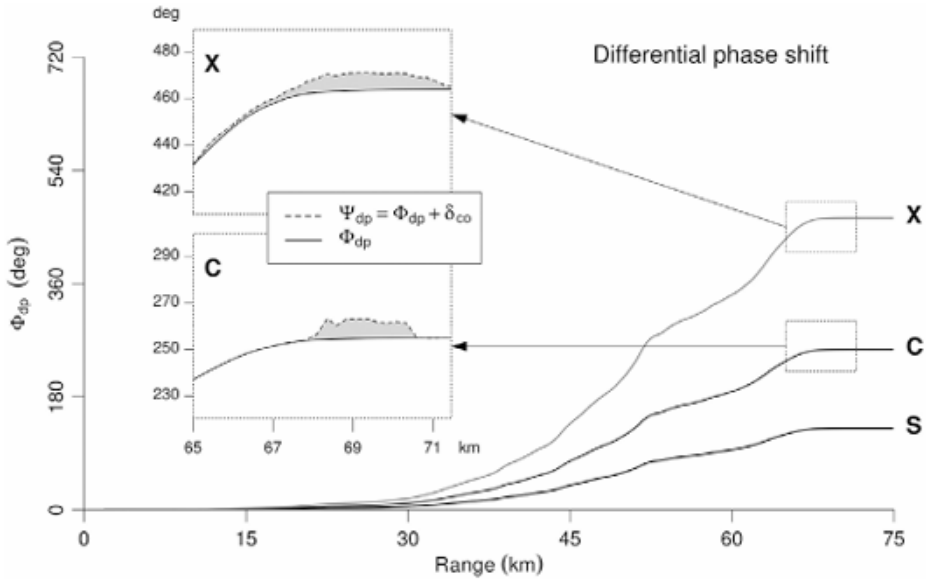

Figure 2.6: Range profiles of differential phase shift at S-band and C-band ([1]).

Attenuation is larger for higher radar frequencies, as shown in Figure 2.5: e.g at C-band rather than at S-band, i.e. at 5.6 GHz vs at 2.8 GHz. Furthermore, as the attenuation increases the rate of decrease in the reflectivity measurement gets significant. [1]

The value of intrinsic or unattenuated reflectivity is quite similar for both frequencies, but the simulated observation shows the increased effect of attenuation for intense rainfall and for C-band in general. The comparison shows that assuming intrinsic values leads to underestimation of measurements, especially when reflectivities exceed 40 or 50 dBZ.

The range profiles of the simulated differential phase shift Φ_{dp} along the same radial (Figure 2.6) confirm what has been discussed above. This proves the relationship between the attenuation and the differential phase shift: Φ_{dp} increases slightly monotonically as the wave travels through the radar path, reflecting the accumulated water content along the radial. When the change rate of this quantity increases, it indicates that the related site may be characterized by a high DSD in larger drops and a favourable orientation. [1]

Measuring the differential phase shift in dual polarization systems has enabled the development of new methods for attenuation correction, which will be discussed in the next section.

2.4.2 Attenuation Correction Methods based on Φ_{dp}

Currently, three Methods are available for attenuation correction: the simple one-parameter method based on the differential phase shift, the Φ_{dp}-constrained methods (the rain-profiling algorithm, based on both the differential phase shift Φ_{dp} and Z_h observations), and a modified version of the rain-profiling algorithm that relies on additional measurements of Z_{dr}.
According to the simple Φ_{dp}-Based Method ([1]) it is true that:

$$A_h = \alpha K_{dp}^b, \tag{2.23}$$

where α (dB/deg) depends on the radar frequency, A_h is measured in dB/km and K_{dp} in deg/km. K_{dp} is proportional to the fourth moment of the DSD, making this parameter very suitable for estimating the specific attenuation of the signal. For weather radar frequencies between 5 and 20 GHz, the coefficient b is very close to the unit value, so the Equation 2.23 can be rewritten as:

$$A_h = \alpha K_{dp}. \tag{2.24}$$

The previous equation can be redefined in terms of intrinsic reflectivity as follows:

$$Z_h(r) = Z'_h(r) + 2\int_0^r A_h(s)ds\,[\mathrm{dBZ}], \tag{2.25}$$

where $Z_h(r)$ is the corrected reflectivity and $Z'_h(r)$ is the observed one.
Therefore, applying the definition of K_{dp} $(\frac{1}{2}\frac{d\Phi_{dp}}{dr})$, the attenuation-corrected reflectivity Z_h at a given range r can be estimated from the observed reflectivity Z'_h and the differential phase shift with:

$$Z_h(r) = Z'_h(r) + \alpha[\Phi_{\mathrm{dp}}(r) - \Phi_{\mathrm{dp}}(0)]\,[\mathrm{dBZ}], \tag{2.26}$$

where $\Phi_{\mathrm{dp}}(0)$ is the system differential phase (ϕ_{sys}).
Since $\Phi_{\mathrm{dp}}(0)$ is usually 0, the 2.26 becomes:

$$Z_{corr} = Z_{obs} + \alpha\Phi_{dp}. \tag{2.27}$$

In conclusion, the observed reflectivity Z_{obs} is underestimated because of the signal attenuation, so adding the estimated attenuation $\alpha\Phi_{dp}$, it is possible to fix the measure and to obtain the corrected reflectivity Z_{corr} [2].
The value of the α coefficient varies according to the radar frequency and temperature; in particular its typical values for the specific attenuation are shown in Table 2.3.

Band (Frequency)	α **value**		
	0°C	10°C	20°C
S (2.8 GHz)	0.022	0.017	0.013
C (5.6 GHz)	0.12	0.11	0.10
X (9.4 GHz)	0.30	0.32	0.34

Table 2.3: α coefficient values (in dB/deg) at different radar frequencies and temperatures.

In addition, α value may vary significantly depending on the DSD according to both A_h and K_{dp} (Figure 1.3).
In order to analyse the variability of the α parameter and to assess the physical consistency of the results, a direct simulation was implemented based on the integration of the scattering cross-sections over a population of raindrops.
The simulation exploits the relationship between the specific attenuation, the horizontal component of attenuation, and the specific differential phase (Equation 2.24), such that:

$$\alpha = \frac{A_H}{K_{DP}}. \tag{2.28}$$

The objective here is the construction of a theoretical model describing the variation of α as a function of the mass-weighted mean diameter D_m, the shape parameter of the drop size distribution μ and the radar operating frequency.
The normalized gamma formulation of the drop size distribution (DSD), introduced in Equation 2.18, is adopted. It can be expressed as:

$$N(D) = N_w\, f(\mu) \left(\frac{D}{D_m}\right)^{\mu} \exp\left[-(4+\mu)\frac{D}{D_m}\right], \tag{2.29}$$

where D is the single drop diameter, D_m is the mass-weighted mean diameter, N_w is the normalized intercept parameter, μ is the shape parameter and $f(\mu)$ is a normalization term.

In this formulation, the slope or size parameter of the gamma distribution is no longer independent, but depends explicitly on D_m according to:

$$\Lambda = \frac{4+\mu}{D_m}. \tag{2.30}$$

Although mathematically equivalent to the classical gamma formulation, the normalized representation provides a more explicit link with the microphysical properties of precipitation, since both D_m and N_w have a direct physical interpretation in terms of drop size and concentration.

In the simulation, values of D_m and μ consistent with realistic precipitation scenarios are considered. Specifically, D_m is varied between 0.7 mm and 3 mm, while μ assumes representative values corresponding to exponential and gamma distributions (μ= -1, 0, 3, 6).

For individual drops of diameter D, the elemental contributions to horizontal specific attenuation $a_h(D)$ and specific differential phase $k_{dp}(D)$ are integrated over the entire DSD according to:

$$A_H = \int_0^{D_{\max}} a_h(D)\, N(D)\, dD, \tag{2.31}$$

$$K_{DP} = \int_0^{D_{\max}} k_{dp}(D)\, N(D)\, dD. \tag{2.32}$$

The upper integration limit is imposed as:

$$D_{max} = 2.5\ D_m. \tag{2.33}$$

This constraint is introduced to prevent numerical instabilities and to limit the influence of unrealistically large drop diameters, ensuring physical consistency of the model. Once A_H and K_{DP} are computed, their ratio provides the theoretical estimate of the α coefficient.

The variability range of α is analysed for radar frequencies of 5.6 GHz (C-band) and 9.4 GHz (X-band), as shown in Figure 2.7.

As observed in Figure 2.7a, the variability range for C-band radars spans from a minimum value of approximately 0.06 dB/deg for D_m around 2 mm to a maximum value of about 0.28 dB/deg for lower D_m values. In contrast,

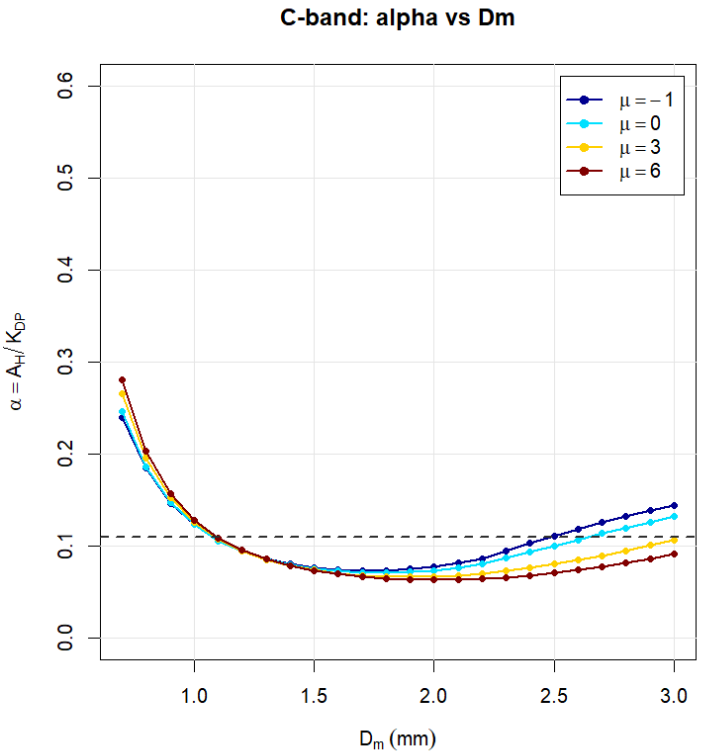

(a) Alpha variability for C-band radars.

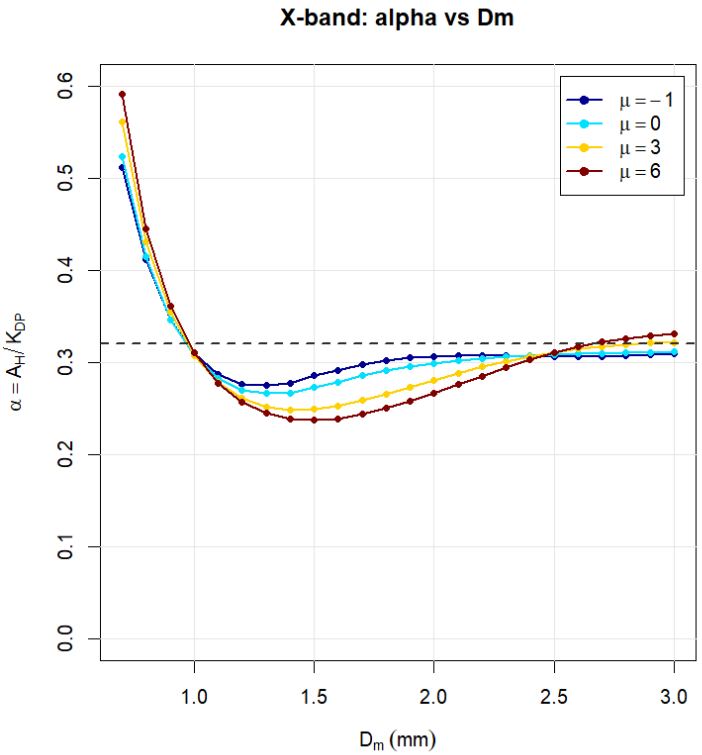

(b) Alpha variability for X-band radars.

Figure 2.7: Variability of the α-parameter for C- and X-band radars for increasing D_m and DSDs with different μs.

the α coefficients obtained for X-band are systematically higher, consistently with the higher operating frequency. Values range from approximately 0.23 dB/deg for D_m around 1.5 mm up to 0.59 dB/deg for the smallest D_m values. The dashed lines indicate the operational values commonly adopted by Arpa, equal to 0.11 dB/deg for C-band and 0.34 dB/deg for X-band.

The highest α values are associated with low D_m. Under these conditions, raindrops are predominantly small and nearly spherical, with similar horizontal and vertical dimensions. As a consequence, the specific differential phase K_{DP} assumes very small values, while the specific attenuation A_H remains appreciable. The resulting small denominator leads to relatively large α values.

As D_m increases, drops become larger and increasingly oblate due to aerodynamic deformation. This enhances the differential phase shift and increases K_{DP}, causing α to decrease progressively up to approximately D_m=2.2 mm for C-band and D_m=1.5 mm for X-band.

A similar behaviour is observed when analysing the dependence on the shape parameter μ. Exponential distributions (μ=0), which allow for a more pronounced tail of larger drops, are associated with higher α values. Conversely, gamma distributions with μ>0 are characterized by narrower spectra with fewer extreme diameters, leading to lower α coefficients.

The second Method available for attenuation correction is the Φ_{dp}-Constrained Method ([1]), also known as Rain-profiling Algorithm (RPA). This builds on the previous method: while the simple Φ_{dp}-Based Method derives the specific attenuation locally from K_{dp}, making it susceptible to noise in the K_{dp} trend estimation, the RPA deploys a full profile of measured attenuated reflectivities to reconstruct attenuation. Furthermore, it uses the total change in differential phase, $\Delta\Phi_{dp}$, measured over the whole volume scan, as a global constraint that must be distributed correctly along the radar path. In fact, the 2.24 becomes:

$$\int_{r_{\min}}^{r_{\max}} A_h(s)\, ds \;=\; \alpha \int_{r_{\min}}^{r_{\max}} K_{dp}(s)\, ds, \tag{2.34}$$

where $A_h(s)$ is expressed as a power-law function of the intrinsic reflectivity:

$$A_h(s) = a\; Z_h(s)^b. \tag{2.35}$$

This leads to a more stable solution, that is unaffected by signal noise.
The last methodology, the Dual Polarization Rain-Profiling Algorithm (DRPA), generalizes the RPA by incorporating the differential reflectivity measurements [1]. The algorithm maintains the Φ_{dp} constraint while simultaneously modulating the attenuation profile with the spatial structure of $Z_h(r)$ and $Z_{dr}(r)$:

$$\begin{cases} A_h(r) = f\Big(Z_h(r), Z_{dr}(r)\Big) \\ \int A_h(s)\, ds = \alpha \int K_{dp}(s)\, ds \end{cases} \tag{2.36}$$

This leads to an even more accurate attenuation correction [1].
For the purposes of the optimization methodology, the simple Φ_{dp} - Method has proven to be both robust and suitable for estimating the attenuation coefficients; consequently, it has been adopted for this study.

Chapter 3

Methodology for the Optimization of attenuation coefficients in C- and X-band radar systems

Arpa (Agenzia Regionale per la Protezione Ambientale) is a national environmental agency established by the Italian public administration and operating in every region in Italy, except Trentino-Alto Adige. The aim of Arpas is to protect the environment by verifying and classifying environmental parameters and communicating them to civil protection bodies [**Wikipedia-Arpa**].

3.1 Arpa Radars description

The dataset employed for the implementation and validation of the methodology consists of observations acquired from three radar systems:

- Bric della Croce
- Monte Settepani
- Druento

The Bric della Croce and Monte Settepani radars operate at the C-band, i.e. at a frequency of 5.6 GHz, while the Druento radar operates at the X-band,

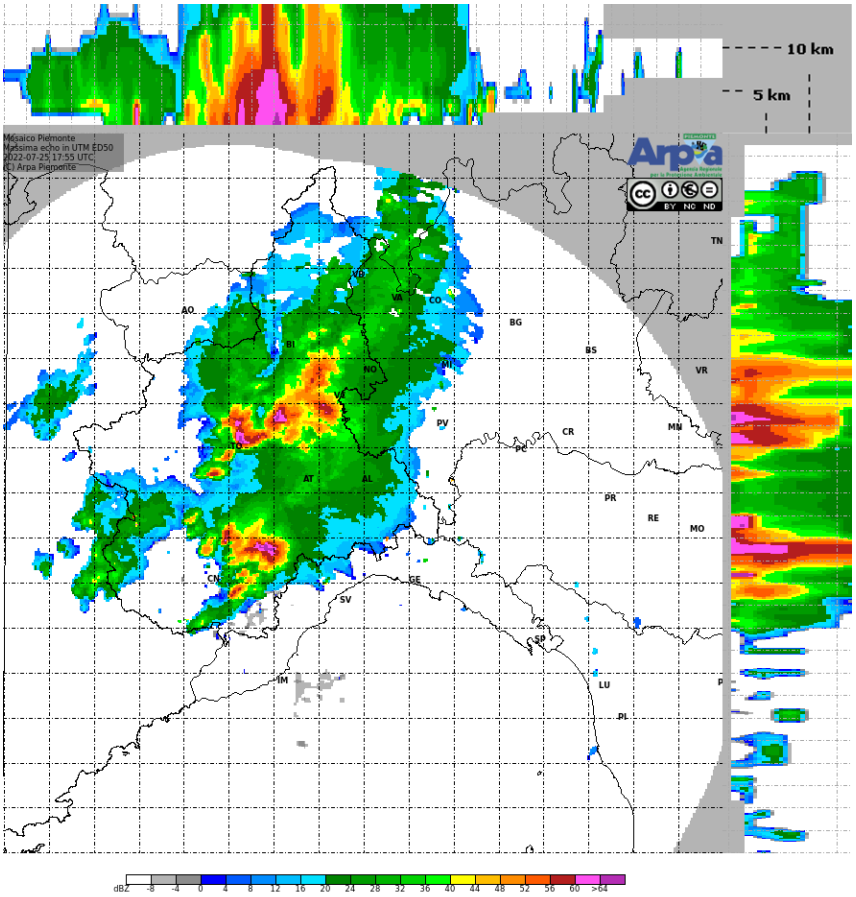

Figure 3.1: Precipitation map resulting from the Bric della Croce and Settepani radars, where the precipitation is measured with reflectivity in dBZ.

with a frequency of 9.4 GHz [3], [4].

The position of the three listed radars enable a real-time precipitation mosaic to be constructed. By combining their measurements, Arpa offers a mosaic updated every 5 minutes, corresponding to the time required to perform a volume scan, which maps the areas of Piedmont and Liguria [3], [4]. Figure 3.1 shows an example of a radar mosaic, representing 25 July 2022 at 17:55. Precipitation is described using a colour scale based on the observed reflectivity.

The Bric della Croce and the Druento radars are located in the province of Turin, in Piedmont: specifically, the former is located in Pecetto Torinese and the latter in Druento. The third radar, Monte Settepani, is located in Liguria, more precisely in Bormida, in the province of Savona. Their altitudes and coordinates are shown in Table 3.1 [4], [5].

Furthermore, the characteristics of each instrument differ in terms of the number of bins and radial resolution; therefore the coverage varies according

	Bric della Croce	Settepani	Druento
Latitude	45.034	44.247	45.137738
Longitude	7.733	8.199	7.598095
Altitude (MSL)	736 m	1390 m	268 m

Table 3.1: Geographical coordinates and altitudes of the dataset radars.

to the maximum range. Taking into account the number of bins (n_{bin}) and the range resolution (r_{res}), it is possible to estimate the maximum distance measured ($s_{r,max}$) by each radar using the following equation:

$$s_{r,max} = r_{res}\, n_{bin}, \tag{3.1}$$

where, n_{bin} corresponds to the number of cells within the radar range and the radial resolution r_{res} measures the width of each cell.

	Bric della Croce	Settepani	Druento
Radial resolution	340 m	250 m	150 m
Number of bins	500	690	267
Maximum range	170 km	172 km	40 km

Table 3.2: Range characteristics of the dataset radars.

Table 3.2 reports the main instrumental specifications, namely the number of bins, the resolution, and the maximum detection range [5].
The angular resolution of the radars, on the other hand, is the same for all of them and is equal to 1 degree. For this reason, the azimuths are distributed from 0 to 360 degrees in increments of 1.

With regard to the investigated elevations, Table 3.3 shows the values of the elevation angles, with their respective identification index.

3.2 Radar network advantages

A key advantage of this network configuration is the presence of overlapping radar beams, which provides common sampled volumes between the radars. This overlap is fundamental for inter-radar calibration and for improving attenuation correction [5].
For a single radar to effectively cover a large area, its design must be scaled

Bric della Croce		Monte Settepani		Druento	
idx	elev [°]	idx	elev [°]	idx	elev [°]
0	0.5	0	-0.3	0	4.5
1	1.2	1	0.7	1	7.0
2	2.0	2	2.1	2	10.0
3	3.0	3	4.0		
4	4.4	4	6.4		
5	5.8	5	9.7		
6	7.4	6	15.0		
7	10.0	7	28.5		
8	15.0				

Table 3.3: Elevation angles and relative indices for each radar. Elevation indices start at 0 and are defined locally for each radar.

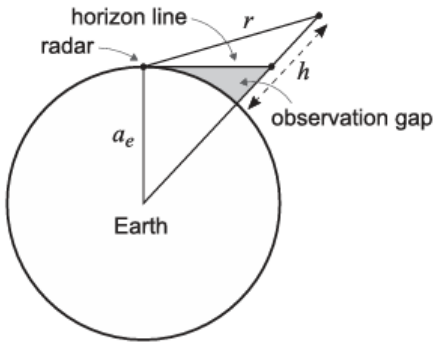

Figure 3.2: Diagram of the beam visibility at increasing range above surface due to Earth's curvature ([1]).

up in terms of size and complexity. While radars' performance is evolving rapidly in line with technological advances, it is also true that a network of smaller radars is more effective than a single large radar. The introduction of spatially distributed networks of weather radars marks a shift in the way weather observation networks are designed and characterised, as they are now evaluated using fundamentally new performance metrics compared to those traditionally used for single radars [1]. For example, a weather radar coverage is limited due to Earth's curvature, and it decreases as the distance from the radar antenna increases, as shown in Figure 3.2.

Additionally, it is important to mention that the enhancement of single radar technology leads to the enhancement of the system radar network.
When a network of radars is used to observe weather phenomena, there are

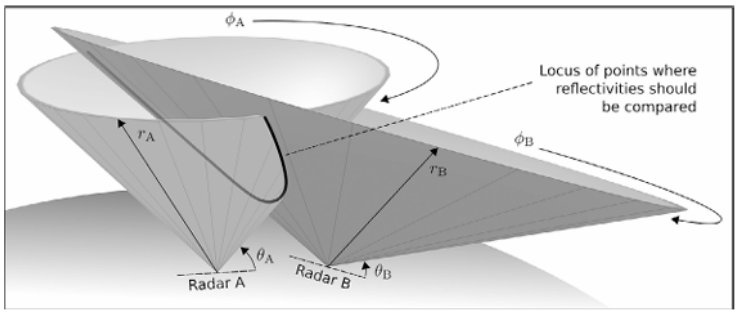

Figure 3.3: PPI scans intersection for network calibration ([1]).

important considerations to take into account. A common reference level is used as the basis for calibrating all the radars belonging to the network. However, they are rarely calibrated at the end-to-end level, meaning it is possible for the calibration of a system to deviate from that of neighbouring nodes in the network at some point. All radars in a network with a significant overlap ratio (a tight network) can be used for relative calibration alignment using their observations routinely collected during precipitation events [1].

Considering the intersection of two PPI scans, as shown in Figure 3.3, and assuming an idealised scenario in which the geometry of the radar resolution volumes (i.e. their size and orientation) is neglected and measurement uncertainties and calibration errors are absent, the observations associated with the common sampled volumes at the intersection of the radar cones are expected to coincide. In practice, measurement uncertainties lead to a spread around the regression line, whose intercept along the reflectivity axis represents the relative bias between the two radars. [1].

To illustrate the procedure commonly adopted for inter calibration between two radar systems, the C-band Monte Settepani radar and the C-band Bric della Croce radar are considered. They both belong to Arpa Piemonte dataset and they are situated at a distance of 95 km. The calculation is performed by identifying common sampling volumes between the two radars. In particular, only those radar bins are selected for which the difference in slant range is less than 20 km and the difference in beam height is smaller than 100 m, as shown in Figure 3.4 in Panel a. The measurements in these points are plotted with a scatter plot and then corrected from the calibration bias, eliminating the intercept of the regression line (Figure 3.4 Panel b).

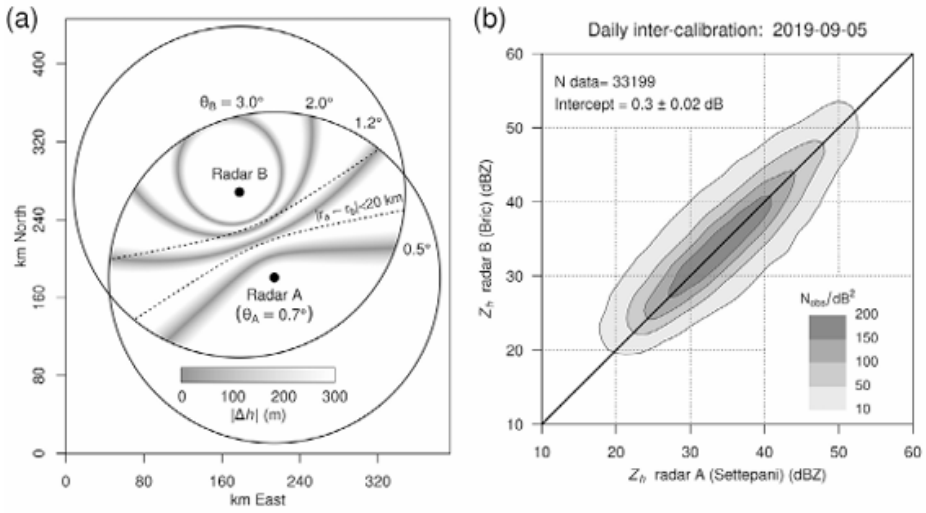

Figure 3.4: Selected points with Δh below 100 m and with Δr below 20 km ([1]).

In the example, the surface projection includes the points at which the 0.7° elevation of the Settepani radar (radar A, 1400 m mean sea level [MSL]) intersects with four low-level scans (0.5°–3.0° elevation) of the Bric della Croce radar (radar B, 740 m MSL). The difference in beam height, or Δh, between the two scans is shown by the grey shading, while the area where the range from the two radars differs by less than 20 km is shown by the dotted lines. The Z_h–Z_h calibration scatter plot deploy observations where $\Delta h < 100\,\text{m}$ (to ensure good matching in the vertical) and $|r_A - r_B| < 20\,\text{km}$ (to ensure a similar size of resolution volumes). Lastly, the contamination by the melting layer, large precipitation gradients, or other artefacts is avoided by using only measurements with $\rho_v > 0.94$ [1].

These constraints guarantee the optimal matching along the direction perpendicular to the ground and maintain comparable sizes for the resolution volumes.

3.3 Optimization methodology

The methodology developed within this Thesis is based on the conventional inter calibration procedure, through which attenuation is evaluated at radar beam intersection points and the corresponding attenuation coefficients are subsequently derived. The individual steps of the procedure are presented

below and thoroughly described in the following sections of this chapter:

- Identification of overlapping backscattering volumes;
- Data filtering and manipulation at intersection points, through visibility maps, geometrical considerations and differential phase shift;
- Radar products extraction including reflectivity, differential phase shift, specific differential phase shift and copolar correlation coefficient;
- Reflectivity correction with the Φ_{dp} - Method using fixed coefficients (2.3);
- Estimation of optimized attenuation coefficients through linear regression applied to measured reflectivity values;
- Reflectivity correction with the Φ_{dp} - Method using optimized coefficients.

The first step of the methodology involves identifying the overlapping backscattering volumes of the chosen radar pair. Then the two radar rays corresponding to the two radars can be extracted. The reflectivities, the differential phase shift, the specific differential phase shift and the copolar correlation coefficient along the rays can be used to attempt a first attenuation correction based on the Φ_{dp}-Based Method (Equation 2.26), by selecting a fixed α-coefficient for the specific radar frequency as shown in Table 2.3. This will later be exploited for comparison with the results obtained from the optimisation analysis, therefore with the optimised α-coefficients. It is expected that the dataset corrected with the optimised coefficients will be characterised by a lower dispersion than the dataset corrected with the fixed Arpa coefficients.
The first analysis will focus on two C-band radars with the same attenuation coefficient, i.e. the Bric della Croce and Monte Settepani radars, while the second one will focus on two radars with different operating frequencies, i.e. the Bric della Croce (C-band) and Druento (X-band) radars.

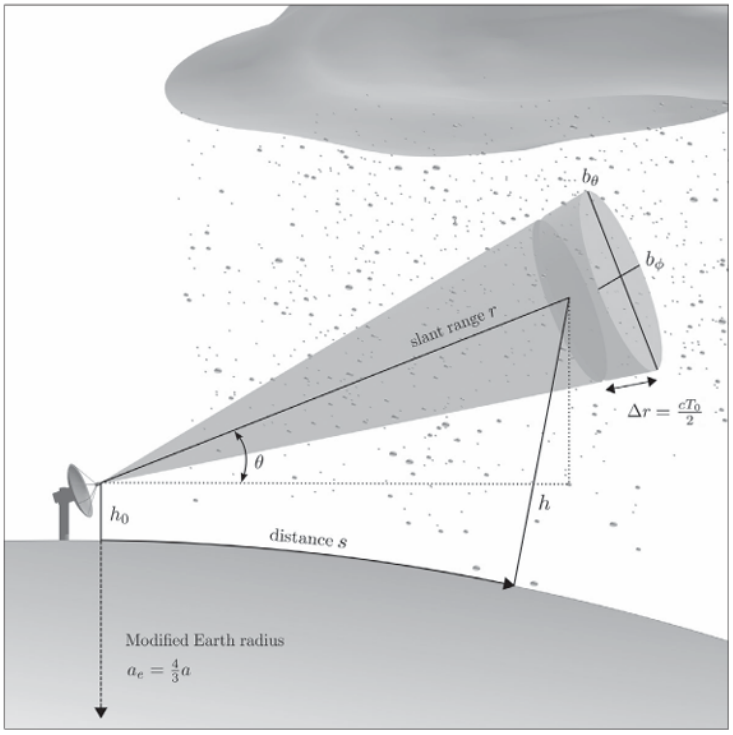

Figure 3.5: Slant range and beam height schematic illustration ([1]).

3.3.1 The identification of overlapping backscattering volumes

In order to determine the intersection points, it is necessary to estimate both the slant range and the radar beam height (Figure 3.5).

In this regard two functions, one for the slant range and one for the beam height above the sea level, are applied. The primary purpose of the slant range function is to convert the horizontal distance between the radar antenna and a given target into the actual line-of-sight distance (slant range) travelled by the radar signal along its propagation path from the transmitting antenna to the target. This step is crucial for georeferencing radar measurements, as radar data are inherently collected along the slant range and must be projected onto a geographic coordinate system. The function arguments are, in fact, the horizontal range between the radar and the target, measured in m, the elevation angle of the radar beam, expressed in degrees (°), and the height of the radar antenna above the sea level, in m. The calculation relies on the definition of the Effective Earth Radius, or R_{eff}, which is set to the value of $8504182.66\,m$.

This value is larger than the real Earth's radius r_E because it comprehends a refractivity constant (considering the 4/3 model) to compensate for the effect of atmospheric refraction along the radar beam [5].

As discussed in the previous chapters, the electromagnetic wave is refracted in the atmosphere due to the refraction index variation based on the temperature trend: as a result, the radar beam gets deviated with respect to its linear path. Therefore, to simplify the problem, a greater radius for Earth is assumed in order to consider a straight line path, as if there were no atmosphere or refraction. The equation for the Effective Earth Radius is:

$$R_{eff} = \frac{4}{3}\, r_E, \tag{3.2}$$

where $\frac{4}{3}$ approximate the refractive effect in the atmosphere.

Once converted the elevation angle from degrees into radians, the following equation is adopted for the slant range calculation:

$$s_r = \frac{(R_{eff} + h_r)\, \frac{d}{R_{eff}}}{cos(\theta + \frac{d}{R_{eff}})}, \tag{3.3}$$

where R_{eff} is the Effective Earth Radius, h_r is the radar height above the mean sea level, d is the horizontal distance between the radar and the target and θ is the elevation angle in radians [5].

The second function defined for the intersection points calculation is the radar beam height function. When observing at small ranges, close to the radar, the surface can be assumed as flat without being affected by a significant error in the measurements. However, as the range increases, the error in the estimated beam height on the surface level become not negligible because of Earth's curvature (3.2). The aim is to determine the altitude corresponding to a given slant range, and thus a specific ground position, by converting radar observations from polar coordinates (range and angle) into actual height coordinates, accounting for the effective Earth radius (R_{eff}). The function takes as inputs the slant range, the radar height (MSL) expressed in m and the radar beam elevation angle in degrees (°). The calculation is based on the application of the *Law of Cosines* of the triangle formed by the centre of the Earth, the radar antenna and the

target point. The following Equation 3.4 returns the Height above Mean Sea Level (MSL) at a certain slant range, in meters:

$$h = \sqrt{s_r^2 + (R_{eff} + h_r)^2 + 2\, s_r\, (R_{eff} + h_r) \sin(\theta)} - R_{eff}, \tag{3.4}$$

where h is the height of the radar beam, s_r is the slant range, R_{eff} is the Effective Earth Radius, h_r is the height of the antenna above the mean sea level and θ is the radar beam elevation angle [5]. Consequently, the vertical tolerance for the beam intersections is defined and set to 500 m.

This parameter, together with the radar beam altitudes h, enables the intersection points for each radar pair to be identified. Firstly, the elevation angles and position of each radar are defined. Then, the beam height function is applied to each radar bin and the results are stored for subsequent steps. By constructing a common Cartesian grid, the beam height measurements, h, are mapped, and the vertical overlap is determined whenever the vertical separation between two radar beams falls below the specified vertical tolerance. Finally, all intersection points are exported to a text file for further analysis. For the present study, two separate files are generated: one corresponding to the Bric–Settepani radar pair and another for the Bric–Druento radar pair.

Each file is structured so that each row represents a single intersection point, and the columns record the associated following radar physical parameters, facilitating subsequent quantitative analysis and processing:

- Row number, i.e. the intersection point number;
- Elevation angle value of the first radar;
- Index of the elevation angle of the first radar;
- Azimuth value corresponding to the first radar;
- Range bin value corresponding to the first radar;
- Elevation angle value of the second radar;
- Index of the elevation angle of the second radar;
- Azimuth value corresponding to the second radar;

- Range bin value corresponding to the second radar.

3.3.2 Data filtering and manipulation at intersection points

Given the computational burden of the analysis, before extracting the radar variables, a selection of the points within the overlapping volume must be performed.

3.3.2.1 Visibility Maps

Firstly, the intersection points are subjected to a filtering based on Visibility maps. The radar signal encounters obstacles along its path, including mountains, trees and buildings, which are defined as *clutters*. These represent an undesirable component within the radar signal, as they generate echoes that do not come from the meteorological targets to be described, but they are derived from obstacles encountered by the electromagnetic wave along its path. This unwanted echo would create errors in the measurement of attenuation and, consequently, in the estimation of precipitation (QPE). Therefore, it is typically managed using visibility maps. For this thesis project, maps are created in ESRI ASCII Grid format, which represents a polar grid.

Visibility maps indicate the points that are visible to the radar. The numerical values indicate the elevation index corresponding to the minimum elevation angle required for the point to be visible. Consequently, if a lower value is reported in a cell, it means that that point is easily visible, so there are probably no major obstacles between the radar and the cell. Conversely, if the value is high, it means that the point will only be visible when the radar beam has a high elevation angle. This happens, for example, when there is a mountain along the radar's line of sight: points behind the mountains will not be visible unless the elevation angle is high enough. In some cases, certain points are completely obscured, so the value indicated by the visibility map is beyond the radar's range and will not be measured by it.

By utilizing visibility maps, only intersection points with elevations exceeding the thresholds defined on the map are retained, effectively removing locations

that may produce unwanted backscatter or clutter, which could compromise the quality and reliability of the radar measurements.

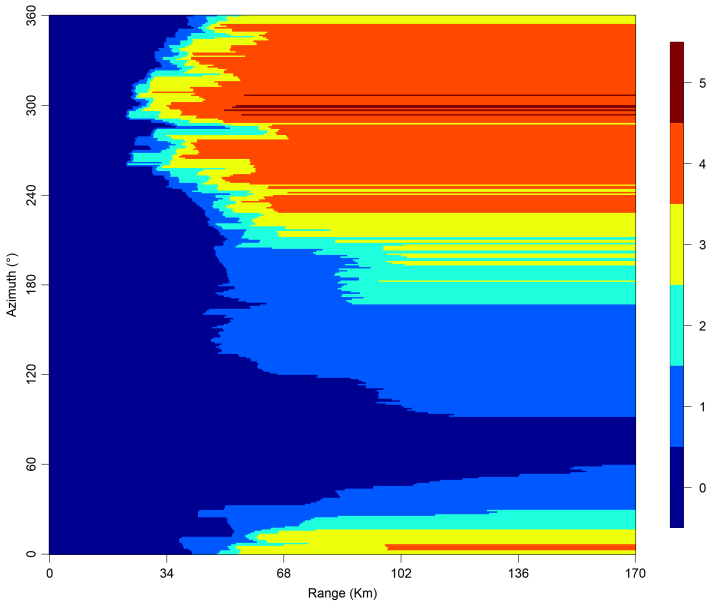

(a) Bric della Croce radar Visibility Map

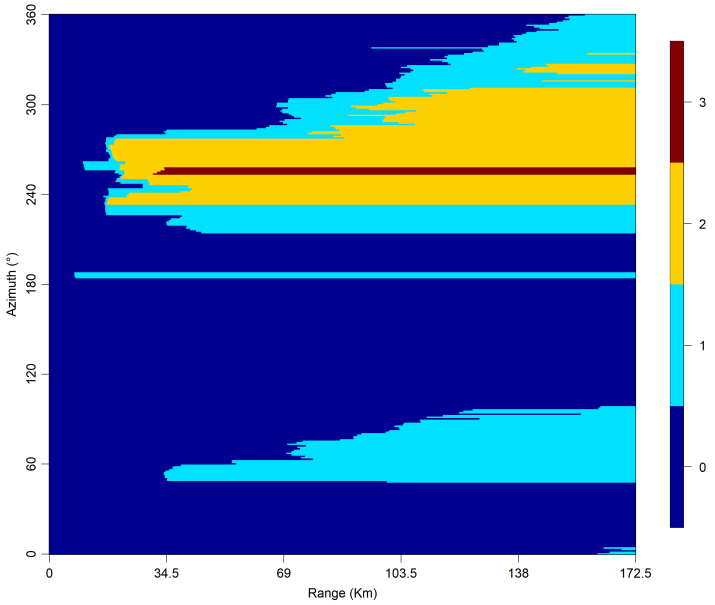

(b) Monte Settepani radar Visibility Map

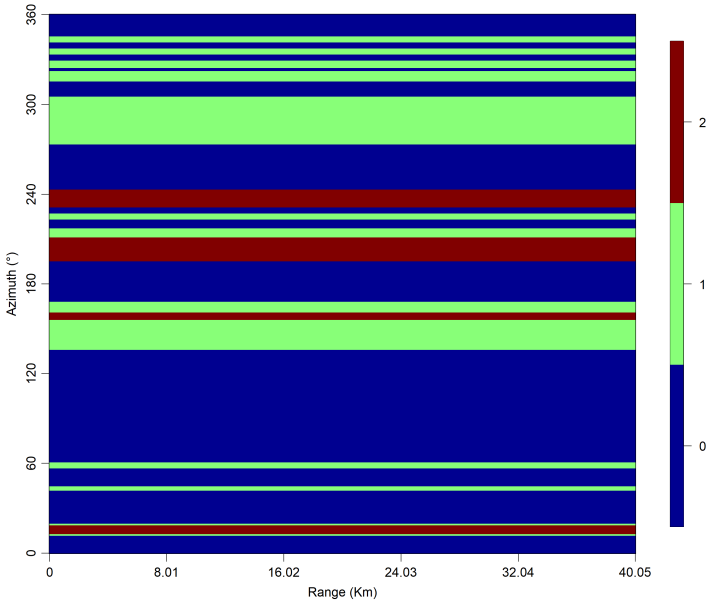

(c) Druento radar Visibility Map

Figure 3.6: Visibility Maps for Bric della Croce, Monte Settepani and Druento radars, indicating the elevation index corresponding to the minimum elevation angle required for the point to be visible. The x-axis indicates the range, i.e., the radial distance from the radar, while the y-axis defines the azimuth angle, measured clockwise from geographic north (0°).

Considering the elevations and the elevation indexes shown in Table 3.3, the visibility maps for Bric della Croce, Monte Settepani and Druento radars are shown, respectively, in Figure 3.6 in Panel 3.6a, 3.6b and 3.6c.

The Bric della Croce and Monte Settepani maps highlight their proximity to the Alps mountains: the low elevations that characterise the first volumetric scans experience the occlusion created by the mountain range. Only mountainous terrain is considered as a potential obstacle for these radars, as their positions and elevations ensure that trees do not obstruct the radar beams, contrary to Druento radar. In the latter, due to its position and elevation, in fact, the occlusion is mainly linked to trees surrounding the measurement area. For this reason, thanks to a recently acquired drone image (2025), the surrounding tree cover is analysed and, in particular, the occlusions are evaluated in relation to the heights of the tree crowns. By selecting the occluded areas as azimuth ranges for each elevation angle, the visibility map is then displayed.

In conclusion, a point is considered visible and suitable for analysis only if its elevation exceeds the threshold specified in the visibility maps for the corresponding radar pair, ensuring that it is within the line of sight of both

radars.

3.3.2.2 The geometrical and the differential phase shift filtering

Further data filtering is applied based on the distance from the radars and the height of the radar beam.

For the first radar pair, both operating at C-band, the intersection points are filtered according to a maximum distance threshold from each radar. This ensures that the points are not excessively distant from either radar, so that the illuminated radar cells maintain comparable sizes. In fact, due to the conical shape of a radar beam, the backscattering volumes tend to widen with distance. By enforcing the distance threshold, each cell contains a uniquely defined and spatially unambiguous intersection point.

The equation used for this purpose is:

$$|s_r^{(1)} - s_r^{(2)}| < \Delta r_{max}, \tag{3.5}$$

where $s_r^{(1)}$ and $s_r^{(2)}$ are the ranges from the first and second radar, while Δr_{max} is the chosen threshold for the maximum difference in range.

A different filtering approach is required for the second radar pair, consisting of the C-band and X-band systems. Since this pair is separated by a shorter distance than the previous one (15 km versus 95 km), the radar beams do not expand significantly with range. Therefore, excluding points that are too far from the radars is unnecessary. Instead, points located very close to either radar correspond to very small azimuthal extents of the beam, which in turn lead to unrealistically small backscattering volumes. To prevent this, a minimum distance threshold is applied to both radars.

The relationship that allows this selection to be applied is:

$$|s_r^{(1)}| > r_{min}, \tag{3.6}$$

$$|s_r^{(2)}| > r_{min}, \tag{3.7}$$

where $s_r^{(1)}$ and $s_r^{(2)}$ are the distances in range from the first and second radar and r_{min} is the threshold chosen for the minimum distance.

Next, a second geometric constraint is applied to the radars beam height. This threshold is required to exclude intersection points located above the melting layer, where precipitation is solid or only partially liquid. Within the melting layer, snow and ice particles begin to melt and become coated with a thin layer of water. In this condition, wet particles scatter radar signals similarly to large raindrops, producing a pronounced peak in measured reflectivity known as the *bright band* [2].

The attenuation coefficients reported in Table 2.3 are valid only for liquid precipitation. As explained in Section 2.1.1, applying attenuation coefficients calibrated for rain within the melting layer would lead to an overcorrection of the reflectivity and, consequently, to its overestimation.

Lastly, it is also decided to exclude intersection points characterised by a low differential phase shift. This allows points characterised by significant attenuation to be selected: in this way, the attenuation coefficients will be calibrated according to the points where the phenomenon is actually occurring. The threshold adopted for the C-band pair is 15°, specifically it is imposed that:

$$|\Phi_{dp}^{(Bric)} - \Phi_{dp}^{(Sett)}| > 15^\circ \tag{3.8}$$

Since the radars operate at the same frequency, we are interested in constraining the phase difference between the two systems below a given threshold, rather than considering their individual values separately.

By contrast, the threshold adopted for the Bric–Druento radar pair is differentiated according to radar frequency. A threshold of 15° is retained for the differential phase shift measured by the Bric della Croce radar, while the threshold is increased to 25.5° for the Druento radar, owing to its higher operating frequency. This approach enables direct comparison between measurements from the X-band radar, which experiences higher attenuation, and the corresponding measurements selected from the C-band radar. Notably, X-band attenuation is approximately 1.7 times greater than that of the C-band, and the adopted thresholds preserve this proportional relationship for consistency. Therefore, in short, the setting is:

$$\Phi_{dp}^{(Bric)} > 15^{\circ} \tag{3.9}$$

$$\Phi_{dp}^{(Druento)} > 25.5^{\circ} \tag{3.10}$$

3.3.3 Extraction of radar products from overlapping backscattering volumes

The first step in the analysis is the identification of overlapping backscattering volumes for each pair of radars. Measurements are extracted from netCDF (Network Common Data Form) files, containing radar informations for each scanning instant and for each radar involved in the analysis.
Specifically, each file can be regarded as a three-dimensional data structure that stores time-fixed and geolocated radar product values. A netCDF file is generated for each radar scan, serving as the starting point for radar data analysis and, in particular, for the estimation of attenuation and attenuation coefficients.
For each instrument and event the following parameters are extracted:

- Scan time;
- Azimuth angles;
- Range in kilometres;
- Measured (attenuated) reflectivity;
- Differential phase shift;
- Copolar correlation coefficient.

The first extracted variable is the scan time. This choice is motivated by the fact that, when the acquisition times of the two radars over the same cell are sufficiently close, both instruments are likely observing the same target. Precipitation and meteorological targets generally evolve and move rapidly; therefore, acquisitions separated in time, even if referring to the same spatial location, may correspond to different meteorological conditions. In such cases,

the resulting attenuation estimate at that point would be inaccurate.

Another important variable is the azimuth angle. The ideal viewing configuration occurs when the radar beams are aligned, i.e., when the difference between their azimuth angles is within ±30°. This is justified by the geometry of the radar resolution volumes and their overlap. At central beam intersections, the overlapping region is more compact and better defined, leading to a more consistent sampling volume and reduced spatial ambiguity. In contrast, lateral intersections produce an oblique and elongated overlap, increasing spatial ambiguity and observational uncertainty. Therefore, measurements at central intersections are more reliable, and the azimuth difference between the two radars can be used to identify the most suitable region of interest.

The extraction procedure is more complicated when it comes to the differential phase shift and the specific differential phase shift. The methodology involves retrieving the differential phase shift from the netCDF file, applying the necessary filtering, and then using it to compute the specific differential phase shift. The details of the calculation are specified in Appendix A.

As an illustrative example, the trends obtained for the Monte Settepani radar along azimuth 30° and the third elevation index (corresponding to an elevation of 2.1°) are presented for 28 August 2025 at 11:50. As shown in Figure 3.7a, the pre-filtering differential phase shift ($u\phi_{DP}$) exhibits both positive and negative peaks with irregular fluctuations. In contrast, the corrected differential phase shift Φ_{dp} displays a smooth, monotonically increasing trend.

These reconstructed Φ_{dp} values can also be verified using the PPI (Plan Position Indicator) of the differential phase shift. By selecting the correct azimuth and radius, the trend is confirmed, as shown in Figure 3.7b.

The reflectivity shown in the Figure 3.7a along the individual ray and in the Figure 3.7c as a PPI format, is a direct indication of the precipitation along the beam. It therefore represents a further indication of the correctness of the Φ_{dp} trend: at points where there is no precipitation, the differential phase shift function does not increase with range, since no amount of water or precipitation has been recorded at that point in the range. Where reflectivity is measured, however, Φ_{dp} generally shows an increasing trend, with a slope depending on

the signal attenuation amount.

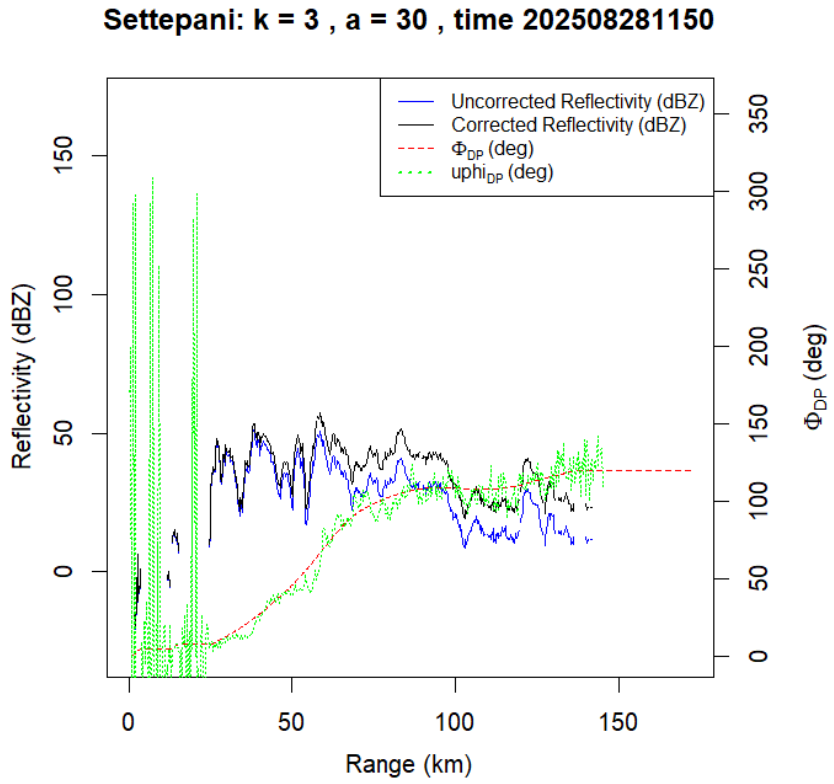

(a) Trends in reflectivity, pre-filtering differential phase shift and reconstructed differential phase shift

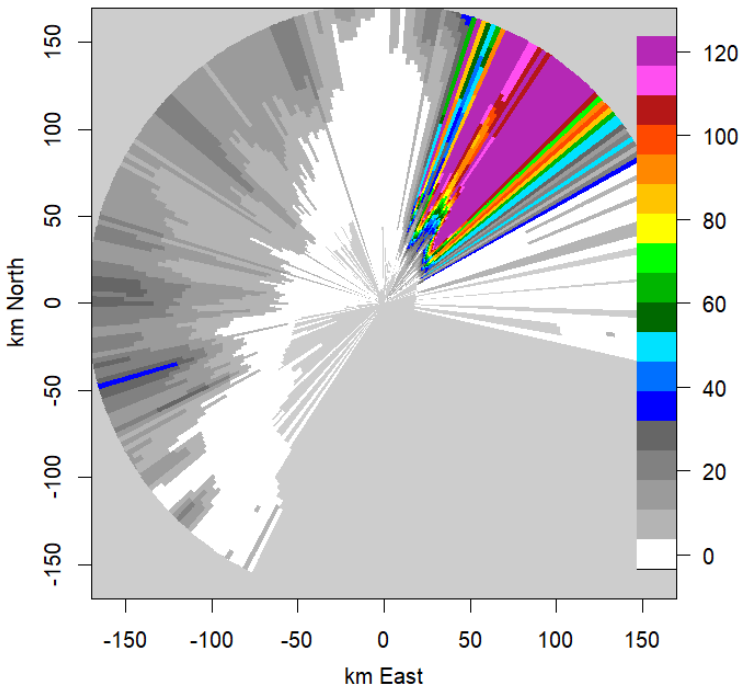

(b) PPI representation of the differential phase shift

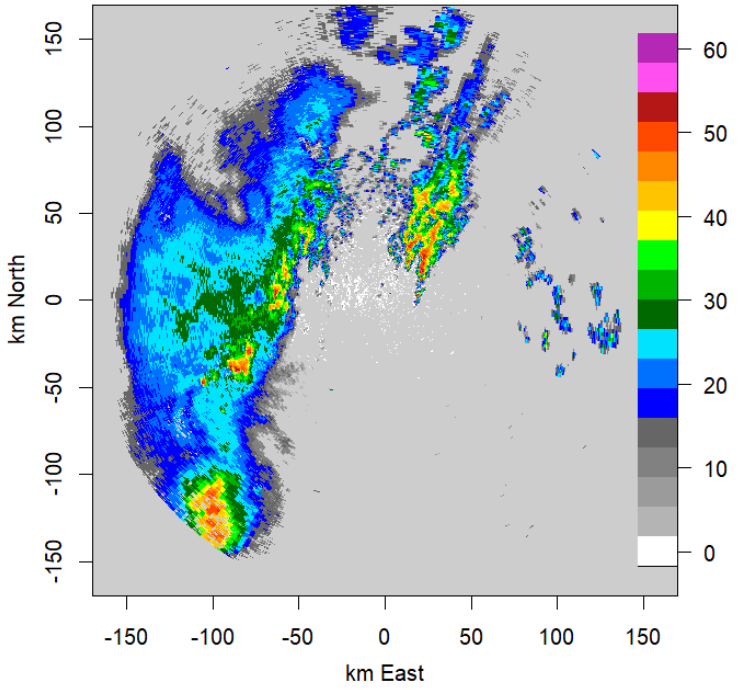

(c) PPI representation of the reflectivity

Figure 3.7: Trends in reflectivity, pre-filtering differential phase shift, and reconstructed differential phase shift measured from the Monte Settepani radar, along the beam with azimuth of 30° and elevation value equal to 2.1° (third elevation index).

3.3.4 Reflectivity correction with a fixed attenuation coefficient

This section will describe the methodology for estimating attenuation coefficients. Fixed values for the attenuation coefficient are available in the literature, as shown in Table 2.3 and are often used in reflectivity correction procedure, avoiding their optimisation for each individual event. As a result, errors may arise in the attenuation estimate for the event in question, creating an overestimate or underestimate in the corrected reflectivities.

Prior to the attenuation coefficient optimisation procedure, reflectivity correction is performed using the classic Φ_{dp} - Method. For each radar and each scan, Equation 2.26 is applied to obtain the corrected reflectivity values. The analysis results will be shown in Chapter 4.

The corrected reflectivity values will be used for comparison with the results obtained at the end of the optimization analyses. In this framework, additional statistical metrics, including standard deviation, are computed for the uncorrected data, the data corrected using a fixed coefficient, and the data corrected using the optimized coefficient, in order to enable a comprehensive comparison of the results.

The standard deviation is expected to decrease, with the largest dispersion observed for the uncorrected data, intermediate values for the fixed-coefficient correction, and the lowest dispersion for the optimized correction.

As an example, the result of the reflectivity correction using a fixed coefficient for two generic radars is shown in Figure 3.8a and 3.8b.

The two density plots confirm what is explained above: the values tend to align along the straight line and their dispersion tends to decrease after the attenuation correction is performed.

However, a residual calibration bias is observed: the two radars systematically measure reflectivities that are offset by a few dB. This is highlighted by the cloud of values that is slightly shifted with respect to the bisector with zero intercept and unit slope. It is therefore considered necessary to apply a specific correction for the calibration bias.

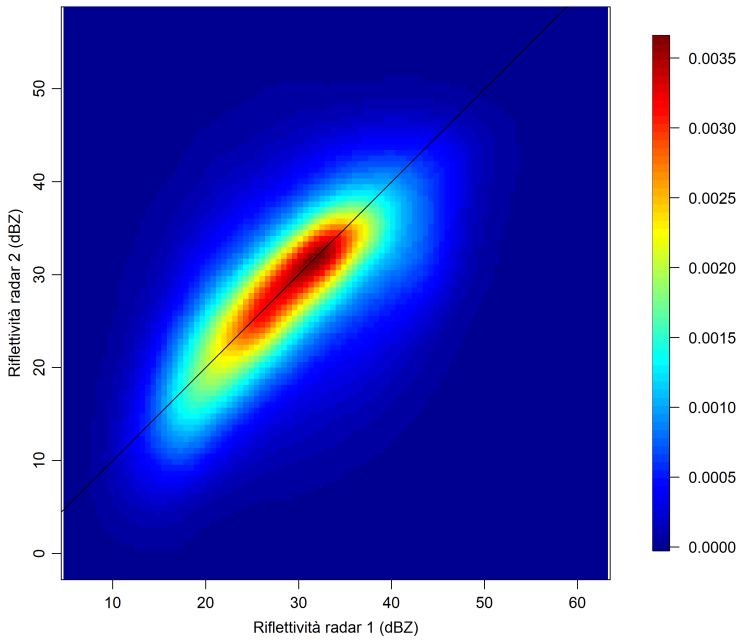

(a) Pre-correction reflectivity values.

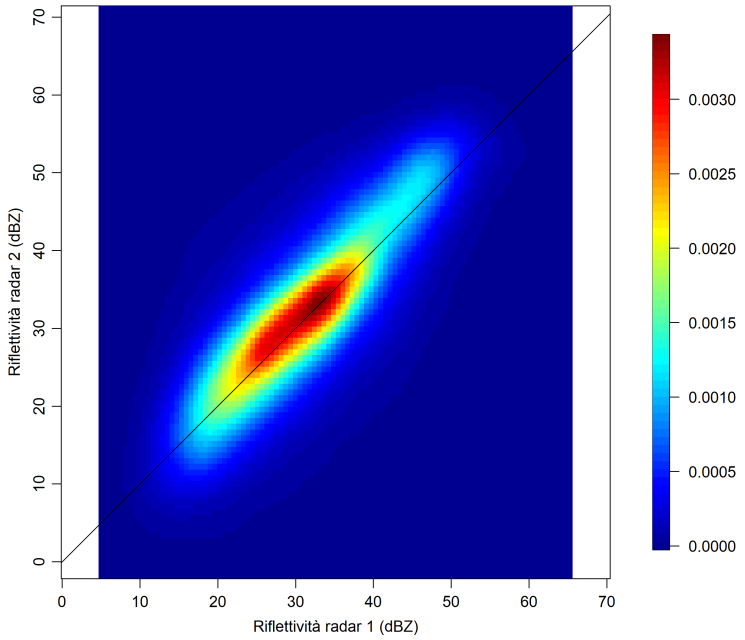

(b) Post-correction reflectivity values (with fixed coefficients).

Figure 3.8: Density plots of reflectivity values for two general radars at their intersection points, before and after correction.

Using the fixed attenuation coefficient and the Φ_{dp}-Method, measured reflectivity values can be corrected for attenuation. However, Equation 2.26 does not account for calibration bias, which must be estimated separately. To do this, a linear regression is applied to the corrected values, forcing the slope to 1 so that

only the intercept, representing the bias, remains unknown. This regression is performed in R using the *linear model* function, which provides estimates of coefficients and related statistics. The intercept can be positive or negative, depending on which radar systematically overestimates reflectivity: if radar 1 is on the x-axis and radar 2 on the y-axis (Figure 3.8b), points above the bisector indicate radar 2 overestimation, while points below indicate radar 1 overestimation.

In a radar network, instruments are generally calibrated to provide consistent measurements, but there are uncertainties that result in a residual bias of a few dB. Even small biases of 3–5 dB correspond to substantial differences in measured reflectivity, and cannot be ignored, as they would lead to errors in the estimation of attenuation coefficients.

3.3.5 New coefficients-based Method

The most important part of the methodology development is related to the optimisation of attenuation coefficients.

The optimised attenuation coefficients can be compared at the end of the analysis with those currently used by Arpa for precipitation estimation (QPE). In particular, it is interesting to note whether they are lower or higher than the latter: if the optimised coefficient is greater than the one used, the drop size distribution (DSD) could be shifted towards smaller drops. Conversely, in the case of a lower optimised coefficient, it could be dominated by large droplets. A second hypothesis concerning the lower optimised coefficient could be precipitation characterised by melting hail, which has a very flattened shape.

These considerations are justified by the fact that the attenuation coefficient is a measure of this phenomenon. According to Equation 2.26, if there is greater attenuation, the alpha coefficient must be greater in order to adequately correct the measured reflectivities.

Attenuation coefficients will be estimated from both radar pairs: the C-band pair (5.6 GHz) yields α_C, while the mixed C–X band pair (5.6 GHz and 9.4 GHz) yields α_C and α_X. Comparing the two pairs allows assessing the correlation between the C-band coefficient derived from the single- and mixed-

frequency analyses.

In addition, different events belonging to different days will be investigated. This will provide a statistical sample of attenuation coefficients for both C-band and X-band radars, which will allow for the analysis of similarities or differences between different daily datasets.

3.3.5.1 The C-band and X-band application

In the general case where the attenuation coefficients for a pair of radars in different bands (C and X) are to be optimised, for their observed reflectivities $Z_{h,C}(V_i)$ and $Z_{h,X}(V_i)$ it is assumed that:

$$Z_{h,C}(V_i) = Z_{h,X}(V_i), \tag{3.11}$$

since the two radars at the intersection points must observe the same meteorological target, and therefore measure the same reflectivity. This assumption holds under Rayleigh scattering conditions. Therefore, non-Rayleigh targets (e.g., hail, which is non-Rayleigh at X-band) must be excluded from the analysis: this condition is enforced operationally by removing overlapping volumes above the melting layer. Below the melting layer, the occurrence of such targets is assumed to be negligible.

However, it has been shown that the two radars, due to attenuation and other phenomena, measure different reflectivity values (Figure 1.4a). Applying the Φ_{dp} - Method equation (Equation 2.26) and substituting into the previous equation (Equation 3.11), the following is obtained:

$$Z'_{h,C}(V_i) + \alpha_C \Phi_{dp,C}(V_i) = Z'_{h,X}(V_i) + \alpha_X \Phi_{dp,X}(V_i), \tag{3.12}$$

where $Z'_{h,C}(V_i)$ and $Z'_{h,X}(V_i)$ are the reflectivities measured by the radars at the C-band and X-band respectively, α_C and α_X are the unknown attenuation coefficients, which will be optimised using a linear regression, and $\Phi_{dp,C}(V_i)$ and $\Phi_{dp,X}(V_i)$ are the differential phase shifts of the C band and X band radars along the two different rays, respectively.

In reality, the calibration bias must be added to this formulation, consequently

the Equation 3.12 becomes:

$$Z'_{h,C}(V_i) + \alpha_C \Phi_{dp,C}(V_i) + bias(C) = Z'_{h,X}(V_i) + \alpha_X \Phi_{dp,X}(V_i) + bias(X). \quad (3.13)$$

The previous equation (3.13) can be rewritten by bringing the calibration bias of the C-band radar to the second term, subtracting it from that of the X-band (thus, de facto, reducing it to a relative calibration), and moving the X-band measured reflectivity to the first term. Consequently, it is rewritten as:

$$Z'_{h,C}(V_i) - Z'_{h,X}(V_i) = \alpha_X \Phi_{dp,X}(V_i) - \alpha_C \Phi_{dp,C}(V_i) + \Delta_{cal}, \quad (3.14)$$

where Δ_{cal} is:

$$\Delta_{cal} = bias(C) - bias(X). \quad (3.15)$$

Rewriting the terms to simplify the equation, they are defined:

$$x = \Phi_{dp,X}, \quad (3.16)$$

$$y = \Phi_{dp,C}, \quad (3.17)$$

$$z = Z'_{h,C}(V_i) - Z'_{h,X}(V_i). \quad (3.18)$$

Finally, the Equation 3.14 is formulated using the previous definitions:

$$z = \Delta_{cal} + \alpha_X x - \alpha_C y. \quad (3.19)$$

In order to optimise the attenuation coefficients, the linear regression tool is used again. In this case, unlike the previous linear regression operation, there are three unknown coefficients of interest (Δ_{cal}, α_X, α_C).
Defining the variables x, y and z as specified above, the linear regression model is set as follows:

$$mod = lm(z \sim x, y) \quad (3.20)$$

where *mod* will contain the coefficients and the related statistical quantities, while the linear model function is read as "*z as a function of x and y*".
The output will return the intercept of the interpolating line and the α_X

and α_C coefficients, namely the partial regression coefficients. This provides the parameters that optimise the interpolation of the measured values and, consequently, that best describe the meteorological event under examination. In order to compare the fixed coefficients used by Arpa with the optimised coefficients obtained, the standard deviation of the values corrected using the optimised coefficients is calculated. In fact, this should be lower than that of the values corrected with a fixed coefficient.

Furthermore, the regression function provides some statistical estimates, which are useful for pre- and post-optimisation comparison. In particular, a statistical summary of the distribution of residuals is highlighted through the median, which indicates how the residuals are distributed, and the first and third quantiles, which together with the minimum and maximum values determine whether or not the distribution of residuals is symmetrical. The ideal condition is a symmetrical distribution, as this means that the regression model is neither underestimating nor overestimating the output coefficients. Under ideal conditions, therefore, we would expect a median close to 0, with the first and third quantile values similar in absolute value, as well as the minimum and maximum values, but with an opposite sign.

The function then lists the statistical quantities related to the estimation of the individual coefficients, describing the estimated standard deviation, the $t - value$ and the $p - value$ for each one. The standard deviation describes the error in the estimation of the coefficients and, as such, the regression result is considered valid when it is low enough, i.e. close to 0. The $t - value$, on the other hand, indicates how large the estimate is relative to the associated uncertainty, so it is preferable to obtain a high value for this parameter (greater than 2 or 3). Finally, the $p - value$ is inversely proportional to the $t - value$, so low values for this parameter indicate that the estimate is to be considered significant. Generally, an estimate is considered significant if the $p - value$ is less than 0.05, very significant if it is less than 0.01, and extremely significant if it is less than 0.001.

In conclusion, the statistical quantities relating to the overall estimate are illustrated, as opposed to the previous ones relating to the estimation of

individuals. Of particular interest are the *Adjusted* R^2 and the $p-value$: the first one represents the coefficient of determination corrected according to the number of variables to be estimated, in this case the alphas. This characteristic makes it particularly suitable for comparing models with different numbers of variables, a situation that arises when adding to the analysis the dataset of the C-band radar pair.

3.3.5.2 The C-band radar pair application

When considering the pair of C-band radars, the procedure and considerations outlined in the previous section remain the same, but the problem is simplified in terms of variables. In fact, when analysing a pair of C-band radars, Equation 3.12 gets simplified because the attenuation coefficient is the same for both instruments. In particular, it becomes:

$$Z'_{h1,C}(V_i) + \alpha_C \Phi_{dp1,C}(V_i) = Z'_{h2,C}(V_i) + \alpha_C \Phi_{dp2,C}(V_i), \tag{3.21}$$

where $Z'_{h1,C}(V_i)$ and $Z'_{h2,C}(V_i)$ are the reflectivities measured by C-band radars 1 and 2 respectively, α_C is the unknown attenuation coefficient, which will be optimised using linear regression, and $\Phi_{dp1,C}(V_i)$ and $\Phi_{dp2,C}(V_i)$ are the differential phase shifts of C-band radars 1 and 2 respectively.
Adding the calibration bias and moving the quantities to the first and second terms, the 3.14 becomes:

$$Z'_{h1,C}(V_i) - Z'_{h2,C}(V_i) = \alpha_C(\Phi_{dp2,C}(V_i) - \Phi_{dp1,C}(V_i)) + \Delta_{cal}. \tag{3.22}$$

At this point, the unknown variables are reduced to two of them: the linear regression will allow to estimate the slope of the regression line, i.e. α_C, and its intercept.
The terms for setting up the linear regression are then redefined, although the same logic explained above applies. In this case, the regression variables are written as follows:

$$x = \Phi_{dp2,C}, \tag{3.23}$$

$$y = \Phi_{dp1,C}, \tag{3.24}$$

$$z = Z'_{h1,C}(V_i) - Z'_{h2,C}(V_i). \tag{3.25}$$

And Equation 3.19 will become:

$$z = \Delta_{cal} + \alpha_C(x - y). \tag{3.26}$$

Consequently, the function for the linear regression is set as:

$$mod = lm(z \sim I(x - y)) \tag{3.27}$$

Unlike the previous application where radars have different frequencies, it is necessary to use the inhibition *I command* so that the regression interprets the difference between x and y as a single variable. In this way, the function will estimate the two unknowns: the intercept Δ_{cal} and the slope α_C.

3.3.5.3 Using the differential phase shift filtering for attenuation coefficient and calibration bias estimate

In conclusion, the last part of the methodology involves estimating the attenuation coefficients α_C and α_X and the calibration biases between the radar pairs by filtering the data with the differential phase shift. This step represents a further verification of the obtained results.
First, the calibration bias is calculated for both pairs, selecting only points characterised by low attenuation. Under low-attenuation conditions, Φ_{dp} assumes negligible values; hence, Equation 3.14 reduces to::

$$Z'_{h,C}(V_i) - Z'_{h,X}(V_i) = \Delta_{cal}. \tag{3.28}$$

While Equation 3.22 becomes:

$$Z'_{h1,C}(V_i) - Z'_{h2,C}(V_i) = \Delta_{cal}. \tag{3.29}$$

It is therefore easy to obtain the calibration bias by simply subtracting the reflectivities of the two radars at the low attenuation intersection points. The

calculated value then becomes a known parameter within Equation 3.14 and Equation 3.22.

This enables the estimation of the attenuation coefficients via linear regression, as previously performed, with the intercept constrained to the calibration bias determined earlier.

Again, the differential phase shift is used to filter the data: contrary to what is done for Δ_{cal}, the high attenuation intersection points are selected. In this framework, the estimation of the coefficients becomes particularly effective. Using the same variables defined in sections 3.3.5.1 and 3.3.5.2, the regression provides the unknown variables, i.e. the attenuation coefficients.

	Bric della Croce	Settepani	Druento
Calibration Bias	5°	5°	8.5°
Attenuation coefficient	20°	20°	34°

Table 3.4: Threshold Φ_{dp} values adopted for the verification step.

The values chosen as thresholds reflect the considerations made in chapter 3.3.2.2. and are shown in Table 3.4.

The selected values are justified by the operating frequencies of the radars. Since the C-band operates at a lower frequency than the X-band, it is less affected by attenuation. Consequently, a lower threshold for the calibration bias was adopted for the C-band compared to the X-band. The same logic applies to the thresholds used for the estimation of the attenuation coefficients. Note that the proportionality factor of 1.7 between the C-band radar and the X-band radar is respected, as already applied in the preliminary filtering.

The outcomes of this verification procedure should be consistent with those from the preceding analysis, thus supporting the reliability of the proposed methodology.

3.3.6 Event selection and data aggregation

The methodology involves analysing radar scans from several days in order to ensure a consistent statistical sample. The procedure explained above is therefore applied to precipitation events that occurred at different days.

The events selected for the development of the methodology must necessarily

be characterised by attenuation. If the signal is not sufficiently attenuated along the path of the radar beam, due to low precipitation for example, the attenuation coefficients cannot be estimated, as the attenuation process cannot be quantified. Accordingly, weakly attenuated events will be analysed as representative cases, and the reasons for their exclusion from the analysis and from the statistical sample of valid events will be discussed.

The correct selection of events, on the other hand, involves the analysis of daily Arpa rainfall data: thanks to this, events are identified according to the highest measurements. Subsequently, the position of the areas of high reflectivity of each event is verified using the mosaics provided by Arpa every 5 minutes, i.e. at each radar scan performed. Particular attention is paid to the areas surrounding Turin and the radars of interest: for the methodology to work, areas of high reflectivity must be observed in the field of view of the radars pairs.

For the analysis of the dataset, multiple temporal aggregations were considered. A daily dataset was retrieved from the Arpa server and subsequently partitioned into time blocks of 12 h, 6 h, 4 h, 2 h, 1 h, and 30 min during the analysis phase. These temporal subdivisions allow the assessment of potential variability in the attenuation coefficients over the course of a precipitation event, as well as the evaluation of their stability within a 24-hour period. The methodological steps previously described in the chapter are therefore applied both to the full 24-hour dataset and to each temporal subset. This approach enables the identification of the most appropriate time interval for the optimisation of the attenuation coefficients.

Chapter 4

The dataset and the analysis results

4.1 Analysis dataset description

This chapter presents the outcomes derived from the methodology described in Chapter 3.
Specifically, it reports the results obtained from the C-band radar pair for the following rainfall events:

- July 25, 2022
- May 1, 2024
- October 3, 2024
- April 16, 2025
- April 17, 2025
- August 28, 2025

Furthermore, the results obtained from the combined C- and X-band radar pair are presented for the following events:

- July 25, 2022
- June 29, 2024

- April 17, 2025
- July 23, 2025
- August 28, 2025

To provide context for the results obtained through the radar processing, a pluviometric characterization of the analysed events is presented based on observational data from the Arpa bulletins.

Table 4.1 summarizes the main pluviometric characteristics of the selected events. For each episode, the maximum accumulated precipitation, intensity classification and expected attenuation level are reported.

Date	Max 12h Acc. (mm)	Max 3h Acc. (mm)	Intensity Class	Expected Attenuation
25 Jul 2022	59.6	59.6	Strong to very strong	High
01 May 2024	97.4	38.2	Strong to very strong	High
29 Jun 2024	194.8	127.2	Strong to very strong	High
03 Oct 2024	75.4	65.2	Strong to very strong	High
16 Apr 2025	253.8	111.4	Very strong	High
17 Apr 2025	176.6	72.8	Very strong	High
23 Jul 2025	53.2	53.0	Strong to very strong	High
28 Aug 2025	218.6	109.4	Very strong	High

Table 4.1: Summary of the main pluviometric characteristics of the selected rainfall events based on Arpa bulletins.

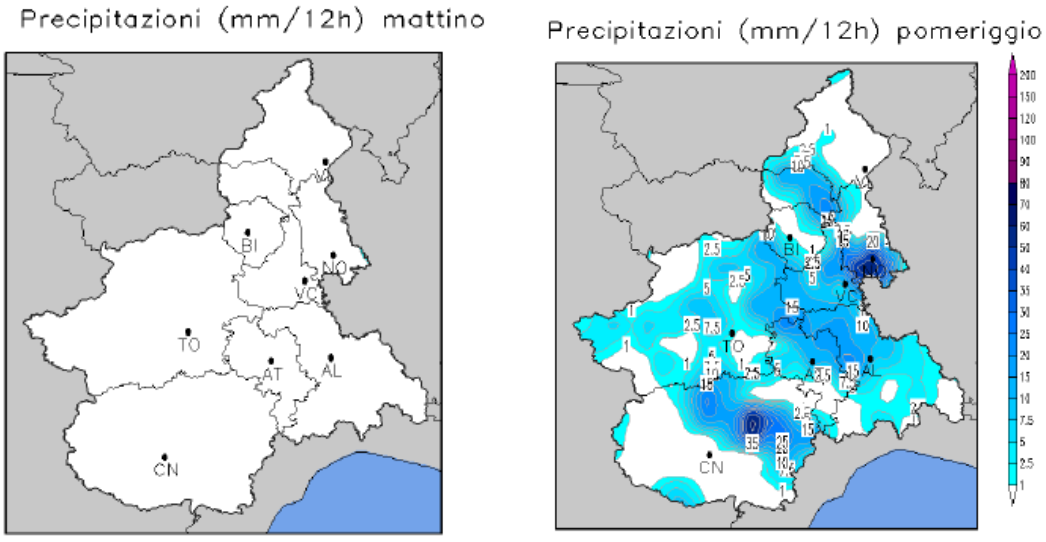

(a) Morning accumulated precipitation. **(b)** Afternoon accumulated precipitation.

Figure 4.1: Accumulated precipitation for the 25 July 2022 event derived from Arpa bulletins.

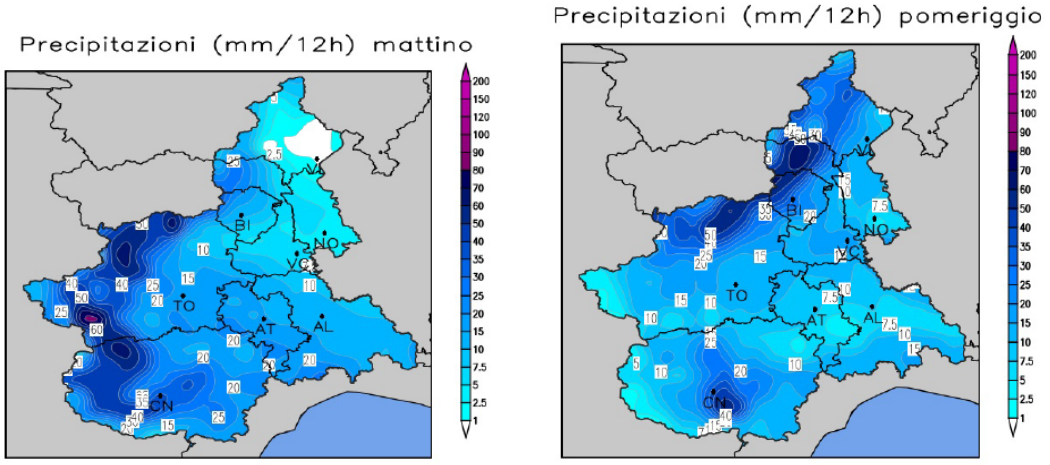

(a) Morning accumulated precipitation. **(b)** Afternoon accumulated precipitation.

Figure 4.2: Accumulated precipitation for the 1 May 2024 event derived from Arpa bulletins.

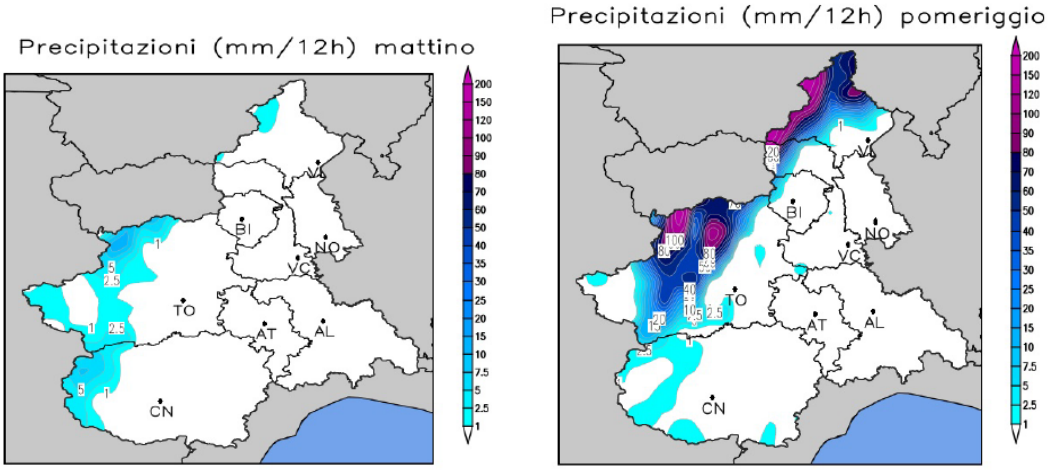

(a) Morning accumulated precipitation. **(b)** Afternoon accumulated precipitation.

Figure 4.3: Accumulated precipitation for the 29 June 2024 event derived from Arpa bulletins.

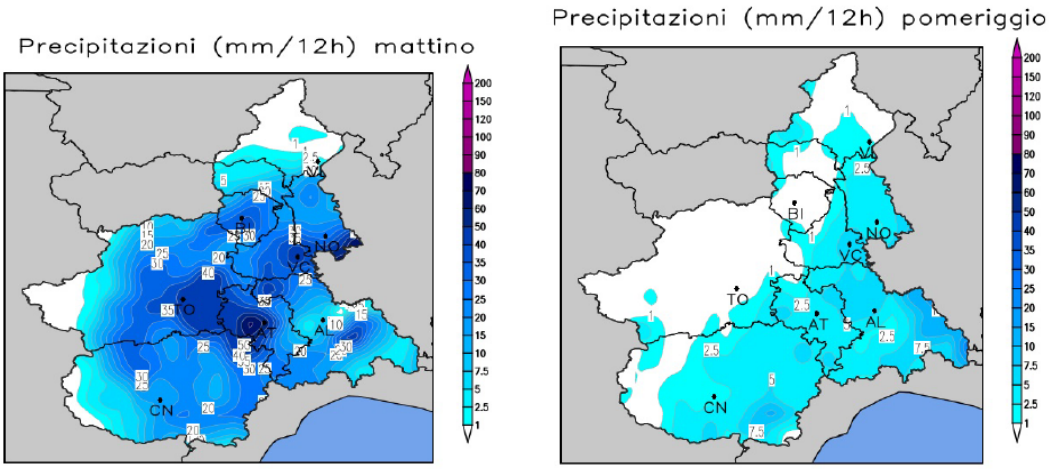

(a) Morning accumulated precipitation. **(b)** Afternoon accumulated precipitation.

Figure 4.4: Accumulated precipitation for the 3 October 2024 event derived from Arpa bulletins.

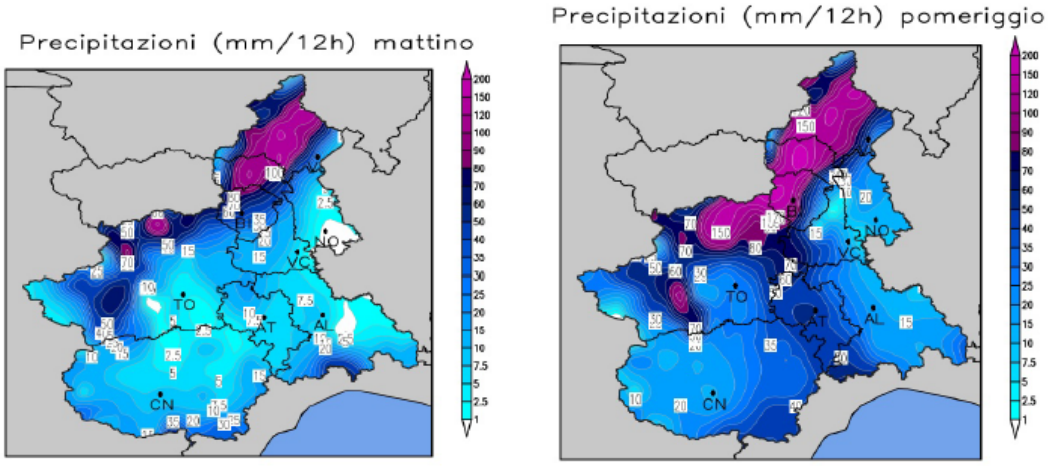

(a) Morning accumulated precipitation. **(b)** Afternoon accumulated precipitation.

Figure 4.5: Accumulated precipitation for the 16 April 2025 event derived from Arpa bulletins.

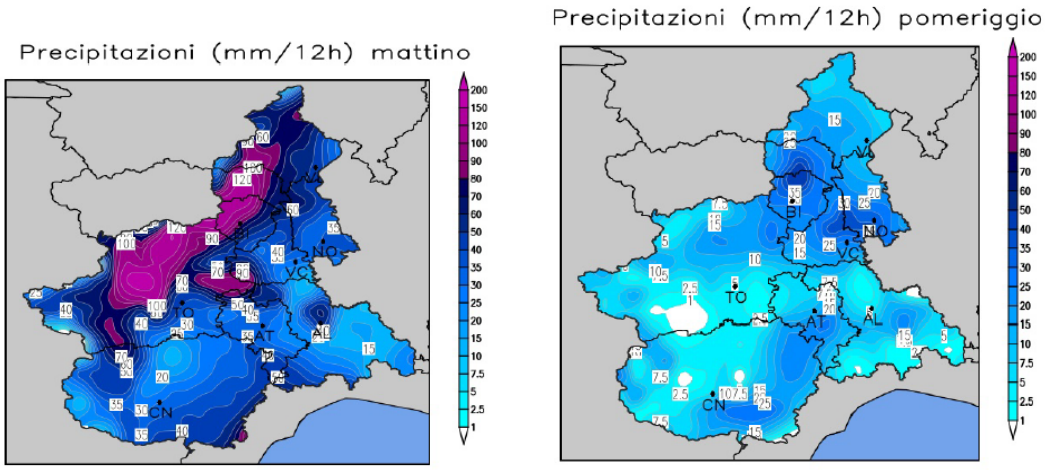

(a) Morning accumulated precipitation. **(b)** Afternoon accumulated precipitation.

Figure 4.6: Accumulated precipitation for the 17 April 2025 event derived from Arpa bulletins.

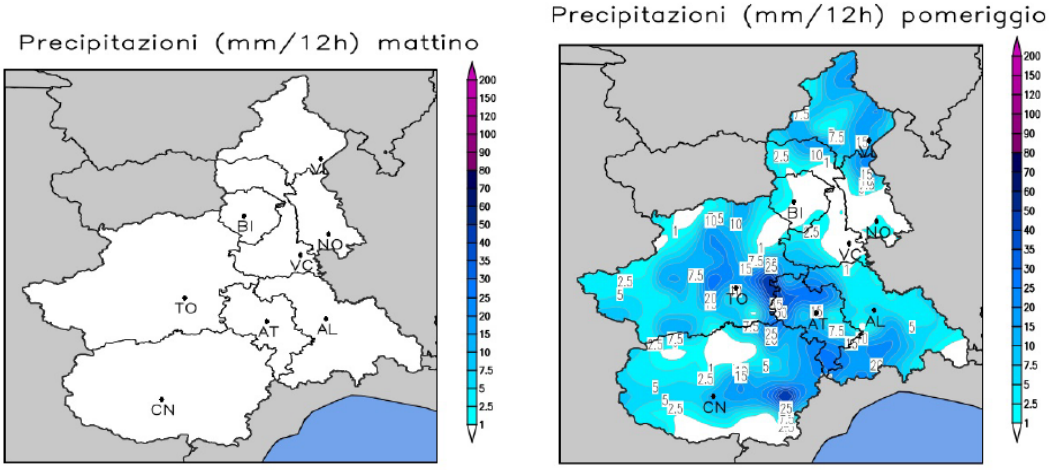

(a) Morning accumulated precipitation. **(b)** Afternoon accumulated precipitation.

Figure 4.7: Accumulated precipitation for the 23 July 2025 event derived from Arpa bulletins.

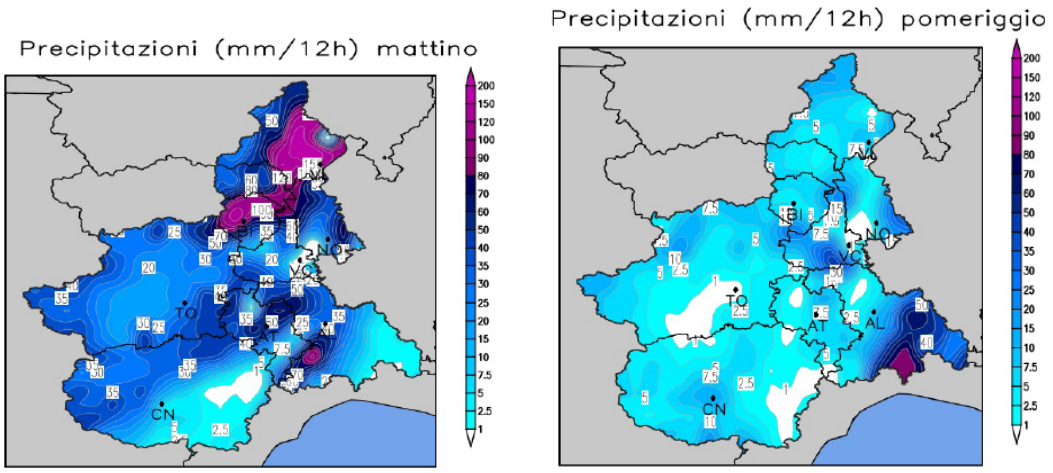

(a) Morning accumulated precipitation. **(b)** Afternoon accumulated precipitation.

Figure 4.8: Accumulated precipitation for the 28 August 2025 event derived from Arpa bulletins.

The selected events exhibit significant variability in terms of spatial distribution, temporal evolution, and intensity of precipitation.

The 25 July 2022 event was mainly concentrated in the afternoon, initially affecting the Alpine and pre-Alpine sectors before moving toward the plains in the evening, with peak accumulations recorded over the Cuneo and Novara areas and a general weakening during late evening.

On 1 May 2024, widespread precipitation occurred, strong to locally very strong over the lower and middle valleys of the Cottian and Graian Alps in the morning, followed by intense showers over the Graian and Pennine Alps in the afternoon, with maximum 24-hour accumulations of about 120–130 mm in the Turin valleys.

The 29 June 2024 event was characterized by thunderstorms developing from late morning over the western Alps and intensifying during the afternoon along the northwestern mountainous and pre-mountain belt, locally accompanied by hail.

On 3 October 2024, moderate and widespread precipitation was observed in the first part of the day, with locally strong showers over the central-eastern plains, followed by a progressive attenuation in the afternoon.

The events of 16 and 17 April 2025 were among the most intense, featuring widespread strong to very strong precipitation with embedded convective ac-

tivity, particularly over the mountainous and foothill sectors of the Turin, Biella, Vercelli, and Verbano areas, leading to significant accumulations before a gradual weakening on the second day.
The 23 July 2025 episode was characterized by afternoon convective development after a dry morning, with scattered thunderstorms over plains and hilly areas and locally intense downpours accompanied by wind gusts and small hail. Finally, on 28 August 2025, widespread morning precipitation affected most sectors, with very strong peaks over the Biella, Verbano, and upper Vercelli areas. Although a partial attenuation occurred later in the day, intense rainfall persisted locally due to a self-regenerating convective system.

4.2 Technical considerations

As described in Chapter 3.3.2.2, geometrical filtering based on distance thresholds is applied in order to maximise the overlapping of the backscattering volumes.
In particular, as regards the Bric della Croce - Monte Settepani pair, a constraint is introduced to exclude intersection points located at excessive distances from the two instruments. The distance between the radars is approximately 95 km; therefore, a maximum allowable range difference of 20 km between the two systems is imposed. Under this condition, Equation 3.5 is reformulated as:

$$|s_r^{(Bric)} - s_r^{(Sett)}| < 20\ km, \tag{4.1}$$

where $s_r^{(Bric)}$ and $s_r^{(Sett)}$ are the distances from the Bric della Croce and Settepani radar, respectively.
This range constraint is further combined with a threshold on the beam height. The freezing level for each event is determined using radiosonde data provided by Arpa from the Cuneo-Levaldigi site, where radiosoundings are conducted at least once per day. For most days, measurements at 00:00 are available, while for some dates additional observations at 12:00 are provided. When available, the midday measurement is selected in order to better represent the rainfall event occurring during the day; otherwise, the 00:00 value is adopted. In any

case, the following Equation is set:

$$H_{beam,th}^{(Bric)} = H_{beam}^{(Bric)} < H_{0\,\circ C}, \tag{4.2}$$

$$H_{beam,th}^{(Sett)} = H_{beam}^{(Sett)} < H_{0\,\circ C}, \tag{4.3}$$

where $H_{beam}^{(Bric)}$ and $H_{beam}^{(Sett)}$ are the beam height for Bric della Croce and Settepani radars and $H_{0\,\circ C}$ is the characteristic freezing level height of each selected date, reported in Table 4.2.

Freezing Level Height		
	00:00	12:00
25 July 2022	4600	4500
01 May 2024	2900	2300
29 June 2024	4200	4000
03 October 2024	3000	-
16 April 2025	-	2500
17 April 2025	2500	2000
23 July 2025	-	3500
28 August 2025	4000	4000

Table 4.2: Freezing Level Height (m) for each selected event.

The overall geometric filtering procedure therefore integrates both the distance-based constraint and the beam-height limitation. Furthermore, an additional filtering criterion based on the visibility maps of each radar is introduced, taking into account their specific visibility characteristics, as illustrated in Figures 3.6a and 3.6b.

Different considerations apply to the Bric della Croce-Druento radar pair. In this case as well, a range constraint is imposed; however, due to the relatively short separation distance of approximately 15 km between the two instruments, the maximum distance criterion is replaced by a minimum distance requirement. Specifically, a minimum distance of 5 km from each radar is imposed. Consequently, Equations 3.6 and 3.7 are reformulated as follows:

$$|s_r^{(Bric)}| > 5\ km, \tag{4.4}$$

$$|s_r^{(Druento)}| > 5\ km, \tag{4.5}$$

where $s_r^{(Bric)}$ and $s_r^{(Druento)}$ are the distances from the Bric della Croce and

Druento radar, respectively.

Similarly to the previous radar pair, a threshold on the radar beam height is also imposed for the Bric della Croce–Druento configuration:

$$H_{beam,th}^{(Bric)} = H_{beam}^{(Bric)} < H_{0\,\circ C}, \tag{4.6}$$

$$H_{beam,th}^{(Druento)} = H_{beam}^{(Druento)} < H_{0\,\circ C}, \tag{4.7}$$

where $H_{beam}^{(Bric)}$ and $H_{beam}^{(Druento)}$ are the beam height for Bric and Druento radars and the values for the freezing level coincide with those listed in Table 4.2.

Finally, in addition to the geometric condition, the visibility condition is applied, according to the maps in Figures 3.6a and 3.6c.

For illustrative purposes, the points retained after applying the above-described filters are presented in Figure 4.9, referring to the event of 28 August 2025. The corresponding accumulated precipitation map is displayed in the background.

Figure 4.9 presents the intersection points density map, enhanced with contour lines connecting locations characterized by equal point density.

In particular, the absence of points towards the western sector reflects the limited radar visibility caused by the Alpine mountain range. Consequently, the point cloud extends predominantly eastward, in the direction of the Po Valley, where no major orographic obstructions are present.

It can be observed from the spatial distribution of the intersection volumes that the overlapping region for the Bric della Croce-Druento pair is more limited than that of the Bric della Croce–Settepani pair. This is due to the shorter maximum operational range of one radar in the former pair, i.e. the Druento one, consistent with the range characteristics reported in Table 3.2. Finally, the highest concentration of intersection points is located along the baseline connecting the two radars, which is consistent with their relative geometry and the underlying radar measurement principles.

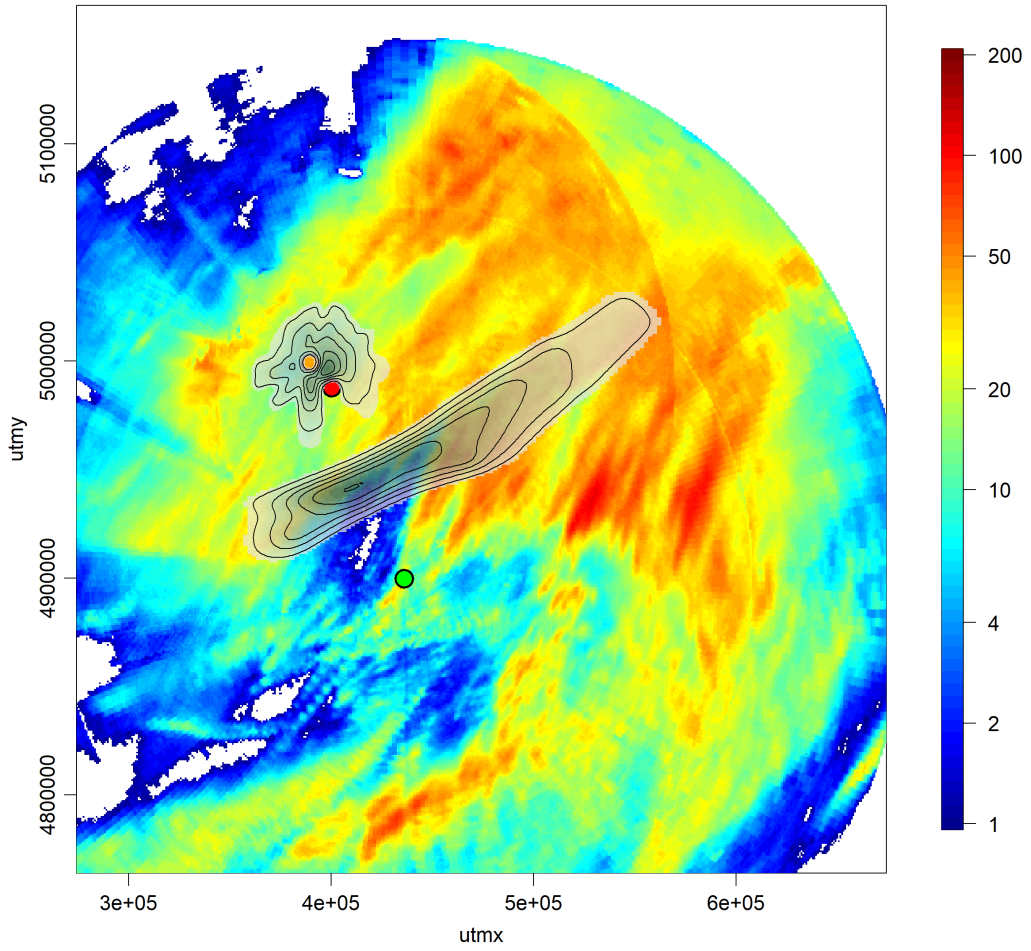

Figure 4.9: Density plot for the intersection points selected for the event of 28 August 2025, with its cumulated precipitation map. The density is represented by a grey colour scale: darker areas are linked to a higher density, while lighter sites are linked to a smaller density of intersection points. The three circles indicate the locations of the radars, with orange representing Druento, red representing Bric della Croce, and green representing Monte Settepani.

4.3 Dataset results

The results are presented in tabular form in the following section. The tables report the following quantities:

- Valid Points: number of valid points after applying all filters, i.e., the number of points that will be analysed to estimate the attenuation coefficient;
- $\alpha_{C,Optimized}$: attenuation coefficient for C-band radar obtained through the optimization methodology proposed in this thesis project;
- $\alpha_{X,Optimized}$: attenuation coefficient for X-band radar obtained through the optimization methodology proposed in this thesis project;
- $StDev_{\text{Uncorrected}}$: standard deviation calculated from uncorrected reflectivity data, i.e. on the reflectivity data measured by radar;
- $StDev_{\text{Corrected}}$: standard deviation calculated from reflectivity data corrected using the Φ_{dp} method with the fixed Arpa coefficient (see Table 2.3);
- $StDev_{\text{Optimized}}$: standard deviation calculated from reflectivity data optimized using the Φ_{dp} method with the optimized coefficient (i.e. $\alpha_{\text{C,Optimized}}$ and $\alpha_{X,Optimized}$);
- $Bias_{\text{Corrected}}$: calibration bias or intercept of the regression line computed on the corrected reflectivity data;
- $Bias_{\text{Optimized}}$: calibration bias or intercept of the regression line computed on the optimized reflectivity data;
- $Bias_{\Phi_{dp}\,\text{low}}$: calibration bias or intercept of the regression line computed on reflectivity data filtered with a low Φ_{dp};
- $\alpha_{C,\Phi_{dp}\,\text{high}}$: attenuation coefficient for C-band radar calculated from reflectivity data filtered with a high Φ_{dp};

- $\alpha_{X,\Phi_{dp}\,\text{high}}$: attenuation coefficient for X-band radar calculated from reflectivity data filtered with a high Φ_{dp}.

4.3.1 Time aggregations considerations

For a representative case study (28 August 2025) and focusing on the C-band radar pair, several temporal aggregation strategies were investigated.
Initially, the event was analysed by dividing it into two 12-hour intervals. The corresponding results are reported in Table 4.3.

Parameter	**1st block**	**2nd block**
Valid Points	211330	319761
$\alpha_{\text{C,Optimized}}$	0.07	0.07
$\text{StDev}_{\text{Uncorrected}}$	8.93	5.77
$\text{StDev}_{\text{Corrected}}$	7.37	5.13
$\text{StDev}_{\text{Optimized}}$	6.95	4.86
$\text{Bias}_{\text{Corrected}}$	1.50	0.52
$\text{Bias}_{\text{Optimized}}$	0.91	-0.30
$\text{Bias}_{\Phi_{dp}\,\text{low}}$	-0.42	0.65
$\alpha_{C,\Phi_{dp}\,\text{high}}$	0.07	0.07

Table 4.3: Statistical metrics for the 12-hour aggregation of 28 August 2025 case study for the Bric della Croce and Settepani radars. The first block refers to 00:00-12:00 interval, while the second to 12:00-24:00 interval.

The 12-hour aggregation yields satisfactory results for the attenuation coefficient, with decreasing values of standard deviation from uncorrected to optimized data. Nevertheless, discrepancies arise in the estimation of the calibration bias, as the verification procedure, i.e. the $\text{Bias}_{\Phi_{dp}\,\text{low}}$, does not fully confirm the obtained results.
To better understand these inconsistencies, additional temporal aggregations were examined by progressively reducing the duration of the time blocks, thereby decreasing the number of available reflectivity samples. The results for the 6-hour and 4-hour aggregations are fully reported in Tables 4.4 and 4.5, respectively, while the outcomes for the shorter intervals (2 hours, 1 hour, and 30 minutes) are provided in Appendix B.

Clearly, as the number of valid points decreases, the methodology becomes less effective. Since the approach relies on linear regression, an insufficient number of data points undermines the robustness of the estimates. This trend

Parameter	**1st block**	**2nd block**	**3rd block**	**4th block**
Valid Points	54425	156905	92233	227528
$\alpha_{\text{C,Optimized}}$	0.08	0.07	0.07	0.05
$\text{StDev}_{\text{Uncorrected}}$	6.06	9.72	6.90	5.02
$\text{StDev}_{\text{Corrected}}$	5.53	7.90	5.20	5.04
$\text{StDev}_{\text{Optimized}}$	5.52	7.37	4.80	4.87
$\text{Bias}_{\text{Corrected}}$	1.29	1.57	1.55	0.11
$\text{Bias}_{\text{Optimized}}$	1.15	0.89	-0.02	-0.50
$\text{Bias}_{\Phi_{dp}\,\text{low}}$	0.02	-1.42	0.71	0.56
$\alpha_{C,\Phi_{dp}\,\text{high}}$	0.08	0.06	0.07	0.06

Table 4.4: Statistical metrics for the 6-hour aggregation of 28 August 2025 case study for the Bric della Croce and Settepani radars. The blocks refer to the following intervals: 00:00-06:00, 06:00-12:00, 12:00-18:00, 18:00-24:00.

Parameter	**1st block**	**2nd block**	**3rd block**	**4th block**	**5th block**	**6th block**
Valid Points	19951	83118	77110	123384	176	226725
$\alpha_{\text{C,Optimized}}$	-0.004	0.09	0.06	0.07	0.1	0.05
$\text{StDev}_{\text{Uncorrected}}$	4.71	8.16	8.97	7.50	4.67	5.02
$\text{StDev}_{\text{Corrected}}$	4.86	6.62	8.51	5.72	4.65	5.04
$\text{StDev}_{\text{Optimized}}$	4.71	5.67	7.95	5.15	4.65	4.87
$\text{Bias}_{\text{Corrected}}$	1.92	0.14	1.93	2.11	3.50	0.11
$\text{Bias}_{\text{Optimized}}$	-0.10	0.55	0.36	0.02	3.68	-0.49
$\text{Bias}_{\Phi_{dp}\,\text{low}}$	0.001	-0.34	-1.94	0.63	-0.17	0.55
$\alpha_{C,\Phi_{dp}\,\text{high}}$	0.01	0.09	0.04	0.07	-0.08	0.06

Table 4.5: Statistical metrics for the 4-hour aggregation of 28 August 2025 case study for the Bric della Croce and Settepani radars. The blocks refer to the following intervals: 00:00-04:00, 04:00-08:00, 08:00-12:00, 12:00-16:00, 16:00-20:00, 20:00-24:00.

is already evident in the verification values of the 12-hour aggregation (Table 4.3).

A closer inspection shows that the 6-hour aggregation still produces attenuation coefficients within the expected range of variability. However, discrepancies remains between the calibration biases estimated through the optimization methodology and the $\text{Bias}_{\Phi_{dp}\,\text{low}}$.

A more critical situation arises in the 4-hour aggregation (Table 4.5), where a negative attenuation coefficient, clearly non physical, appears for the first time block of the day. $\text{Bias}_{\Phi_{dp}\,\text{low}}$ and $\alpha_{C,\Phi_{dp}\,\text{high}}$ are also affected by the reduced sample size: an additional negative coefficient is observed, and the values begin to diverge from the regression methodology estimated ones.

The results reported in Table B.1, and even more clearly in Tables B.2 and B.3, further confirm this tendency. Extremely short time aggregations prove to be

unsuitable for a reliable estimation of the attenuation coefficients.
In summary, as the duration of the temporal blocks decreases, the following effects are observed:

- Attenuation coefficients that fall outside the range of variability
- Verifications results calculated through low and high Φ_{dp} respectively for calibration bias and attenuation coefficient, inconsistent with the estimated values through regression analysis.

For these reasons, the most appropriate temporal aggregation for applying the proposed methodology is considered to be the full 24-hour period. This choice ensures a sufficiently large sample size, thereby enhancing the stability and reliability of the linear regression. Shorter aggregations may still be appropriate in cases of events characterized by particularly strong attenuation, but they are generally less robust.

4.4 Results discussion

The results of the proposed methodology are presented in Tables 4.6 and 4.7, referring to the Bric della Croce–Monte Settepani radar pair and the Bric della Croce–Druento radar pair, respectively.

Parameter	**25/07/22**	**01/05/24**	**03/10/24**	**16/04/25**	**17/04/25**	**28/08/25**
Valid Points	124679	94749	219749	91820	213582	530207
$\alpha_{\text{C,Optimized}}$	0.15	0.06	0.05	0.08	0.10	0.07
$\text{StDev}_{\text{Uncorrected}}$	9.50	4.45	5.24	5.00	5.10	7.24
$\text{StDev}_{\text{Corrected}}$	6.37	4.40	5.28	4.80	4.68	6.14
$\text{StDev}_{\text{Optimized}}$	5.77	4.35	5.10	4.78	4.67	5.81
$\text{Bias}_{\text{Corrected}}$	-0.55	1.36	-0.44	-1.05	-2.63	0.91
$\text{Bias}_{\text{Optimized}}$	-0.90	0.90	-0.23	-1.41	-2.63	0.22
$\text{Bias}_{\Phi_{dp}\,\text{low}}$	1.06	-0.32	0.55	-1.8	-1.76	0.33
$\alpha_{C,\Phi_{dp}\,\text{high}}$	0.15	0.04	0.04	0.07	0.10	0.07

Table 4.6: Comparison of statistical metrics for the C-band (Bric della Croce) and C-band (Monte Settepani) radars across different events.

The analysis of Table 4.6 for the Bric della Croce–Settepani radar pair provides a representative sample of optimized attenuation coefficients, $\alpha_{C,\text{Optimized}}$. The estimated values range between 0.05 dB/deg and 0.15 dB/deg. The associated standard deviation generally supports these results, showing a decreasing

Parameter	**25/07/22**	**29/06/24**	**17/04/25**	**23/07/25**	**28/08/25**
Valid Points	37839	21491	69689	51739	141420
$\alpha_{\text{C,Optimized}}$	0.13	0.06	0.05	0.1	0.06
$\alpha_{\text{X,Optimized}}$	0.34	0.27	0.22	0.32	0.26
$\text{StDev}_{\text{Uncorrected}}$	13.28	12.10	6.31	12.70	7.59
$\text{StDev}_{\text{Corrected}}$	10.24	10.12	5.83	8.50	6.53
$\text{StDev}_{\text{Optimized}}$	10.21	9.99	5.57	8.40	6.39
$\text{Bias}_{\text{Corrected}}$	2.69	-4.38	-4.31	-1.64	-4.08
$\text{Bias}_{\text{Optimized}}$	1.70	-5.85	-5.86	-2.90	-4.90
$\text{Bias}_{\Phi_{dp}\,\text{low}}$	4.36	-3.68	-5.37	-2.09	-3.34
$\alpha_{C,\Phi_{dp}\,\text{high}}$	0.13	0.11	0.09	0.1	0.05
$\alpha_{X,\Phi_{dp}\,\text{high}}$	0.38	0.35	0.27	0.32	0.28

Table 4.7: Comparison of statistical metrics for the C-band (Bric della Croce) and X-band (Druento) radars across different events.

trend after optimization.

A meaningful insight is provided by the high Φ_{dp}-filtered attenuation coefficients, which closely match, or in some cases coincide with, the values estimated through the proposed methodology.

Turning to Table 4.7, which reports results for the combined C- and X-band radar pair, the optimized attenuation coefficients vary between 0.05 dB/deg and 0.13 dB/deg for the C-band and between 0.22 dB/deg and 0.34 dB/deg for the X-band. These estimates are generally confirmed by the verification procedure. An exception is represented by the 29/06/24 event, for which greater uncertainty is observed. This is likely attributable to the limited number of valid points available, which increases the instability of the linear regression used in the estimation process.

Finally, each attenuation estimate was assessed using linear regression statistics, as described in Section 3.3.5.1. As an illustrative example, the regression statistics for the 28 August 2025 event, derived from both radar pairs, are presented.

As reported in Table 4.8, both the statistics related to the individual regressions and those referring to the overall estimates indicate a satisfactory level of robustness. In particular, the standard error assumes values close to zero, suggesting limited dispersion around the regression line. Moreover, the p-values fall within the range defined in Section 3.3.5.1 as extremely significant, further confirming the low level of uncertainty associated with the attenuation

Coefficients	**Estimate**	**Std. Error**	**t value**	**Pr(>|t|)**
(Intercept)	0.22	0.0085	25.6	$< 2 \times 10^{-16}$ ***
I(X2 - X1)	0.07	0.0001	540.5	$< 2 \times 10^{-16}$ ***
Residuals				
Min: -41.119	1Q: -3.197	Median: 0.008	3Q: 3.146	Max: 36.448
Residual standard error: 5.81 on 530205 degrees of freedom				
Multiple R-squared: 0.3553, Adjusted R-squared: 0.3553				
F-statistic: 2.922×10^5 on 1 and 530205 DF, p-value: $< 2.2 \times 10^{-16}$				

Table 4.8: Linear Regression results for 28 August 2025 case study and Bric della Croce - Monte Settepani radars.

Coefficients	**Estimate**	**Std. Error**	**t value**	**Pr(>|t|)**
(Intercept)	4.902495	0.037994	129.03	$< 2 \times 10^{-16}$ ***
X2	0.254824	0.001064	239.41	$< 2 \times 10^{-16}$ ***
X1	0.057587	0.001337	43.08	$< 2 \times 10^{-16}$ ***
Residuals				
Min: -38.594	1Q: -3.668	Median: -0.125	3Q: 3.451	Max: 38.890
Residual standard error: 6.39 on 141417 degrees of freedom				
Multiple R-squared: 0.2916, Adjusted R-squared: 0.2916				
F-statistic: 2.91×10^4 on 2 and 141417 DF, p-value: $< 2.2 \times 10^{-16}$				

Table 4.9: Linear Regression results for 28 August 2025 case study and Bric della Croce - Druento radars.

coefficients estimated through the proposed methodology. Special attention should be given to the *adjusted R squared value*, which is especially meaningful when comparing regression models characterized by a different number of partial regression coefficients. Values tending toward zero are consistent with the considerations discussed above and support the reliability of the model formulation.

The same observations apply to the results presented in Table 4.9. Furthermore, the regression statistics computed for the remaining events show comparable behaviour.

Despite variations in the sample size across events, the methodology consistently demonstrates stability and applicability, confirming its robustness under different conditions.

4.4.1 Standard Deviation trend based on attenuation coefficient variability

The proposed methodology is based on a linear regression approach aimed at minimizing the mean square error (MSE) between the reflectivity measurements under analysis. The regression identifies the partial coefficients that best fit the relationship between the variables, ensuring that the difference between the corrected reflectivities is minimized in a least-squares sense.

At first glance, the reduction in the standard deviation observed when comparing reflectivities corrected with a fixed attenuation coefficient and those corrected with the optimized coefficient may appear limited. This could suggest that the improvement introduced by the optimization is not particularly significant. For this reason, a sensitivity analysis was performed by evaluating the variation of the standard deviation as a function of α. The objective was to verify that the standard deviation follows a curve characterized by a clear and physically meaningful minimum, rather than a nearly flat or fluctuating behaviour with non-significant local minima. The methodology can be considered robust only if a well-defined minimum exists, ensuring that the regression process is effectively minimizing a meaningful objective function. The analysis and the corresponding graphical representation are shown for the 25 July 2022 event, which is taken as a representative case study.

As shown in Panel 4.10, although the variations in the standard deviation appear relatively small, they correspond to significant changes in the attenuation coefficient α. This behaviour indicates that the minimization procedure is operating as intended. Importantly, during the regression process, the reflectivity values along one axis are not held fixed while adjusting only the other dataset. Instead, both reflectivity fields are simultaneously modified through the attenuation correction term. Consequently, variations in α tend to partially compensate between the two datasets, which explains why the observed changes in the standard deviation are relatively modest.

Therefore, even small variations in the standard deviation correspond to meaningful changes in the attenuation parameter. The fact that the standard

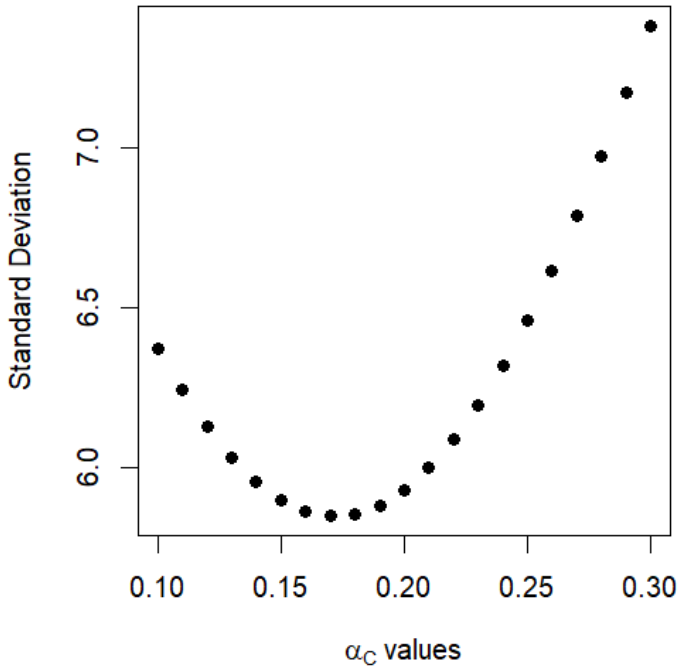

(a) Standard deviation variability for C-band radars.

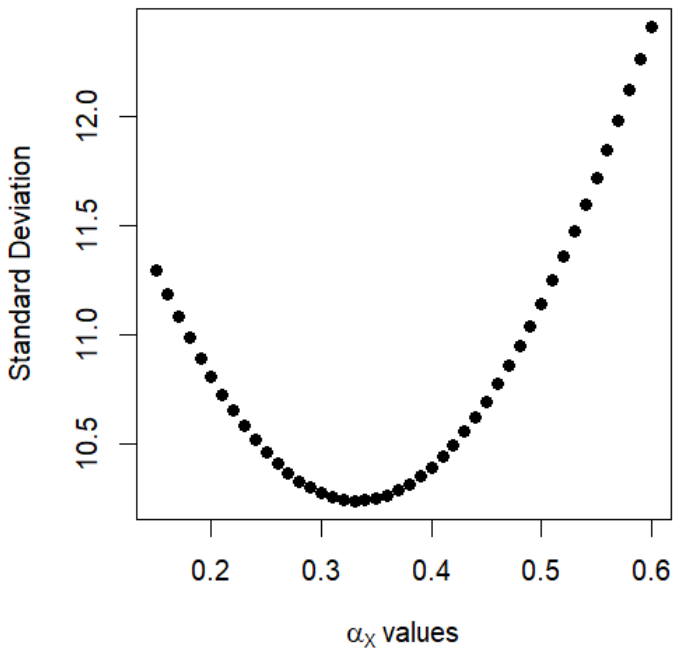

(b) Standard deviation variability for X-band radars.

Figure 4.10: Standard deviation variability on a typical range of α_C and α_X values (in dB/deg), based on the event of 25 July 2022.

deviation curve exhibits a single well-defined minimum, without oscillations or secondary minima within the explored interval, confirms that the minimization process is stable and physically consistent. This behaviour demonstrates that the methodology is robust: the objective function is smooth and effectively convex in the considered range, leading to a unique and well-defined optimal solution for α_C and α_X.

4.4.2 Differential phase shift - based considerations

To better interpret the attenuation coefficients estimated for each event, and to clarify why different datasets were selected for the two radar pairs, it is necessary to analyse the behaviour of the differential phase shift (Φ_{dp}) and, consequently, the overall attenuation associated with each event. For this purpose, two histograms will be produced for each case study showing the Φ_{dp} values measured by both radars of the pair. Negative values are also included, although they are not considered in the analysis since they have no physical meaning. Two additional histograms will represent the attenuation estimates.

The event of 25 July 2022 can be regarded as representative of events suitable for both radar pairs. Panels 4.11 and 4.12 display, respectively, the differential phase shift and attenuation estimate histograms, together with the reflectivity density plots.

From Panel 4.11, differential phase shift values reach approximately 200° for Bric della Croce and 150° for Monte Settepani. Maximum attenuation values of about 17 dB for Bric della Croce and 20 dB for Monte Settepani are observed. The effectiveness of the correction is also confirmed by the density plots in Panel 4.12, where corrected and optimized reflectivity values tend to align along the bisector, indicating improved agreement between the two radar measurements. When comparing these findings with those shown in Panel 4.13 for the Bric della Croce–Druento pair, the Druento radar exhibits stronger attenuation effects, consistent with its higher operating frequency (X-band). This confirms that the event is also suitable for estimating the attenuation coefficient for the second radar pair.

Overall, given the significant differential phase shift and attenuation values

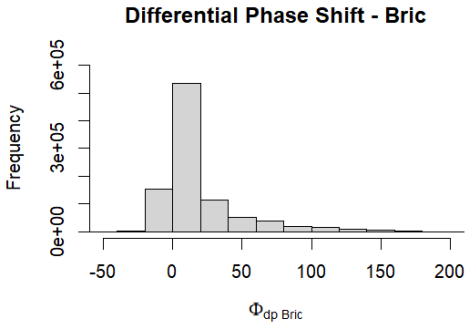

(a) Bric della Croce differential phase shift distribution through histogram, for the 25 July 2022 event and Bric della Croce - Monte Settepani radar pair

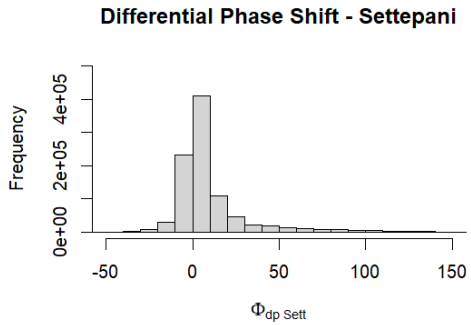

(b) Monte Settepani differential phase shift distribution through histogram, for the 25 July 2022 event and Bric della Croce - Monte Settepani radar pair

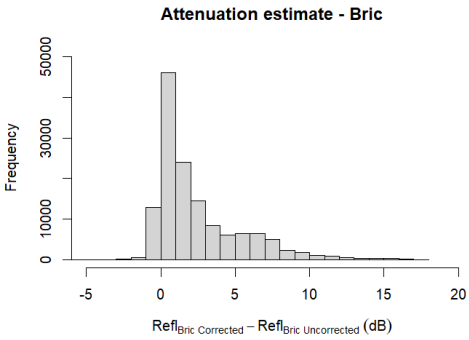

(c) Bric della Croce attenuation distribution through histogram, for the 25 July 2022 event and Bric della Croce - Monte Settepani radar pair.

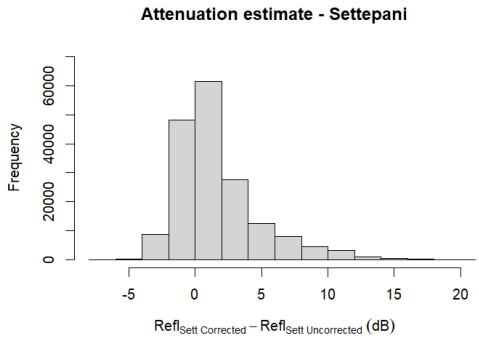

(d) Monte Settepani attenuation distribution through histogram, for the 25 July 2022 event and Bric della Croce - Monte Settepani radar pair

Figure 4.11: Histograms for differential phase shift and attenuation representations for 25 July 2022 and Bric della Croce - Monte Settepani radar pair.

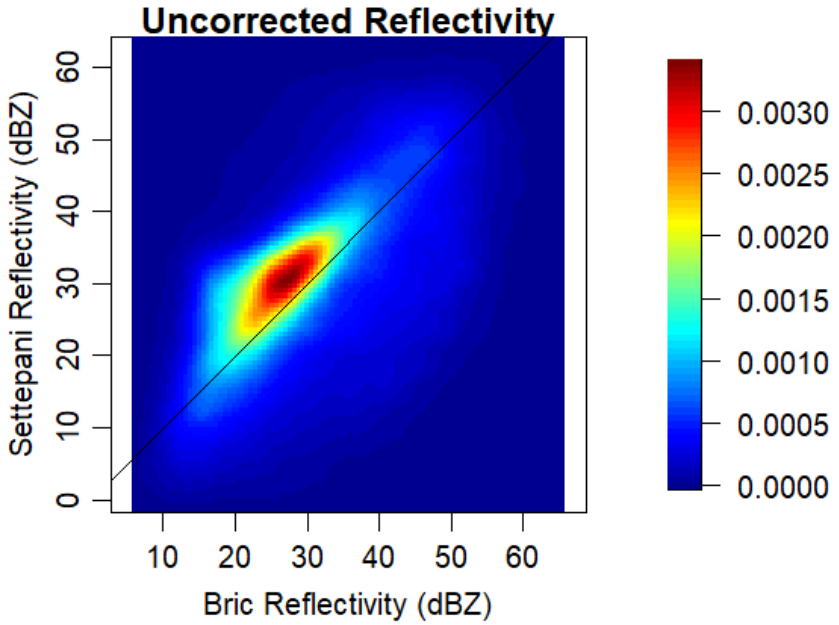

(a) Density plot for uncorrected reflectivity values, for the 25 July 2022 event and Bric della Croce - Monte Settepani radar pair.

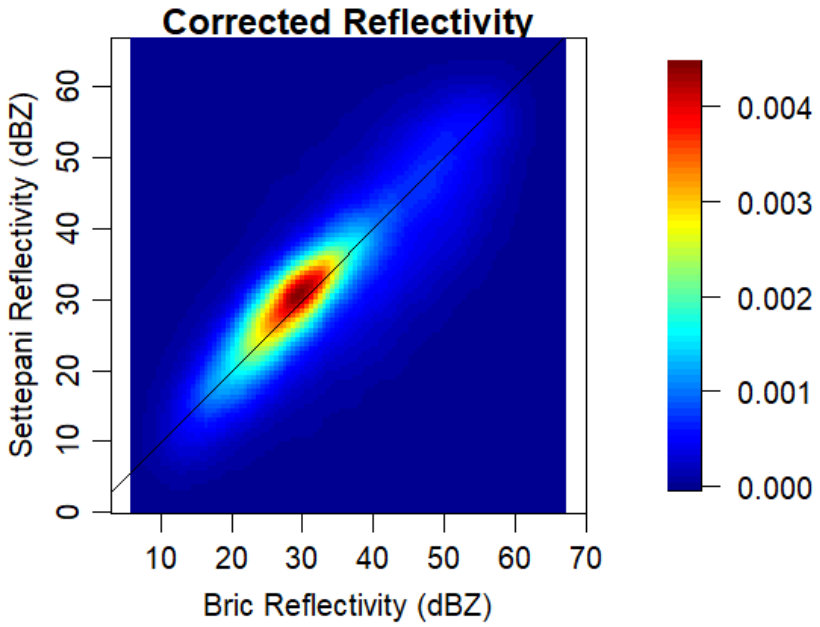

(b) Density plot for corrected reflectivity values (with the fixed coefficient), for the 25 July 2022 event and Bric della Croce - Monte Settepani radar pair.

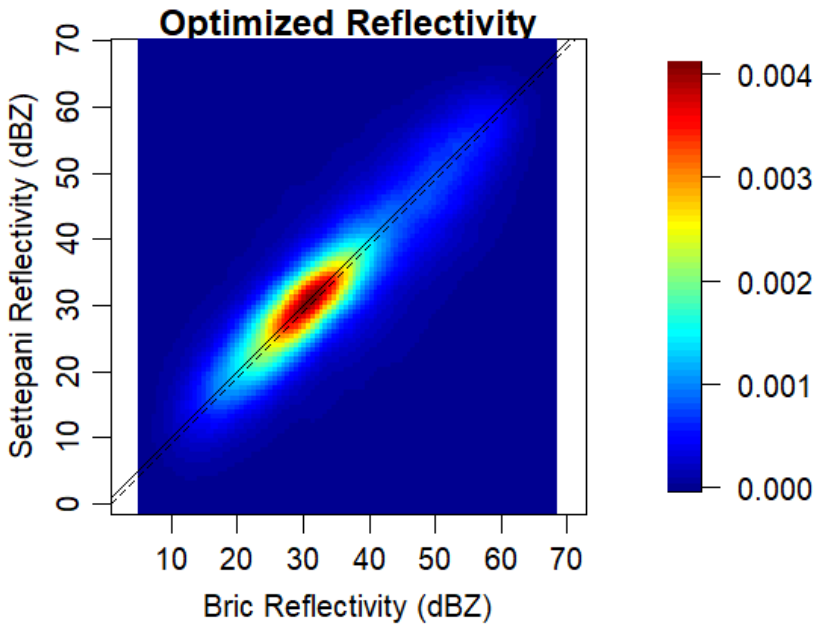

(c) Density plot for optimized reflectivity values, for the 25 July 2022 event and Bric della Croce - Monte Settepani radar pair. The dashed line represents the interpolating line obtained after applying the optimized calibration bias, with a unit slope (equal to 1) and an intercept corresponding to the estimated calibration bias.

Figure 4.12: Density plots of uncorrected, corrected and optimized reflectivity values for 25 July 2022 and Bric della Croce - Monte Settepani radar pair.

observed for both radar configurations, the 25 July 2022 event is considered valid for attenuation coefficient estimation across all considered radars.

In contrast, the event of 16 April 2025 was analysed only for the C-band radar pair. This case is representative in explaining why certain events were selected exclusively for the C-band pair and not for the C–X combination. The histograms (Panel 4.15) indicate more limited attenuation compared to the previously discussed case, a feature that is also reflected in the similarity of the density plots (Panel 4.16). Nevertheless, the differential phase shift values remain sufficiently significant to ensure the applicability of the method to the two C-band radars, which are inherently less affected by attenuation than the X-band radar.

A markedly different situation emerges when examining the parameters for the Bric della Croce–Druento pair (Panels 4.17 and 4.18). In this case, the differential phase shift values are more indicative of a noise-affected signal, with negative values and maxima of approximately 20 for Bric and 40 for Druento. The attenuation estimates and corresponding density plots confirm

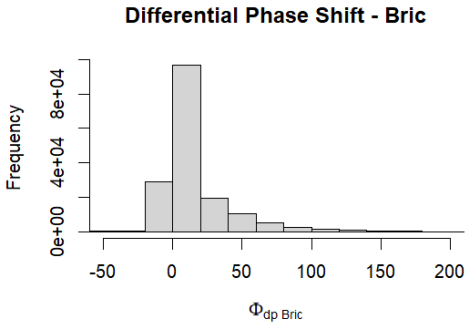

(a) Bric della Croce differential phase shift distribution through histogram, for the 25 July 2022 event and Bric della Croce - Druento radar pair

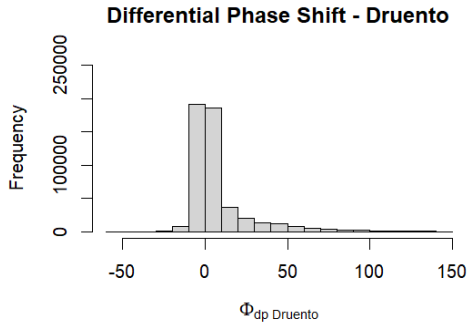

(b) Druento differential phase shift distribution through histogram, for the 25 July 2022 event and Bric della Croce - Druento radar pair

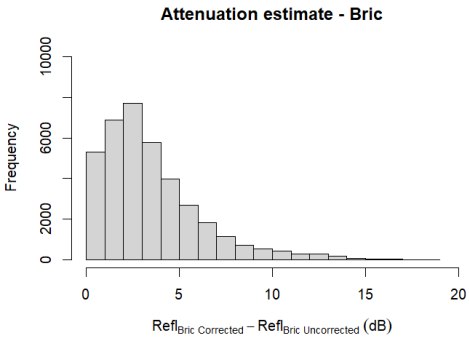

(c) Bric della Croce attenuation distribution through histogram, for the 25 July 2022 event and Bric della Croce - Druento radar pair

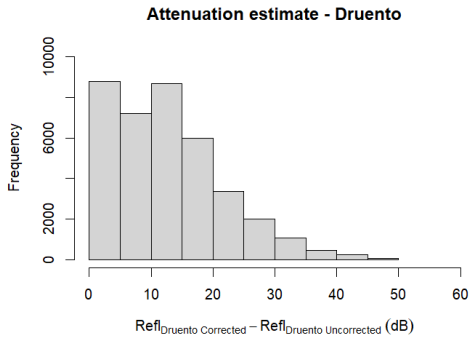

(d) Druento attenuation distribution through histogram, for the 25 July 2022 event and Bric della Croce - Druento radar pair

Figure 4.13: Histograms for differential phase shift and attenuation representations for 25 July 2022 and Bric della Croce - Druento radar pair.

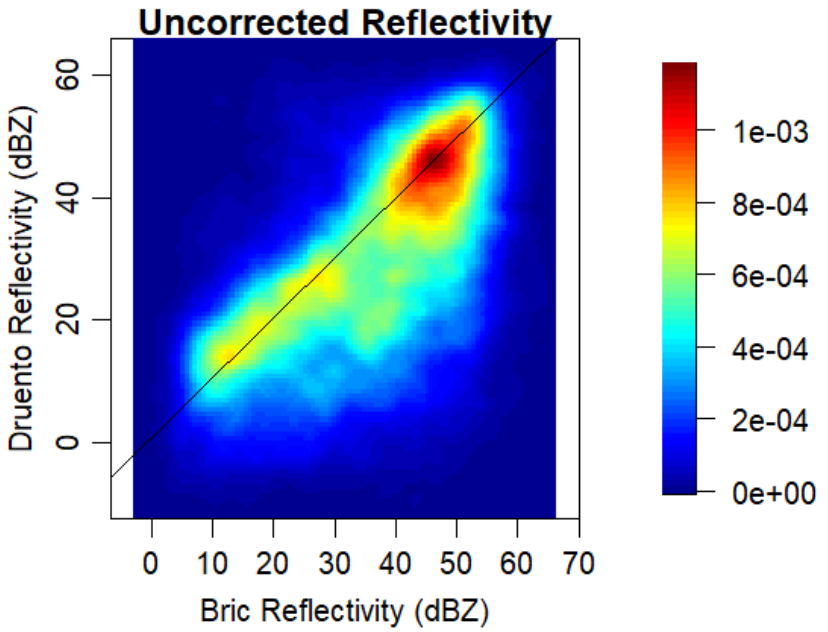

(a) Density plot for uncorrected reflectivity values, for the 25 July 2022 event and Bric della Croce - Druento radar pair.

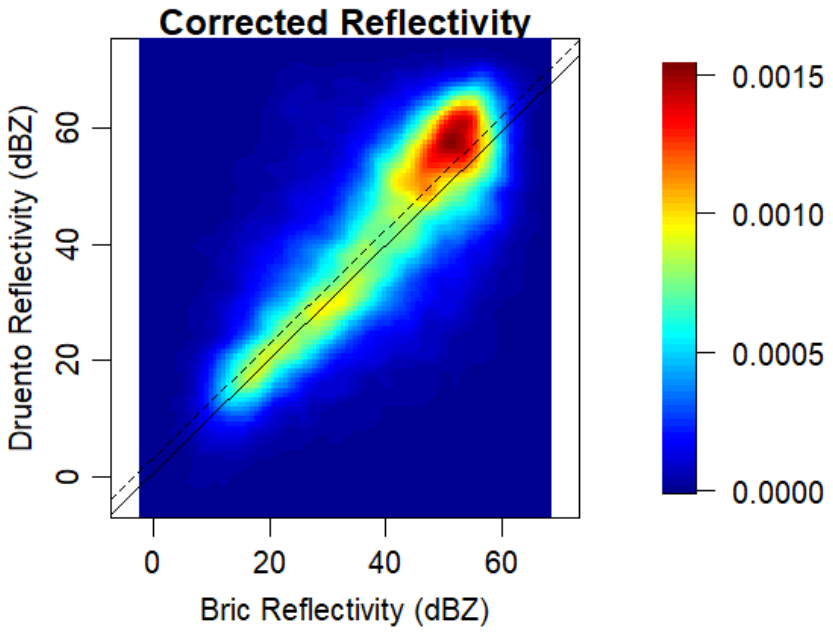

(b) Density plot for corrected reflectivity values (with the fixed coefficient), for the 25 July 2022 event and Bric della Croce - Druento radar pair. The dashed line represents the interpolating line obtained after applying the corrected calibration bias, with a unit slope (equal to 1) and an intercept corresponding to the estimated calibration bias.

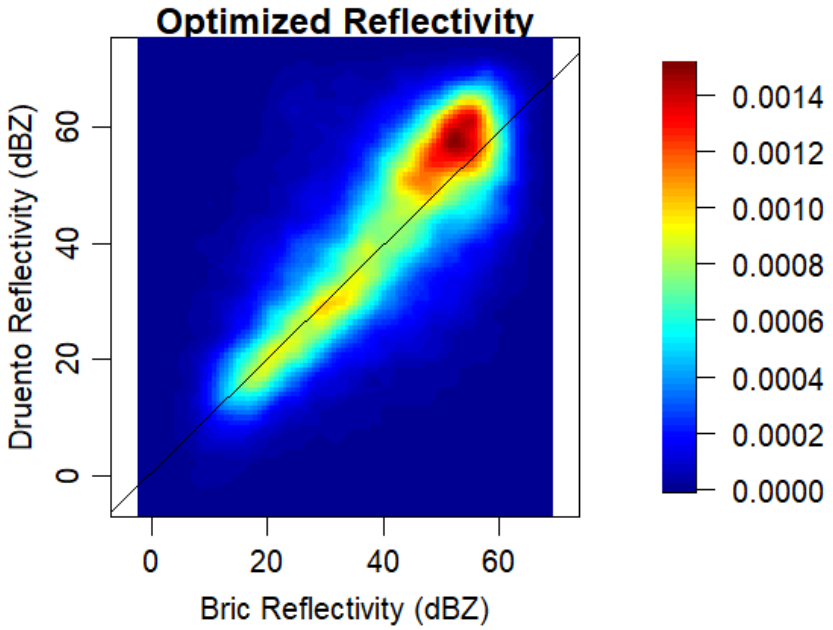

(c) Density plot for optimized reflectivity values, for the 25 July 2022 event and Bric della Croce - Druento radar pair.

Figure 4.14: Density plots of uncorrected, corrected and optimized reflectivity values for 25 July 2022 and Bric della Croce - Druento radar pair.

this behaviour. The underlying reason is the relatively weak attenuation associated with the event when observed by the second radar pair. Due to the short distance separating the two instruments, it is more difficult to capture a sufficiently attenuated event occurring between them. Conversely, the first radar pair covers a much larger area, increasing the likelihood of observing events with stronger attenuation effects.

Additional factors further limit the applicability of certain events to the C–X pair. The Druento radar is not always operational, resulting in incomplete datasets for some cases. Moreover, the X-band radar operates with three elevation angles characterized by relatively high beam angles, which reduces the number of intersection points and limit the analysis to ranges close to the Druento radar. This significantly reduces the number of matched points, thus limiting the appliability of the linear regression analysis to few cases.

Finally, since the X-band operates at a higher frequency than the C-band and is therefore more prone to attenuation, a correspondingly larger differential phase shift is required for an event to be considered a suitable candidate for reliable attenuation coefficient estimation.

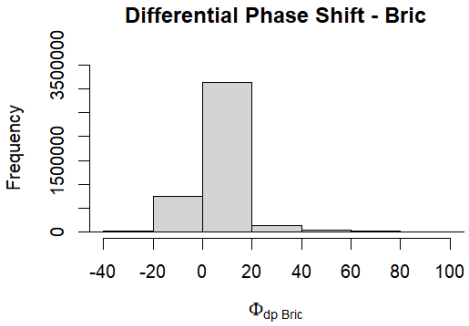

(a) Bric della Croce differential phase shift distribution through histogram, for the 16 April 2025 event and Bric della Croce - Monte Settepani radar pair

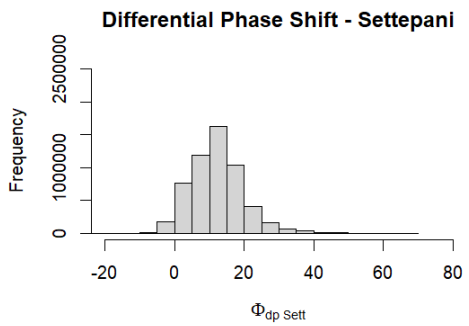

(b) Monte Settepani differential phase shift distribution through histogram, for the 16 April 2025 event and Bric della Croce - Monte Settepani radar pair

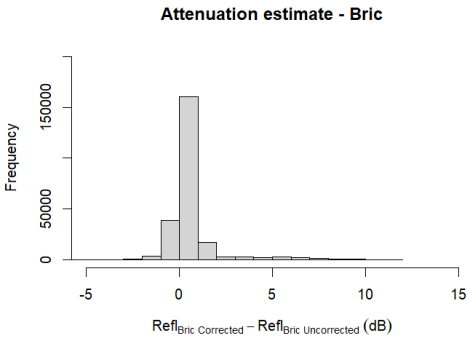

(c) Bric della Croce attenuation distribution through histogram, for the 16 April 2025 event and Bric della Croce - Monte Settepani radar pair

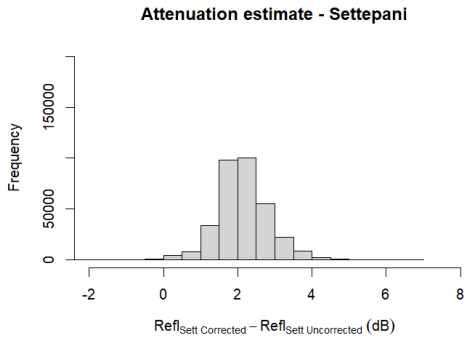

(d) Monte Settepani attenuation distribution through histogram, for the 16 April 2025 event and Bric della Croce - Monte Settepani radar pair

Figure 4.15: Histograms for differential phase shift and attenuation representations for 16 April 2025 and Bric della Croce - Monte Settepani radar pair.

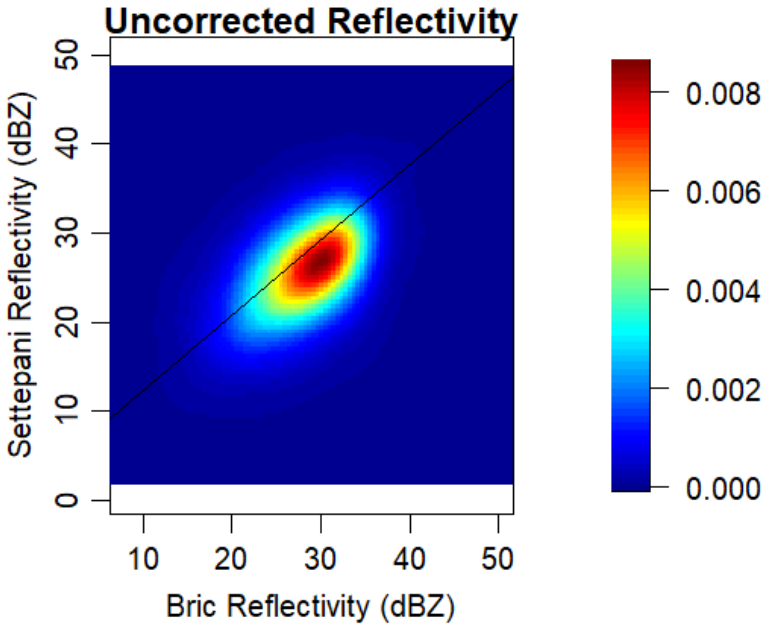

(a) Density plot for uncorrected reflectivity values, for the 16 April 2025 event and Bric della Croce - Monte Settepani radar pair.

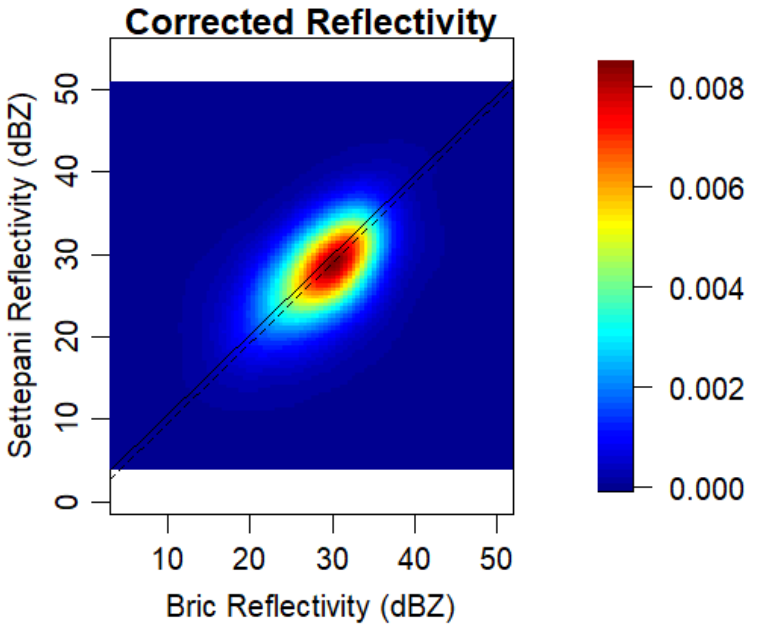

(b) Density plot for corrected reflectivity values (with the fixed coefficient), for the 16 April 2025 event and Bric della Croce - Monte Settepani radar pair. The dashed line represents the interpolating line obtained after applying the corrected calibration bias, with a unit slope (equal to 1) and an intercept corresponding to the estimated calibration bias.

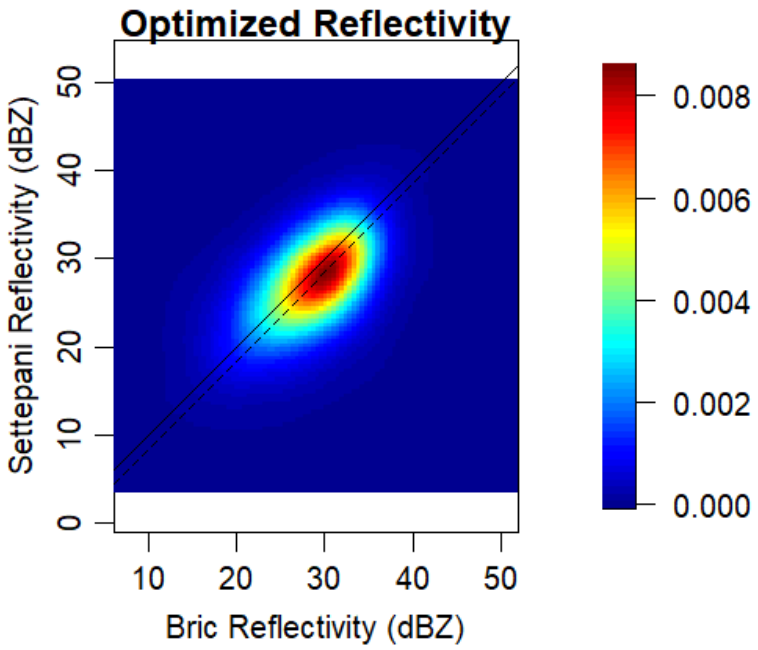

(c) Density plot for optimized reflectivity values, for the 16 April 2025 event and Bric della Croce - Monte Settepani radar pair. The dashed line represents the interpolating line obtained after applying the optimized calibration bias, with a unit slope (equal to 1) and an intercept corresponding to the estimated calibration bias.

Figure 4.16: Density plots of uncorrected, corrected and optimized reflectivity values for 16 April 2025 and Bric della Croce - Monte Settepani radar pair.

4.5 Attenuation coefficient variability and consequences on the QPEs

The comparison between the α values obtained through the optimization procedure and those derived from the theoretical simulation (Chapter 2.4.2) shows that the optimized coefficients fall within the physically consistent range predicted by the model. This agreement supports the physical validity of the optimization results.

The variability of the attenuation coefficient α is reflected in the variability of the corresponding QPE estimates. Therefore, estimating event-based values of α through the developed optimization methodology, either higher or lower than those commonly adopted by Arpa, implies obtaining different precipitation estimates.

To this end, a procedure was implemented to compare three precipitation scenarios:

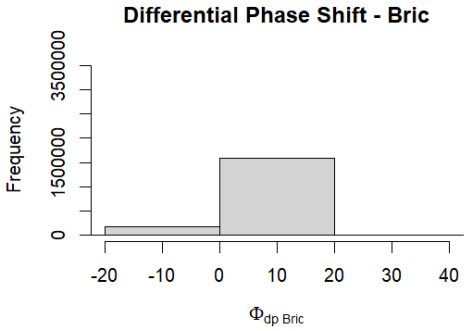

(a) Bric della Croce differential phase shift distribution through histogram, for the 16 April 2025 event and Bric della Croce - Druento radar pair

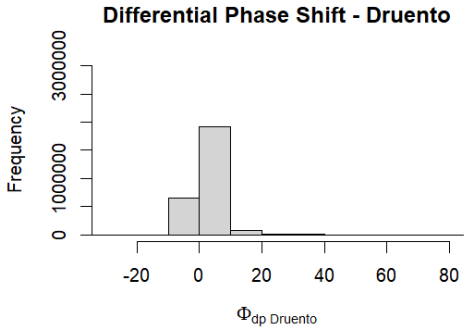

(b) Druento differential phase shift distribution through histogram, for the 16 April 2025 event and Bric della Croce - Druento radar pair

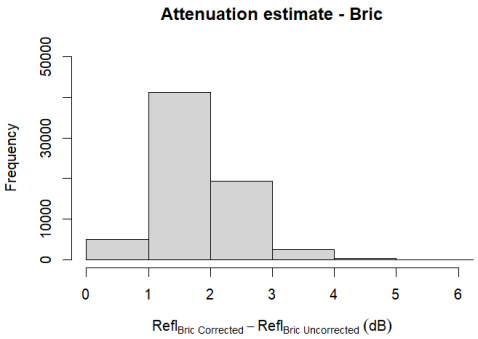

(c) Bric della Croce attenuation distribution through histogram, for the 16 April 2025 event and Bric della Croce - Druento radar pair

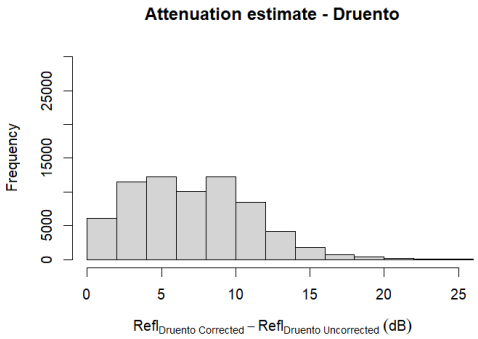

(d) Druento attenuation distribution through histogram, for the 16 April 2025 event and Bric della Croce - Druento radar pair

Figure 4.17: Histograms for differential phase shift and attenuation representations for 16 April 2025 and Bric della Croce - Druento radar pair.

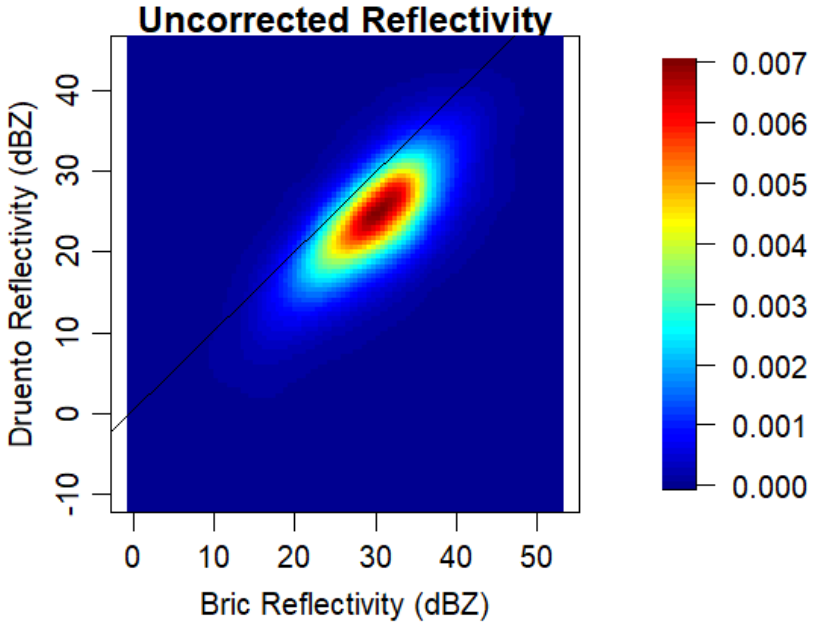

(a) Density plot for uncorrected reflectivity values, for the 16 April 2025 event and Bric della Croce - Druento radar pair.

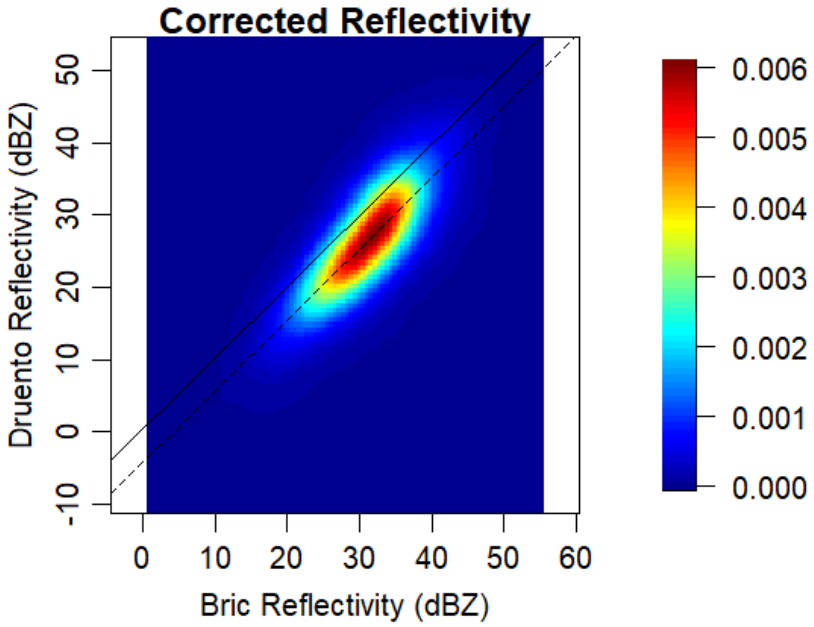

(b) Density plot for corrected reflectivity values (with the fixed coefficient), for the 16 April 2025 event and Bric della Croce - Druento radar pair. The dashed line represents the interpolating line obtained after applying the corrected calibration bias, with a unit slope (equal to 1) and an intercept corresponding to the estimated calibration bias.

Figure 4.18: Density plots of uncorrected and corrected reflectivity values for 16 April 2025 and Bric della Croce - Druento radar pair.

- Reflectivity not corrected for attenuation,
- Reflectivity corrected using fixed operational coefficients,
- Reflectivity corrected using coefficients optimized through the methodology developed in this thesis.

The objective is to quantify how variations in the attenuation coefficient propagate into the QPE estimates and, consequently, into the total accumulated precipitation over the entire event.
The analysis was conducted using PPI scans from the Bric della Croce and Druento radars, acquired every 5 minutes, considering a single elevation angle selected consistently with the vertical structure of the precipitation in order to ensure a representative description of the phenomenon.
For the Bric della Croce radar, the 2.0° elevation was selected, while for the Druento radar the lowest available elevation, 4.5°, was used. Accordingly, PPI scans including all 360 azimuths were extracted for each radar scan of the event, with a temporal resolution of 5 minutes. For each PPI, horizontal reflectivity and the estimated differential phase were retrieved.
Subsequently, the Marshall–Palmer relationship linking reflectivity Z to rain rate R was applied ([3]):

$$Z = a\ R^b, \tag{4.8}$$

where the coefficients are defined as:

$$a = 300,\ b = 1.5 \tag{4.9}$$

and Z is expressed in linear units:

$$Z = 10^{(dBZ/10)} \tag{4.10}$$

Eq. (4.8) can be inverted to retrieve the rain rate in mm/h as:

$$R = \left(\frac{Z}{a}\right)^{\frac{1}{b}}. \tag{4.11}$$

The procedure was applied to the three different scenarios: the chosen fixed coefficients correspond to the Arpa ones (0.1 dB/deg for Bric della Croce, C-band, and 0.34 dB/deg for Druento, X-band); while for the third scenario coefficients are derived from the event-specific attenuation optimization. Indeed, for the cases presented below, values of $\alpha = 0.06\ dB/deg$ were considered for the Bric della Croce radar for the 28 August 2025 event and $\alpha = 0.15\ dB/deg$ for the 25 July 2022 event, while $\alpha = 0.26\ dB/deg$ was adopted for the X-band radar for the 28 August 2025 event. Therefore, for each of the three scenarios, the reflectivity correction was applied accordingly with equation 2.24.
In order to compute the total precipitation accumulation H for each event, the instantaneous rain rate estimates obtained in the previous steps were temporally integrated over the duration of the event, assuming a sampling interval t of 5 minutes:

$$H = \sum_{t} R(t)\ \Delta t \tag{4.12}$$

This procedure allowed the generation of accumulated precipitation maps for each event.
To quantify variability, absolute differences between the scenarios and their corresponding percentage differences were calculated. These were represented in polar PPI visualizations.

The results demonstrate that the parametrization of the attenuation coefficient plays a crucial role in QPE estimation and that assuming a fixed attenuation coefficient represents a limitation. Conversely, the optimization methodology could provide more accurate precipitation estimates, as it accounts for the actual microphysical characteristics of the investigated precipitation events. In Panels 4.19, 4.21 and 4.23 the accumulated precipitation is described, while Figures 4.20, 4.22, and 4.24 show absolute (left column) and percentage (right column) differential accumulation. Rows compare the corrected and uncorrected scenarios (top), optimized and uncorrected scenarios (middle), and optimized and corrected scenarios (bottom).
The 28 August 2025 event analysed for the Bric della Croce radar highlights the effect of an optimized attenuation coefficient lower than the fixed operational one. The accumulated rainfall maps (Figure 4.19) show discrepancies

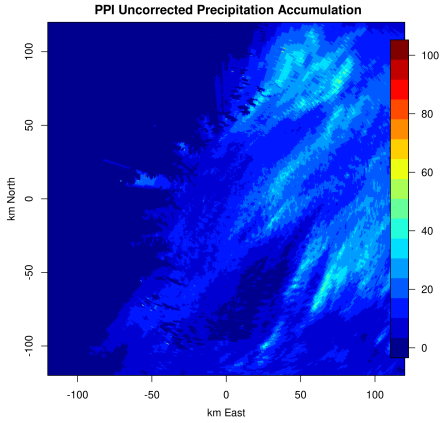

(a) PPI Uncorrected accumulation

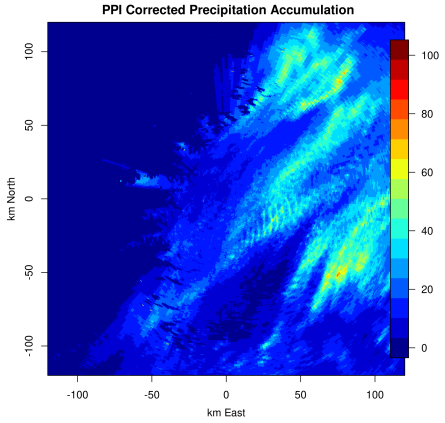

(b) PPI Corrected accumulation

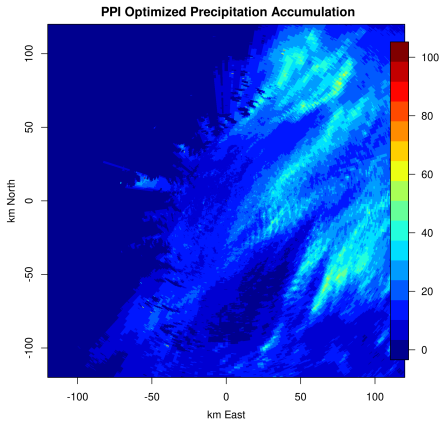

(c) PPI Optimized accumulation

Figure 4.19: Comparison between uncorrected, corrected and optimized QPE scenarios for the 28 August 2025 event (with PPI representation) with respect to the Bric della Croce radar.

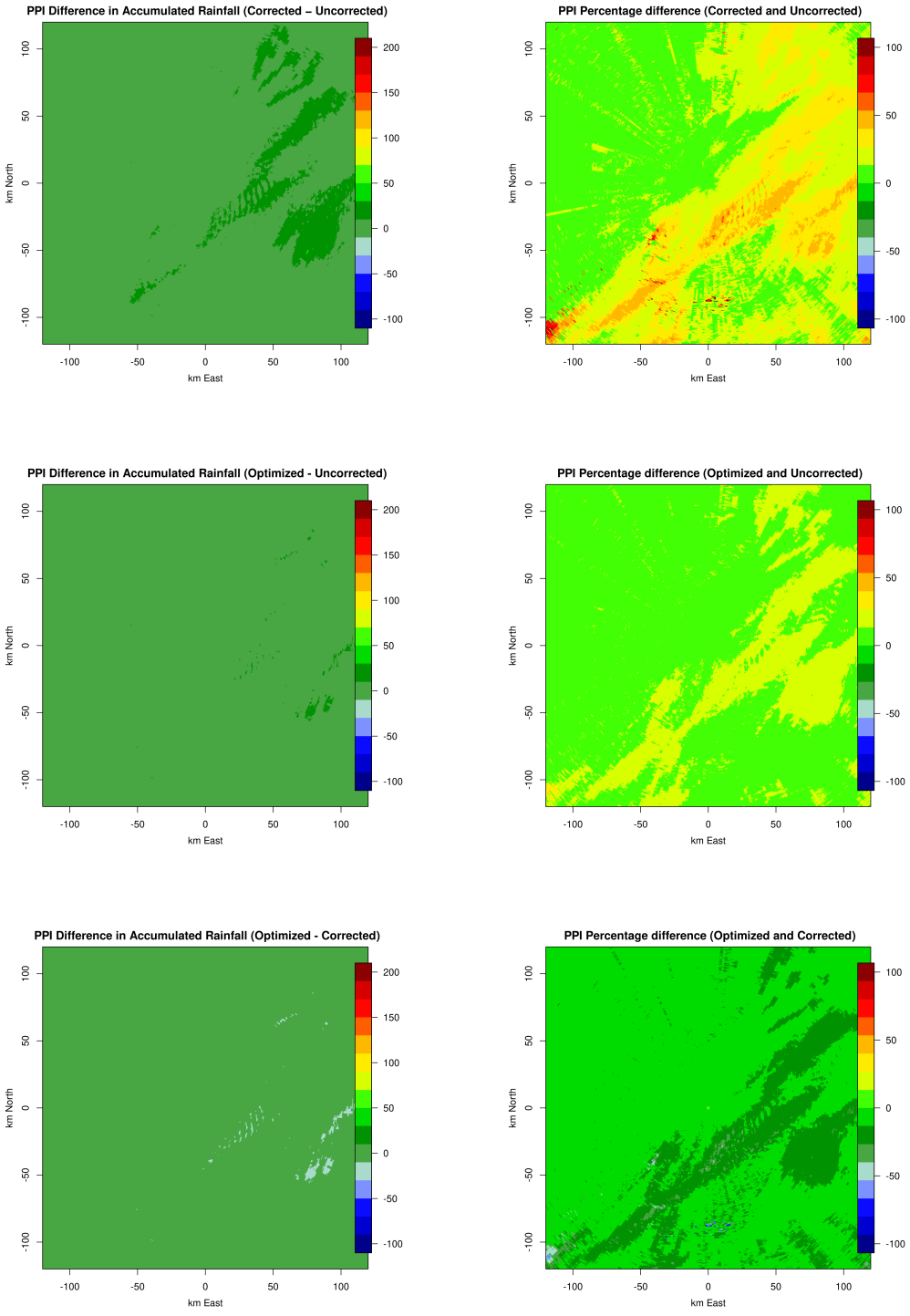

Figure 4.20: Absolute and percentage differential accumulation between uncorrected, corrected and optimized QPE scenarios for the 28 August 2025 event in PPI representation, with respect to the Bric della Croce radar.

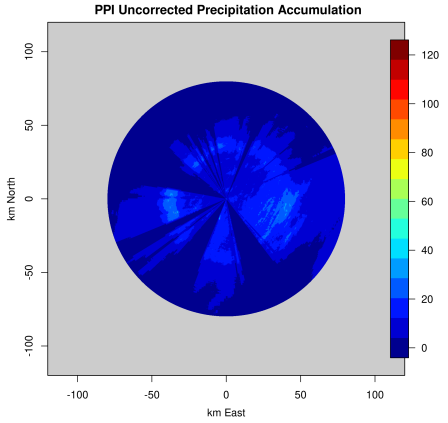

(a) PPI Uncorrected accumulation

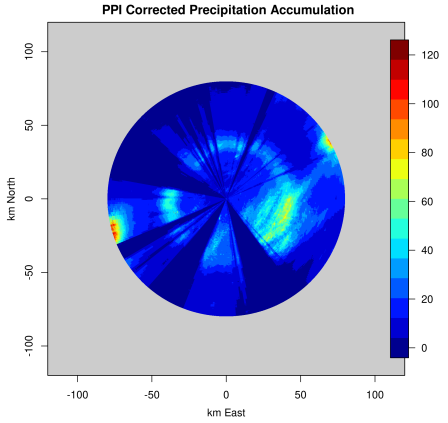

(b) PPI Corrected accumulation

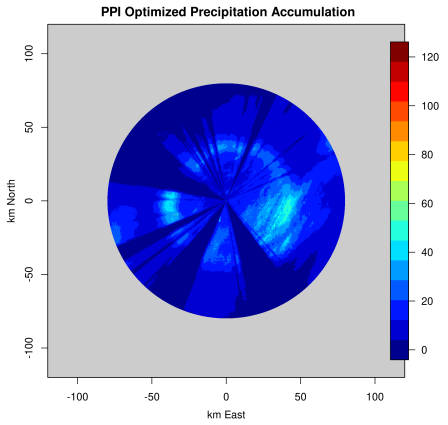

(c) PPI Optimized accumulation

Figure 4.21: Comparison between uncorrected, corrected and optimized QPE scenarios for the 28 August 2025 event (with PPI representation) with respect to the Druento radar.

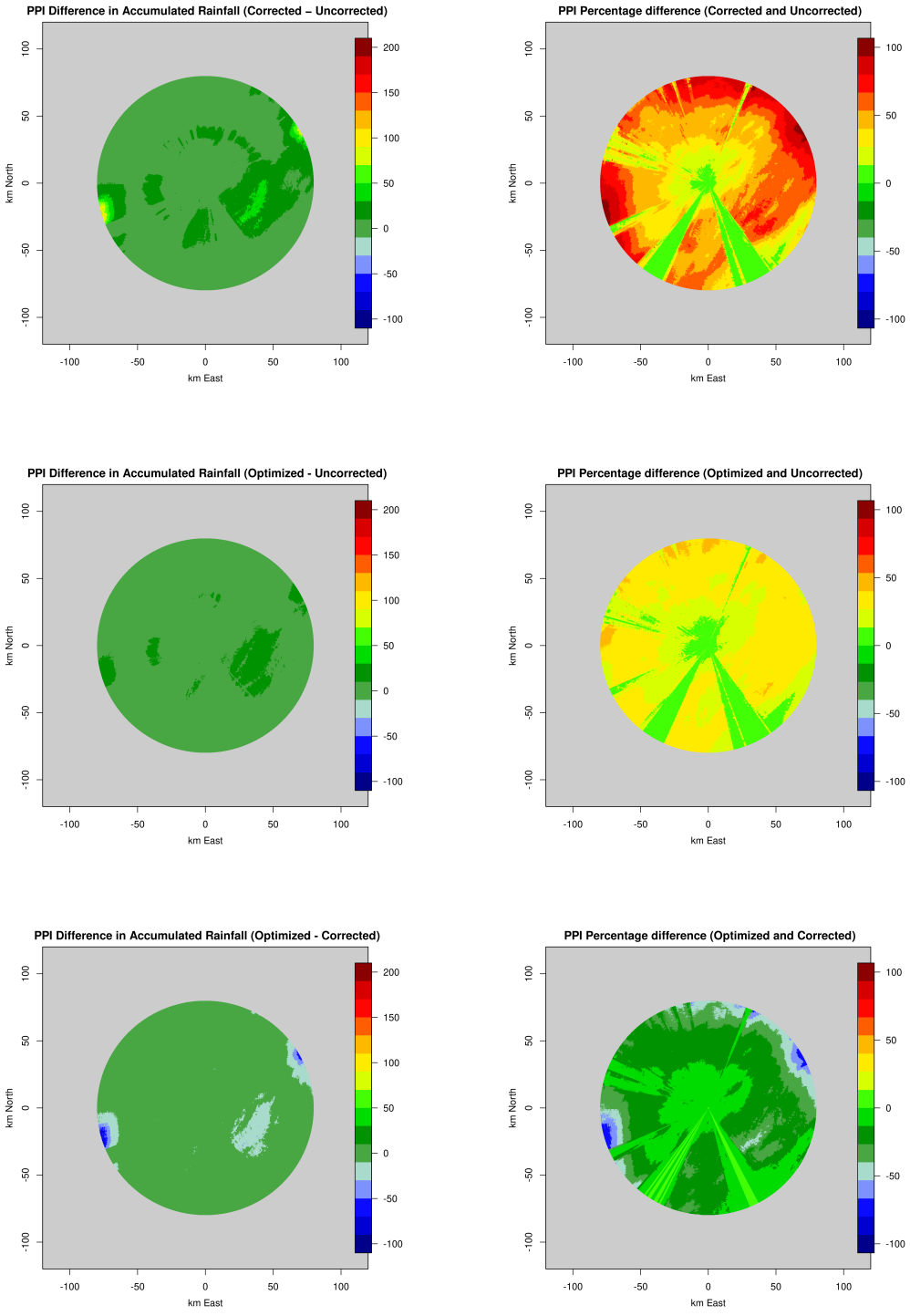

Figure 4.22: Absolute and percentage differential accumulation between uncorrected, corrected and optimized QPE scenarios for the 28 August 2025 event in PPI representation, with respect to the Druento radar.

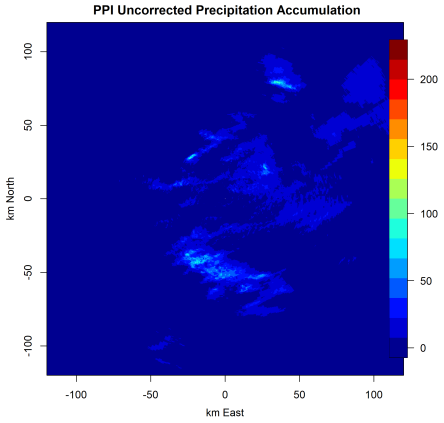

(a) PPI Uncorrected accumulation

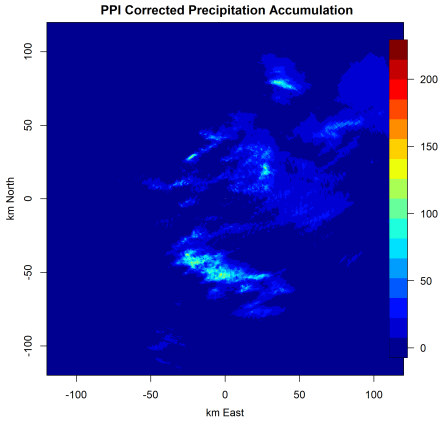

(b) PPI Corrected accumulation

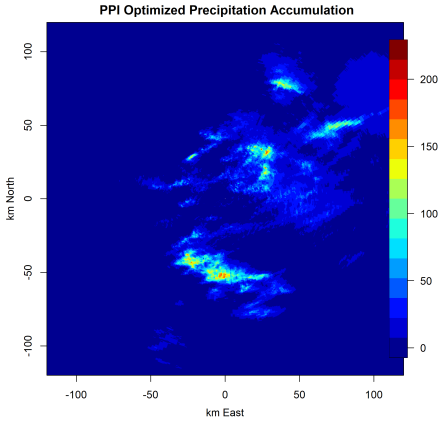

(c) PPI Optimized accumulation

Figure 4.23: Comparison between uncorrected, corrected and optimized QPE scenarios for the 25 July 2022 event (with PPI representation) with respect to the Bric della Croce radar.

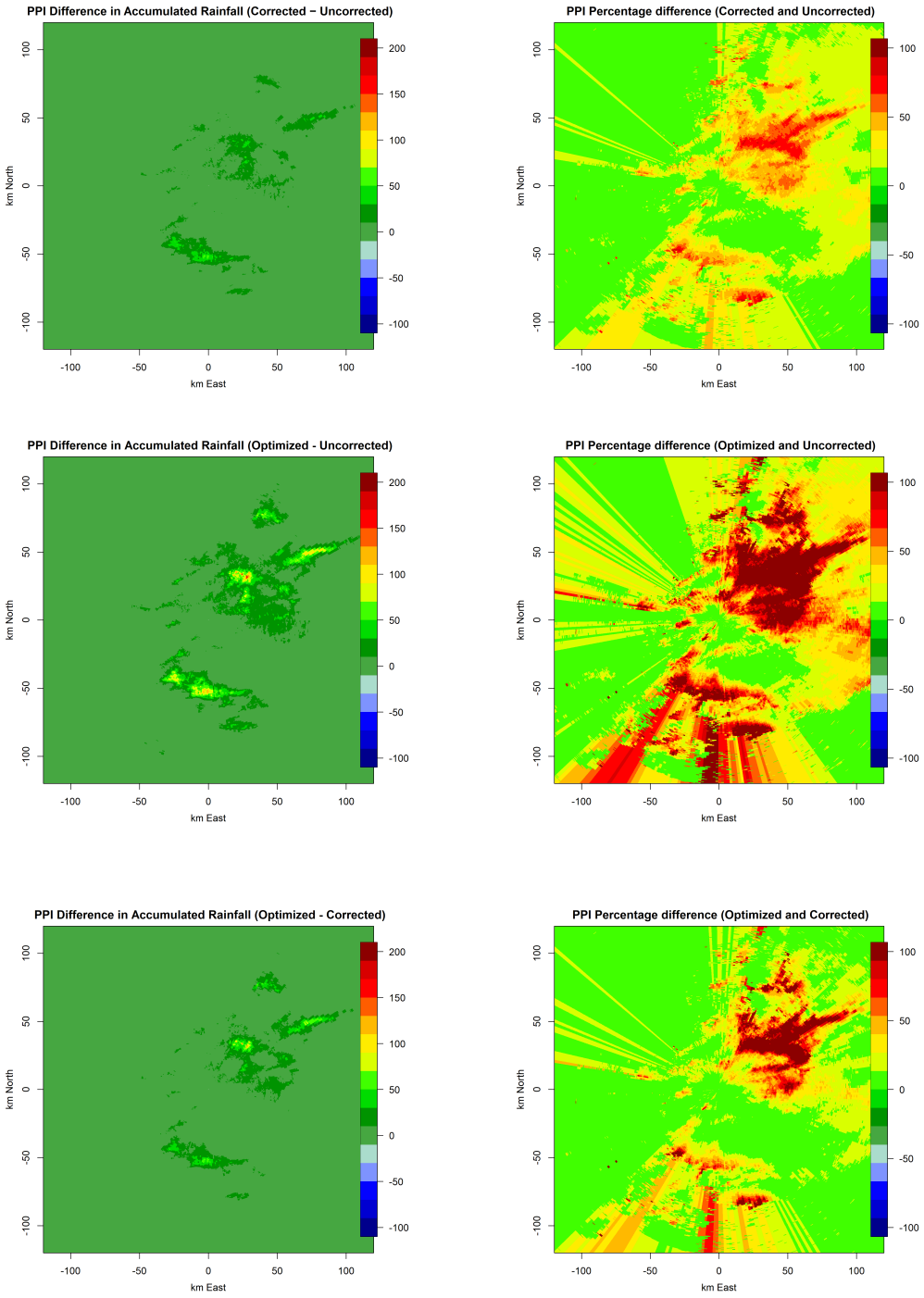

Figure 4.24: Absolute and percentage differential accumulation between uncorrected, corrected and optimized QPE scenarios for the 25 July 2022 event in PPI representation, with respect to the Bric della Croce radar.

in the maximum precipitation values, which become even more evident in the differential maps, both in absolute and percentage terms (Figure 4.20). In some areas, differences in accumulated rain reach 20-30 mm. Since the optimized attenuation coefficient α is lower than the fixed one, the resulting correction is smaller. Consequently, the optimized reflectivities are lower, leading to an underestimation of precipitation compared to the standard correction case.
This behaviour is confirmed by the negative differences between the rain accumulations derived from corrected reflectivity and those derived from optimized reflectivity. Adopting the fixed coefficient implies estimating approximately 20 mm more than what is obtained using the optimized coefficient. The percentage differences, calculated with respect to the accumulated rainfall values corrected using the Arpa coefficient, further emphasize this aspect, showing reductions of up to -20% in the optimized accumulated estimates.
For the same radar, the 25 July 2022 event was analysed in order to demonstrate the consequences of selecting an optimized coefficient higher than the fixed one. The absolute differential accumulated maps (Figure 4.24) highlight discrepancies already visible in the cumulative rainfall maps: in some areas, the difference in rain accumulation between optimized and corrected reflectivities exceeds 50 mm, corresponding to a percentage increase of up to $+100\%$.
Finally, the maps related to the X-band radar of Druento for the 28 August 2025 event were analysed. The differential accumulated map (Figure 4.22) between optimized and corrected reflectivities shows minima of -70 mm, corresponding to a substantial percentage decrease relative to the corrected accumulation. It is furthermore worth noting that the PPI maps have a reduced spatial extent compared to the previous cases, consistently with the shorter range coverage of the X-band radar.

Chapter 5

Conclusions

This thesis develops and implements a methodology for the optimisation of attenuation coefficients in C- and X-band weather radars belonging to Arpa Piemonte, specifically the C-bands Bric della Croce and Monte Settepani radars and the X-band Druento radar.

The proposed approach builds upon the conventional inter-radar calibration technique and extends it to derive event-specific attenuation coefficients through regression analysis applied at radar beam intersection points. A detailed description of the methodological framework is provided in Chapter 3.3.

Overall, the proposed methodology enables event-adaptive attenuation correction within radar networks by exploiting overlapping volumes and differential phase information to retrieve physically consistent attenuation coefficients, ultimately enhancing reflectivity consistency across systems.

The results show that the choice of temporal aggregation has a pronounced impact on the robustness of the results. Shorter intervals, such as 4- or 6-hour, produce greater variability and, in some cases, unrealistic negative attenuation coefficients due to limited sampling. In contrast, a full 24-hour aggregation for significant rain events provides sufficient data to ensure stable estimates of both the attenuation coefficients and the calibration biases, minimizing statistical uncertainty. This highlights the importance of selecting appropriate temporal windows for quantitative precipitation estimation, particularly when applying linear regression-based optimization methods.

Frequency-dependent effects clearly emerge from the comparison between radar

pairs. The C-band configuration exhibits moderate attenuation, whereas the inclusion of the X-band radar enhances sensitivity to attenuation processes due to its higher operating frequency. Consequently, low-intensity or short-duration events are less suitable for C–X analysis, while intense precipitation cases allow reliable coefficient estimation across all radar combinations.

For the C-band Bric della Croce–Monte Settepani pair, attenuation coefficients deriving from optimization methodology range between 0.05 dB/deg and 0.15 dB/deg. The correction procedure (with the Φ_{dp} - Method) reduces reflectivity standard deviation from values up to 5-9 dB in uncorrected data to approximately 4-6 dB after optimization. For the C–X Bric della Croce–Druento pair, $\alpha_{X,\text{Optimized}}$ ranges between 0.22 dB/deg and 0.34 dB/deg, with standard deviations decreasing from over 8-13 dB to approximately 6–10 dB. These reductions confirm the effectiveness of the optimization in improving internal radar consistency.

A central outcome of this work concerns the intrinsic variability of the attenuation coefficient α, both as a function of the radar operating frequency and the microphysical characteristics of the precipitation. Specifically, theoretical simulations based on integrating scattering properties over realistic raindrop size distributions (DSDs) indicate that for C-band radars, α spans approximately from 0.06 dB/deg to 0.28 dB/deg, while for X-band radars, it ranges from 0.23 dB/deg to 0.59 dB/deg, depending on the mass-weighted mean diameter D_m and the shape parameter μ. The highest values of α are associated with small, nearly spherical drops (low D_m), where the specific differential phase shift K_{DP} is low, resulting in a large ratio A_H/K_{DP}. As drops grow larger and increasingly oblate, α decreases, highlighting the sensitivity of this parameter to microphysical conditions.

This variability has direct implications for QPEs. For instance, in the 28 August 2025 event observed by the Bric della Croce radar, using an optimized α of 0.06 dB/deg instead of the fixed operational value of 0.1 dB/deg led to reductions in accumulated rainfall of up to 20% in certain areas, corresponding to absolute differences of 20-30 mm. Conversely, for the 25 July 2022 event observed by the Bric della Croce radar, an optimized coefficient higher than the fixed one

produced differences exceeding 50 mm, with percentage increases reaching 100%. For the X-band radar of Druento and 28 August 2025 case study, differences between corrected and optimized QPEs reached 70 mm, emphasizing the even stronger sensitivity of QPEs at higher frequencies.

Applying a fixed attenuation coefficient, as commonly done in operational procedures, can lead to substantial systematic over- or underestimation of rainfall. By contrast, an event-specific optimization of α ensures that the QPEs reflect the actual microphysical properties of the precipitation, improving both the accuracy and physical consistency of the estimated rainfall. In conclusion, accounting for α variability should be considered in operational QPE procedures. Despite these promising results, several obstacles must be considered when evaluating its transition to an operational framework.

Firstly, the optimization procedure strongly depends on the availability and quality of Φ_{dp} measurements. Events characterized by weak attenuation, noisy differential phase signals, or limited spatial overlap between radars reduce the number of valid intersection points and weaken regression stability.

Secondly, an additional and specific criticality concerns the configuration of the X-band radar system. The reduced spatial coverage, due to a limited elevations number, and shorter maximum range compared to the C-band system, limit the extent of overlapping volumes and reduce the number of statistically valid samples available for regression. Furthermore, the higher sensitivity of X-band measurements to attenuation and noise requires the presence of sufficiently attenuated volumes to ensure statistical significance of the regression. In weakly attenuated events, the reduced Φ_{dp} signal limits the robustness of the coefficient estimation.

Future developments should therefore aim at reinforcing the physical basis of the method and enhancing robustness under operational constraints. Since the observed variability of α is intrinsically linked to the drop size distribution (DSD), a promising direction involves retrieving microphysical information from polarimetric variables such as Z_{DR} and K_{DP} consistency relations. Disdrometers provide direct information on drop size distribution (DSD) parameters, thereby the systematic use of their measurements would allow independent

validation of α–DSD relationships before transferring the correction scheme to operational QPE [6]. Moving toward a physically based estimation of α, rather than relying exclusively on statistical optimization, would significantly improve the stability of the method, particularly under limited sampling conditions or weak attenuation scenarios. In parallel, rain gauge networks remain essential for verifying cumulative rainfall maps and quantifying residual biases at the surface, ensuring that attenuation corrections translate into measurable improvements in surface precipitation estimates.

A second research direction concerns the extension to C-band systems of attenuation coefficient estimate approaches originally developed for S-band radars. At S-band, attenuation is negligible, so polarimetric variables such as Z_h and Z_{dr} can be regarded as intrinsic and directly linked to precipitation microphysics. In particular, Z_{dr} provides information on the median volume diameter D_m, while the joint behaviour of Z_{dr} and Z_h reflects the nature of the drop size distribution. A small slope in the Z_{dr}-Z_h relation indicates that increases in reflectivity are mainly driven by higher drop concentration rather than larger drop size. This is consistent with relatively small Φ_{dp} values (the differential phase is mainly affected by large oblate particles), which scale with the integrated water content along the radar path. While these relationships can be exploited directly at S-band, at C-band both Z_h and Z_{dr} are affected by attenuation. Therefore, transferring S-band consistency-based frameworks to C-band requires explicitly accounting for attenuation effects within the retrieval, enabling physically constrained estimation of the attenuation coefficient α [7].

More broadly, future work should aim at designing automated quality-control procedures and dynamic decision criteria capable of determining when event-specific optimization is reliable and when fallback strategies are required. The development of such adaptive frameworks would represent a key step toward bridging the gap between research-oriented methodologies and fully operational radar-based QPE systems.

In conclusion, this work demonstrates that attenuation coefficient variability is not merely a secondary calibration issue, but a central factor in ensuring physically consistent and reliable radar-based precipitation estimates. By combining

statistical optimization, microphysical interpretation, and multi-instrument validation, the proposed framework provides a scientifically grounded pathway toward more accurate and adaptive radar QPE systems.

Appendix A

K_{dp} estimation function

The function K_{dp} *estimation* is defined with the aim of estimating K_{dp} in $^\circ/km$ from the monotonic increasing profile of Φ_{dp}.

The differential phase shift is first cleaned of values associated with so-called *clutters*. Omitting this step would introduce significant errors in the derivation of the specific differential phase shift K_{dp}. The filtering is performed by applying a threshold to the copolar correlation coefficient ρ_{hv}, which is closely related to the type of target. Low ρ_{hv} values indicate non-meteorological targets, such as buildings, mountains, and other objects classified as *clutters*. By selecting cells with $\rho_{hv} > 0.7$, only meteorological targets are identified [8].

After that, any isolated values of Φ_{dp} dataset are removed. This is possible by counting the differential phase shift values available within a moving window along each radius. For each interval, the valid phase data are evaluated and are considered valid only if, within that window, the number of non-NA Φ_{dp} values is greater than half the number of valid Φ_{dp} values, again within the same window. Therefore, if the count of valid Φ_{dp} values exceeds half the total number of values, the corresponding window block is considered; otherwise, it is excluded. The reason behind this procedure is that isolated differential phase shift values are linked to noise and signal anomalies, which would erroneously influence the estimation of the specific differential phase shift K_{dp}. The K_{dp} is, in fact, nothing more than the derivative of the Φ_{dp} curve. If the isolated values were not filtered, the spline used for the derivation would undergo a curve characterised by a steep slope in order to adapt to the anomalous value. This

would cause an incorrect estimate in K_{dp}, which at that point would assume enormous values indicating very heavy rainfall that does not actually exist [8]. After the Φ_{dp} values have been properly filtered, the estimation of K_{dp} is performed through spline-based processing. Due to phase folding, the raw Φ_{dp} measurements may exhibit artificial discontinuities, resulting in a fragmented profile along range. To overcome this issue, the differential phase is first projected onto the complex plane:

$$w = cos(\Phi), \tag{A.1}$$

$$p = sin(\Phi). \tag{A.2}$$

By representing the phase on the unit circle, this transformation effectively removes the ambiguity introduced by folding, ensuring continuity of the signal [8].

Subsequently, the phase variation with respect to range is reconstructed using the derivative formulation reported in Equation A.3:

$$\frac{d\Phi}{dr} = \frac{w\ dp/dr - p\ dw/dr}{w^2 + p^2}. \tag{A.3}$$

Finally, by exploiting the relationship between differential phase shift and specific differential phase shift (Equation 2.22), K_{dp} is calculated as:

$$K_{dp} = \frac{1}{2} \cdot \frac{d\Psi}{dr} \cdot \frac{180}{\pi}. \tag{A.4}$$

The factor of $\frac{1}{2}$ arises because the differential phase shift accounts for the entire round-trip path of the radar beam [8].

Finally, the Φ_{dp} and K_{dp} profiles are reconstructed to ensure that both data series are monotonically increasing and that any gaps between valid measurements are filled, resulting in a continuous function along the entire radar beam.

Appendix B

Statistical metrics for sub-aggregations

Parameter	B1	B2	B3	B4	B5	B6	B7	B8	B9	B10	B11	B12
Valid Points	421	21787	29524	53215	4482	89058	96568	8508	0	5278	182495	39755
$\alpha_{\text{C,Optimized}}$	0.11	0.02	0.08	0.08	0.04	0.06	0.07	0.10	NA	0.08	0.05	0.05
$\text{StDev}_{\text{Uncorrected}}$	4.14	4.71	6.36	8.49	8.17	9.26	7.18	5.37	NA	6.07	5.01	4.33
$\text{StDev}_{\text{Corrected}}$	4.12	4.77	6.02	7.02	8.40	8.27	5.36	4.62	NA	6.05	5.01	4.36
$\text{StDev}_{\text{Optimized}}$	4.12	4.71	6.01	6.99	7.99	7.68	4.88	4.62	NA	6.04	4.96	4.22
$\text{Bias}_{\text{Corrected}}$	-5.01	2.02	0.77	-0.37	-0.72	2.48	2.08	-0.56	NA	1.17	0.58	-2.18
$\text{Bias}_{\text{Optimized}}$	-5.24	0.45	0.56	0.29	-0.48	0.48	0.14	-0.58	NA	0.75	-0.51	-0.44
$\text{Corr}_{\text{Uncor.}}$	0.68	0.74	0.72	0.59	0.58	0.49	0.58	0.82	NA	0.76	0.76	0.71
$\text{Corr}_{\text{Corr.}}$	0.69	0.74	0.76	0.76	0.57	0.69	0.84	0.90	NA	0.76	0.76	0.73
$\text{Corr}_{\text{Optim.}}$	0.68	0.74	0.75	0.74	0.59	0.68	0.83	0.89	NA	0.76	0.76	0.74
$\text{Bias}_{\Phi_{dp}\,\text{low}}$	-1.02	0.17	0.03	-1.15	-2.47	-1.78	0.69	0.71	-4.00	0.55	0.47	0.61
$\alpha_{C,\Phi_{dp}\,\text{high}}$	-0.08	0.02	0.08	0.10	0.04	0.05	0.07	0.10	NA	0.06	0.08	0.02

Table B.1: Statistical metrics for the 2-hour aggregation on 28 August 2025 for the Bric della Croce and Settepani radars. The blocks refer to the following intervals: 00:00-02:00, 02:00-04:00, 04:00-06:00, 06:00-08:00, 08:00-10:00, 10:00-12:00, 12:00-14:00, 14:00-16:00, 16:00-18:00, 18:00-20:00, 20:00-22:00, 22:00-24:00.

Parameter	**B1**	**B2**	**B3**	**B4**	**B5**	**B6**	**B7**	**B8**	**B9**	**B10**	**B11**	**B12**	**B13**
Valid Points	0	308	1397	16156	19782	7601	30729	24432	7308	277	17592	37721	67021
$\alpha_{\text{C,Optimized}}$	NA	0.244	-0.051	0.024	0.004	0.074	0.097	0.054	0.054	0.035	0.059	0.050	0.068
$\text{StDev}_{\text{Uncorrected}}$	NA	3.86	4.17	4.73	5.58	6.68	8.19	7.72	7.87	7.45	9.01	8.42	8.72
$\text{StDev}_{\text{Corrected}}$	NA	3.80	5.03	4.79	5.65	6.52	5.67	7.60	7.83	7.62	8.90	8.44	6.86
$\text{StDev}_{\text{Optimized}}$	NA	3.77	4.04	4.73	5.58	6.50	5.67	7.29	7.72	7.38	8.81	7.78	6.20
$\text{Bias}_{\text{Corrected}}$	NA	-4.83	1.29	2.13	1.75	-0.47	0.92	-1.57	-2.39	-3.20	2.13	2.01	3.44
$\text{Bias}_{\text{Optimized}}$	NA	-7.56	-1.61	0.63	-0.24	-0.74	1.12	-0.02	-0.96	-3.02	0.65	0.61	0.38
$\text{Corr}_{\text{Uncor.}}$	NA	0.67	0.71	0.74	0.73	0.61	0.53	0.69	0.62	0.57	0.53	0.57	0.52
$\text{Corr}_{\text{Corr.}}$	NA	0.69	0.62	0.74	0.73	0.64	0.79	0.74	0.64	0.59	0.56	0.66	0.76
$\text{Corr}_{\text{Optim.}}$	NA	0.68	0.66	0.74	0.73	0.64	0.77	0.75	0.64	0.59	0.56	0.67	0.77
$\text{Bias}_{\Phi_{dp}\,\text{low}}$	NA	-1.39	0.13	0.22	-0.20	1.04	1.52	-1.21	-1.82	-2.29	-5.48	0.06	-1.17
$\alpha_{C,\Phi_{dp}\,\text{high}}$	NA	-0.028	-0.012	0.021	0.020	0.096	0.093	0.068	0.070	0.039	-0.037	0.046	0.059

Parameter	**B14**	**B15**	**B16**	**B17**	**B18**	**B19**	**B20**	**B21**	**B22**	**B23**	**B24**	**B25**	**B26**
Valid Points	41973	27455	3800	11	0	0	21	8920	107293	71539	37600	2045	110
$\alpha_{\text{C,Optimized}}$	0.080	0.073	0.064	-0.105	NA	NA	-0.575	0.080	0.023	0.043	0.047	0.036	0.143
$\text{StDev}_{\text{Uncorrected}}$	6.98	5.66	4.86	1.31	NA	NA	4.27	6.17	4.92	4.96	4.28	4.45	3.50
$\text{StDev}_{\text{Corrected}}$	4.67	4.83	4.74	1.36	NA	NA	4.62	6.15	4.95	5.01	4.30	4.48	3.40
$\text{StDev}_{\text{Optimized}}$	4.47	4.68	4.68	1.29	NA	NA	3.18	6.15	4.91	4.90	4.21	4.43	3.39
$\text{Bias}_{\text{Corrected}}$	2.35	-0.73	-0.24	0.98	NA	NA	5.25	1.14	0.39	0.83	-2.35	0.63	0.79
$\text{Bias}_{\text{Optimized}}$	0.95	-0.92	-1.02	-4.37	NA	NA	-9.27	0.66	-1.48	-0.09	-0.40	-0.77	1.90
$\text{Corr}_{\text{Uncor.}}$	0.50	0.78	0.69	-0.19	NA	NA	0.28	0.76	0.74	0.74	0.71	0.77	0.06
$\text{Corr}_{\text{Corr.}}$	0.84	0.90	0.73	-0.24	NA	NA	0.26	0.76	0.75	0.74	0.74	0.77	-0.01
$\text{Corr}_{\text{Optim.}}$	0.80	0.89	0.72	-0.22	NA	NA	0.27	0.76	0.75	0.75	0.74	0.77	0.01
$\text{Bias}_{\Phi_{dp}\,\text{low}}$	1.08	0.60	0.51	-2.84	NA	-3.76	1.28	-0.07	NA	0.47	0.42	1.23	-2.66
$\alpha_{C,\Phi_{dp}\,\text{high}}$	0.081	0.079	0.090	-0.046	NA	NA	-0.187	0.045	NA	0.058	0.028	0.103	-0.014

Table B.2: Statistical metrics for the 1-hour aggregation on 28 August 2025 for the Bric della Croce and Settepani radars. The table is split into two sections for better readability.

Parameter	**B1**	**B2**	**B3**	**B4**	**B5**	**B6**	**B7**	**B8**	**B9**	**B10**	**B11**	**B12**	**B13**	**B14**	**B15**
Valid Points	0	0	0	83	490	922	344	3402	14710	9606	8086	1734	3907	11141	16108
$\alpha_{\text{C,Optimized}}$	NA	NA	NA	0.380	-0.040	-0.016	0.016	-0.033	0.089	-0.008	-0.003	-0.009	0.081	0.119	0.085
$\text{StDev}_{\text{Uncor.}}$	NA	NA	NA	4.324	4.313	3.903	3.621	4.107	4.773	5.365	6.011	7.503	6.194	7.883	7.248
$\text{StDev}_{\text{Corr.}}$	NA	NA	NA	4.168	4.711	4.160	3.929	4.613	4.750	5.428	6.117	7.743	6.088	5.335	5.686
$\text{StDev}_{\text{Optim.}}$	NA	NA	NA	3.976	4.276	3.898	3.609	4.070	4.750	5.365	6.011	7.502	6.081	5.255	5.632
$\text{Bias}_{\text{Corr.}}$	NA	NA	NA	-3.786	-4.492	2.900	-0.195	3.466	1.803	1.902	1.582	-1.058	-0.146	0.282	1.592
$\text{Bias}_{\text{Optim.}}$	NA	NA	NA	-9.335	-2.525	-0.365	-0.744	1.548	1.571	-0.505	-0.292	0.185	-0.472	0.017	2.870
$\text{Corr}_{\text{Uncor.}}$	NA	NA	NA	0.565	0.695	0.720	0.824	0.781	0.738	0.745	0.717	0.521	0.642	0.458	0.625
$\text{Corr}_{\text{Corr.}}$	NA	NA	NA	0.598	0.624	0.694	0.798	0.754	0.741	0.737	0.715	0.518	0.667	0.766	0.797
$\text{Corr}_{\text{Optim.}}$	NA	NA	NA	0.588	0.651	0.706	0.813	0.767	0.740	0.740	0.717	0.523	0.662	0.717	0.793
$\text{Bias}_{\Phi_{dp}\text{ low}}$	NA	NA	NA	-1.823	-0.156	0.290	-0.016	0.374	-0.220	-0.459	0.028	1.218	-0.915	1.022	1.929
$\alpha_{C,\Phi_{dp}\text{ high}}$	NA	NA	NA	0.086	-0.129	0.001	-0.001	-0.043	0.022	0.003	0.035	-0.052	0.055	0.110	0.093

Parameter	**B16**	**B17**	**B18**	**B19**	**B20**	**B21**	**B22**	**B23**	**B24**	**B25**	**B26**	**B27**	**B28**	**B29**	**B30**
Valid Points	13239	10868	8429	3685	1054	92	90	1439	12586	17703	15912	24549	31151	29643	17628
$\alpha_{\text{C,Optimized}}$	0.063	0.058	0.057	0.046	0.045	0.006	0.046	0.060	0.058	0.053	0.035	0.063	0.067	0.073	0.089
$\text{StDev}_{\text{Uncor.}}$	7.041	8.288	8.079	7.607	7.703	7.792	5.890	9.275	8.931	8.584	7.690	9.605	8.726	7.265	7.451
$\text{StDev}_{\text{Corr.}}$	6.470	8.083	7.943	7.645	7.725	8.189	5.906	9.207	8.852	8.540	8.224	8.228	6.789	5.452	4.326
$\text{StDev}_{\text{Optim.}}$	6.139	7.853	7.748	7.505	7.660	7.790	5.847	9.152	8.762	8.365	7.463	7.343	6.058	5.098	4.253
$\text{Bias}_{\text{Corr.}}$	-0.766	-1.734	-2.021	-2.479	-2.485	-3.612	-1.359	3.045	2.146	1.131	1.604	3.429	3.777	2.971	2.325
$\text{Bias}_{\text{Optim.}}$	0.956	-0.156	-0.860	-0.792	-0.806	-3.824	-2.515	1.123	0.549	-0.103	1.136	0.562	0.389	0.628	1.465
$\text{Corr}_{\text{Uncor.}}$	0.729	0.644	0.663	0.626	0.462	0.460	0.686	0.618	0.527	0.546	0.647	0.440	0.517	0.591	0.487
$\text{Corr}_{\text{Corr.}}$	0.800	0.711	0.707	0.632	0.488	0.478	0.704	0.633	0.551	0.568	0.691	0.707	0.769	0.786	0.878
$\text{Corr}_{\text{Optim.}}$	0.813	0.713	0.709	0.637	0.483	0.477	0.701	0.631	0.549	0.572	0.696	0.701	0.773	0.782	0.838
$\text{Bias}_{\Phi_{dp}\text{ low}}$	0.819	-1.116	-1.634	-2.054	-1.027	-2.560	-10.83	-5.628	NA	-0.625	2.000	-2.001	-1.659	-0.091	1.147
$\alpha_{C,\Phi_{dp}\text{ high}}$	0.064	0.070	0.068	0.070	0.049	0.026	-0.220	-0.049	NA	0.045	0.038	0.050	0.056	0.068	0.086

Parameter	**B31**	**B32**	**B33**	**B34**	**B35**	**B36**	**B37**	**B38**	**B39**	**B40**	**B41**	**B42**	**B43**	**B44**	**B45**
Valid Points	17515	16219	7417	2219	1496	96	0	0	0	0	0	0	0	21	155
$\alpha_{\text{C,Optimized}}$	0.072	0.064	0.124	0.067	0.012	-0.033	NA	NA	NA	NA	NA	NA	NA	-0.575	0.320
$\text{StDev}_{\text{Uncor.}}$	6.410	5.466	6.043	4.905	4.630	1.901	NA	NA	NA	NA	NA	NA	NA	4.274	4.700
$\text{StDev}_{\text{Corr.}}$	4.727	4.941	4.745	4.712	4.740	2.587	NA	NA	NA	NA	NA	NA	NA	4.621	4.620
$\text{StDev}_{\text{Optim.}}$	4.340	4.686	4.687	4.644	4.628	1.846	NA	NA	NA	NA	NA	NA	NA	3.180	4.546
$\text{Bias}_{\text{Corr.}}$	2.097	-0.802	-1.201	0.245	-1.086	1.728	NA	NA	NA	NA	NA	NA	NA	5.247	3.269
$\text{Bias}_{\text{Optim.}}$	0.542	-1.019	-1.213	-0.355	-3.326	-3.112	NA	NA	NA	NA	NA	NA	NA	-9.269	7.333
$\text{Corr}_{\text{Uncor.}}$	0.472	0.751	0.834	0.776	0.370	0.904	NA	NA	NA	NA	NA	NA	NA	0.283	0.841
$\text{Corr}_{\text{Corr.}}$	0.815	0.878	0.924	0.811	0.342	0.819	NA	NA	NA	NA	NA	NA	NA	0.259	0.836
$\text{Corr}_{\text{Optim.}}$	0.788	0.868	0.908	0.809	0.354	0.854	NA	NA	NA	NA	NA	NA	NA	0.265	0.838
$\text{Bias}_{\Phi_{dp}\text{ low}}$	1.170	0.334	0.836	0.844	-1.129	-2.291	NA	NA	NA	-6.694	-3.668	-2.604	2.195	-1.117	0.396
$\alpha_{C,\Phi_{dp}\text{ high}}$	0.076	0.070	0.125	0.078	0.076	-0.014	NA	NA	NA	NA	NA	NA	NA	-0.279	-0.008

Parameter	**B46**	**B47**	**B48**	**B49**	**B50**	**B51**	**B52**	**B53**	**B54**	**B55**	**B56**	**B57**	**B58**
Valid Points	5102	27129	57553	59802	29001	18759	22682	5394	1303	517	110	0	0
$\alpha_{\text{C,Optimized}}$	0.073	0.059	0.025	0.034	0.066	0.065	0.038	0.028	0.031	0.100	0.143	NA	NA
$\text{StDev}_{\text{Uncor.}}$	6.088	5.688	4.672	5.120	4.564	4.476	4.169	4.014	4.600	4.469	3.496	NA	NA
$\text{StDev}_{\text{Corr.}}$	6.072	5.681	4.710	5.138	4.536	4.377	4.240	4.147	4.661	4.430	3.402	NA	NA
$\text{StDev}_{\text{Optim.}}$	6.069	5.675	4.667	5.113	4.527	4.337	4.128	3.991	4.584	4.430	3.393	NA	NA
$\text{Bias}_{\text{Corr.}}$	1.089	0.751	0.323	0.615	1.624	-2.045	-2.530	-1.781	0.575	0.371	0.788	NA	NA
$\text{Bias}_{\text{Optim.}}$	0.456	-0.204	-1.502	-0.982	0.905	-0.976	-0.047	-0.039	-0.908	0.373	1.897	NA	NA
$\text{Corr}_{\text{Uncor.}}$	0.758	0.743	0.747	0.721	0.746	0.734	0.698	0.750	0.789	0.404	0.057	NA	NA
$\text{Corr}_{\text{Corr.}}$	0.760	0.752	0.756	0.729	0.768	0.741	0.724	0.779	0.787	0.348	-0.008	NA	NA
$\text{Corr}_{\text{Optim.}}$	0.760	0.750	0.727	0.762	0.745	0.722	0.777	0.791	0.364	0.012	0.012	NA	NA
$\text{Bias}_{\Phi_{dp}\text{ low}}$	-0.304	NA	NA	NA	0.299	0.672	0.104	0.716	1.453	0.410	-2.656	NA	NA
$\alpha_{C,\Phi_{dp}\text{ high}}$	0.032	NA	NA	NA	0.051	0.026	0.034	0.005	0.103	0.107	-0.014	NA	NA

Table B.3: Statistical metrics for the 30 minutes aggregation on 28 August 2025 for the Bric della Croce and Settepani radars. The table is split into four sections for better readability.

Bibliography

[1] V Chandrasekar, R M Beauchamp, and R Bechini. *Introduction to Dual Polarization Weather Radar: Fundamentals, Applications, and Networks*. Cambridge: Cambridge University Press, 2023, pp. 1–11 (cit. on pp. 1–4, 6, 10–12, 15, 17, 21, 22, 25–27, 31, 32, 36–38, 40).

[2] Frédéric Fabry. *Radar Meteorology: Principles and Practice*. Cambridge University Press, 2015 (cit. on pp. 9, 11–18, 23, 24, 28, 47).

[3] Roberto Cremonini and Renzo Bechini. "Heavy Rainfall Monitoring by Polarimetric C-Band Weather Radars". In: *Water* 2.4 (2010), pp. 838–848. ISSN: 2073-4441. DOI: 10.3390/w2040838. URL: https://www.mdpi.com/2073-4441/2/4/838 (cit. on pp. 34, 93).

[4] R. Bechini, L. Baldini, and V. Chandrasekar. "Polarimetric Radar Observations in the Ice Region of Precipitating Clouds at C-Band and X-Band Radar Frequencies". In: *Journal of Applied Meteorology and Climatology* 52.5 (2013), pp. 1147–1169. DOI: 10.1175/JAMC-D-12-055.1. URL: https://journals.ametsoc.org/view/journals/apme/52/5/jamc-d-12-055.1.xml (cit. on p. 34).

[5] M. Vaccarono, R. Bechini, C. V. Chandrasekar, R. Cremonini, and C. Cassardo. "An integrated approach to monitoring the calibration stability of operational dual-polarization radars". In: *Atmospheric Measurement Techniques* 9.11 (2016), pp. 5367–5383. DOI: 10.5194/amt-9-5367-2016. URL: https://amt.copernicus.org/articles/9/5367/2016/ (cit. on pp. 34, 35, 41, 42).

[6] E. Adirosi et al. "Database of the Italian disdrometer network". In: *Earth System Science Data* 15.6 (2023), pp. 2417–2429. DOI: 10.5194/essd-15-

2417-2023. URL: https://essd.copernicus.org/articles/15/2417/2023/ (cit. on p. 105).

[7] Alexander Ryzhkov, Pengfei Zhang, Petar Bukovčić, Jian Zhang, and Stephen Cocks. "Polarimetric Radar Quantitative Precipitation Estimation". In: *Remote Sensing* 14.7 (2022). ISSN: 2072-4292. DOI: 10.3390/rs14071695. URL: https://www.mdpi.com/2072-4292/14/7/1695 (cit. on p. 105).

[8] Yanting Wang and V. Chandrasekar. "Algorithm for Estimation of the Specific Differential Phase". In: *Journal of Atmospheric and Oceanic Technology* 26.12 (2009), pp. 2565–2578. DOI: 10.1175/2009JTECHA1358.1. URL: https://journals.ametsoc.org/view/journals/atot/26/12/2009jtecha1358_1.xml (cit. on pp. 107, 108).

Dedications

I would like to express my sincere gratitude to my supervisor, Prof. Battaglia, for inspiring me and providing invaluable guidance throughout this work.
I am also deeply thankful to my co-supervisors, Dr. Renzo Bechini and Dr. Valentina Campana, for their mentorship and encouragement during my time at Arpa.
Finally, I am grateful to my parents and friends for their unwavering support and constant presence, both in completing this thesis and throughout my academic journey.